Nina Kristine Reitan

Methods for studying critical barriers to the delivery of nanomedicine

The potential of fluorescence correlation spectroscopy, confocal microscopy and MRI

Thesis for the degree of Philosophiae Doctor

Trondheim, June 2009

Norwegian University of Science and Technology
Faculty of Natural Sciences and Technology
Department of Physics

NTNU
Norwegian University of
Science and Technology

NTNU
Norwegian University of Science and Technology

Thesis for the degree of Philosophiae Doctor

Faculty of Natural Sciences and Technology
Department of Physics

ISBN 978-82-471-1620-3 (printed ver.)
ISBN 978-82-471-1621-0 (electronic ver.)
ISSN 1503-8181

Doctoral theses at NTNU, 2009:118

Printed by NTNU-trykk

Acknowledgements

The work presented in this thesis has been carried out at the Department of Physics, Norwegian University of Science and Technology (NTNU) during the period 2004 – 2009 in collaboration with the Department of Biotechnology and the Department of Circulation and Medical Imaging, NTNU. Financial support was provided by the Department of Physics, NTNU, and the Norwegian Cancer Society.

The diversity of techniques applied has made the work both interesting and challenging, and many people deserve to be mentioned for their various contributions.

First of all I would like to express my gratitude to my supervisor, Professor Catharina de Lange Davies. Your competence and unique enthusiasm in the field of drug delivery have deeply inspired me during these years. You have been supportive and always available to provide guidance when needed, and I thank you for never giving me the opportunity to give up, even in my most frustrated moments.

I would also like to thank co-authors for their contributions, co-supervisor Professor Tore Lindmo for advice and constructive feedback, Research Scientist Sabina P. Strand for collaboration and discussions on the field of gene delivery, the people at the MR Center for practical help with experiments and analysis, and Edrun A. Schnell and Astrid Bjørkøy for technical assistance. Thanks to Kristin Grendstad Sæterbø for invaluable effort in the lab, and for her good spirits and great way with animals.

Thanks to my colleagues for sharing your scientific expertise over a cup of coffee and for initiating social activities outside the office. It has been a pleasure to work with you.

I am also deeply grateful to family and dear friends, to those who passed away and those who patiently stood by me throughout these years, even when my work intruded on my social life. A special thanks to my beloved daughter for just being wonderful and for reminding me of the most important things in life. This one's for you, Maja!

Abbreviations

A/P	amino/phosphate
AFM	atomic force microscope
CLSM	confocal laser scanning microscopy
CMV	cytomegalovirus
DCE-MRI	dynamic contrast enhanced magnetic resonance imaging
DLS	dynamic light scattering
DNA	deoxyribonucleic acid
DP	degree of polymerization
ECM	extracellular matrix
FCCS	fluorescence cross-correlation spectroscopy
FCS	fluorescence correlation spectroscopy
FITC	fluorescein isothiocyanate
FOV	field of view
FRAP	fluorescence recovery after photobleaching
Gd	gadolinium
GFP	green fluorescent protein
HEK293	human embryonic kidney 293 cells
HPLC	high-performance liquid chromatography
IFP	interstitial fluid pressure
IgG	immunoglobulin G
LCO	linear (unsubstituted) chitosan oligomer
Luc	luciferase
MRI	magnetic resonance imaging
MVP	microvascular pressure
OHS	osteohuman sarcoma
Polyplex	polyelectrolyte complex (polyanion-polycation)
POM	poloxy methylen
RLU	relative luciferase units
ROI	region of interest
SB-TCO	self-branched trisaccharide substituted chitosan oligomer
SNR	signal-to-noise ratio
TCO	trisaccharide substituted chitosan oligomer
TMR	tetramethylrhodamine

List of papers

The present work is based on the following original reports, which will be referred to in the text by their roman numerals:

I **Reitan N K**, Juthajan A, Lindmo T, Davies C de L. *Macromolecular diffusion in the extracellular matrix measured by fluorescence correlation spectroscopy*. Journal of Biomedical Optics 13(5), 054040, 2008.

II **Reitan N K**, Maurstad G. Davies C de L, Strand S P. *Characterizing DNA condensation by structurally different chitosans of variable gene transfer efficacy*. Biomacromolecules, April 9, 2009.

III Strand S P, Lelu S, **Reitan N K**, Artursson P, Davies C de L, Vårum K M. *Structure-function relationship in chitosan-mediated gene delivery: controlling polyplex disassembly through chitosan design.* Manuscript in preparation.

IV **Reitan N K**, Thuen M, Goa P E, Davies C de L. *Characterization of tumor microvascular structure and permeability: comparison between MRI and intravital confocal imaging*. Manuscript in preparation.

Contributions to the papers

The work on which this thesis is based is presented in papers and have involved collaboration with others. My contributions to the papers are as follows:

I Manuscript, experimental work (sample preparations and a major part of the FCS measurements), and data analysis.

II Manuscript, experimental work (sample preparations, DLS, FCS, FCCS, AFM), and data analysis. Parts of the AFM and DLS analysis were performed by Dr. Gjertrud Maurstad. Fluorescently labeled chitosans were provided by Dr. Sabina P. Strand.

III Involved in planning and performing CLSM and FCS experiments.

IV Manuscript, involved in design of the MRI-compatible dorsal window chamber, designing the experimental setup, preparing animals for experiments (implantation of the dorsal window chambers was not performed by me), performing CLSM and MRI, and data analysis. Dr. Marte Thuen assisted in optimizing the DCE-MRI protocols and a Matlab script written by Dr. Pål Erik Goa was used for analysis of the DCE-MRI data.

Contents

1 Introduction

1.1 Nanomedicine in drug delivery

A challenge in conventional therapy is the non-selective delivery of toxic agents to both normal and diseased tissue. Sophisticated drug delivery aims to develop selective and specific delivery of therapeutic and diagnostic agents in order to minimize systemic side-effects. To achieve this goal, knowledge and experience from nanotechnology, advanced polymer chemistry, and optical engineering are being brought together.

The term nanomedicine has been given a variety of definitions.[1-3] Here, we define nanomedicine as nanoscale or nanostructured materials in medicine that by their structure have unique medical effects.[2] Nanomedicine differ from small-molecule drugs and includes macromolecular therapeutic agents, such as monoclonal antibodies, liposomes, polymers, and dendrimers. Nanomedicine may have inherent diagnostic properties themselves, or they may protect, induce target-specificity or -selectivity, or overcome drug solubility issues by serving as vehicles for therapeutic and diagnostic agents.[3]

In this work we focus on drug delivery after intravenous administration. For successful drug delivery, the therapeutic agents must be transported across the vascular wall and through the extracellular matrix (ECM) toward the target cells. If the target is the cell nucleus, the therapeutic agents must further penetrate the cell membrane and travel through the intracellular environment to the nucleus. Each of these steps constitutes a barrier to drug delivery. In cancer therapy, macromolecular therapeutic agents are of great interest due to their selectivity or specificity for tumor tissue after injection. However, only a minor fraction of the injected macromolecules has been shown to accumulate in tumor tissue, and the distribution is heterogeneous.[4-6] The biodistribution of the therapeutic agents is determined by the microvascular network, perfusion, permeability across the blood vessel wall, and diffusion through the extracellular matrix to the target cells. It is therefore important to develop suitable methods for characterizing transport in the vascular, interstitial, and cellular compartments.

1.2 Tumor characteristics

Because of inadequate blood perfusion, tumors are characterized by a range of structural and functional abnormalities which form barriers to the delivery of nanomedicine[7,8] The vascular architecture is tortuous, irregular, and highly heterogeneous (Fig. 1).[7,9] The endothelial lining of the tumor vessel wall is incomplete or missing, which results in leaky tumor vessels. Due to the chaotic, permeable vascular network combined with a high microvascular pressure (MVP), the interstitial fluid pressure (IFP) in tumors is elevated. This diminishes the pressure gradient and thereby the fluid flow from the vessels to the interstitium.[5,10-12] The absence of an anatomically well-defined functioning lymphatic network is also characteristic of tumors. Excess fluid which is not reabsorbed into the microvascular network may thus ooze out of the tumor periphery and be collected by the lymphatic vessels of the surrounding normal tissue, thereby aiding the metastatic process.[13]

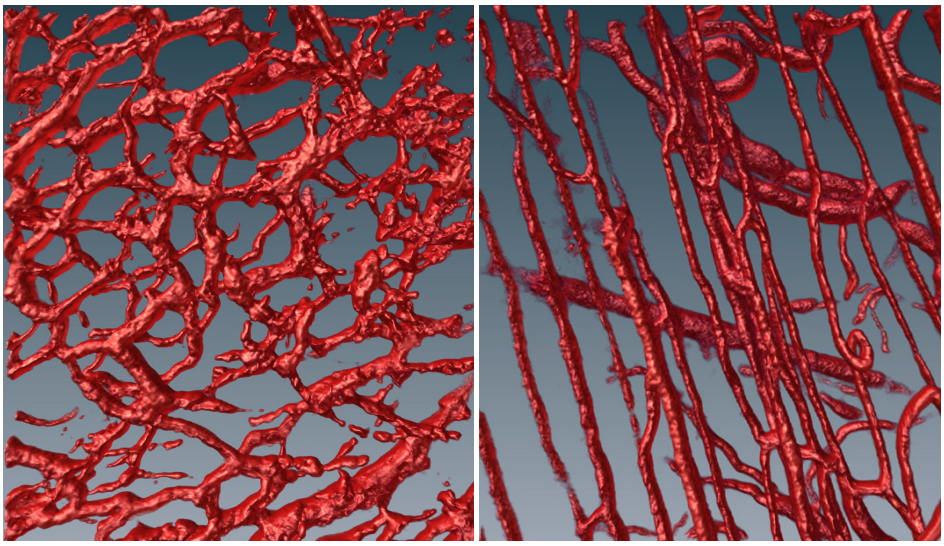

Figure 1. 3D reconstruction of blood vessels in mice showing the abnormal architecture of the tumor microenvironment characterized by tortuous vasculature (left) compared to the well-organized parallel blood vessels in normal tissue (right).

The enhanced vascular permeability is of great interest in cancer-selective therapy because the leaky capillaries favor the transport of therapeutic agents across the blood vessel wall.[14] It is mainly macromolecules that are able to utilize this hyperpermeability and discriminate between normal and tumor vessels, and not low molecular weight compounds like most conventional anticancer agents. Macromolecules also show slower clearance from tumors and inflammatory tissue compared to low molecular weight substances, which are not retained but diffuse back into the circulating blood, and they have a longer plasma half-time which enhances the therapy efficacy.[15-17] The vascular permeability is shown to be dependent on the molecular weight and charge of the tracer,[18,19] as well as the tumor type.[20-22]

Angiogenesis is essential for formation of new blood vessels and is an important step in tumor growth. The number of branching points is an estimate of the number of neo-formed vessels. This parameter, called the fork density, has previously been shown to correlate with angiogenetic activity.[23] Early quantitative studies showed that the vascular volume predicted growth rate and stage of tumors, and slightly higher vascular density has been reported in tumors compared to normal tissue.[24-27] However, both vascular volume and density are dependent on tumor type.[28,29] Fractal analysis describes non-Euclidean structural properties like self-similarity and tortuousity.[30,31] The fractal dimension of the microvasculature may be used to distinguish between the architecture of tumor and normal tissue, and may predict necrosis, survival, and tumor grade.[32,33]

The interstitium, defined as the extracellular space exclusive of the vascular space, consists of a collagen and elastic fiber network embedded in a hydrophilic gel of glycosaminoglycans and proteoglycans. The interstitium of tumors has several abnormal characteristics. The large interstitial space and low concentrations of polysaccharides may facilitate transport of therapeutic agents.[13,29] On the other hand, the high IFP in the inner parts of tumors induces an outward pressure gradient that obstructs the penetration of therapeutic agents.[9]

1.3 Molecular transport mechanisms in tissue

Tissue can be divided into the vascular, interstitial, and cellular subcompartments. Transport of molecules in and between these compartments depends on the microenvironment as well as molecular parameters, like size, charge, and structure of the drug and its carrier. Because of the high IFP in tumors, transvascular and interstitial transport is largely dependent on diffusion.

1.3.1 Diffusion and convection

The thermal fluctuations of a particle suspended in a fluid cause it to constantly collide with surrounding particles. This random movement induces a net transport of the particles from an area of high concentration to an area of lower concentration. The one-dimensional diffusion flux J_D is proportional to the concentration gradient $\partial C / \partial x$, as described by Fick's law

$$J_D = -D\left(\frac{\partial C}{\partial x}\right) \tag{1}$$

where D is the macroscopic diffusion coefficient, C the particle concentration, and x the position coordinate.

Fick's law leads to the diffusion equation, whose solution describes the mean square displacement of a freely diffusing particle by

$$\left\langle x^2(t)\right\rangle = 6Dt \tag{2}$$

The mean square displacement is thus proportional to the square root of the elapsed time t and the diffusion coefficient. Diffusion is a slow process for large particles, and the diffusion coefficient is related to the hydrodynamic radius R of the diffusing particle by the Stokes-Einstein relation

$$D = \frac{k_B T}{6\pi\eta R} \tag{3}$$

where k_B is the Boltzmann constant, T is the temperature and η is the viscosity of the solvent.

In complex media, the mean square displacement is expected to obey a power law

$$\left\langle x^2(t)\right\rangle = 6\Gamma t^{\alpha} \tag{4}$$

where Γ is a constant independent of time. If the exponent $\alpha \neq 1$ the diffusion is anomalous, and anomalous subdiffusion is given by $\alpha < 1$. For anomalous diffusion the diffusion coefficient depends on the timescale, or equivalently the length scale, of the measurement and can be written as[34]

$$D(t) = \Gamma t^{\alpha-1} \tag{5}$$

Convection is fluid flow from areas of high pressure to areas of low pressure. The convective flux can be described by[35]

$$J_C = Cv \tag{6}$$

where v is the velocity of the dissolved particles and the solvent.

1.3.2 Transvascular transport

The transport of a solute across the vessel wall and into the interstitium occurs by diffusion and convection. The total transvascular flow of solute J_T can be described by the Staverman-Kedem-Katchalsky equation

$$J_T = PA\left(c_v - c_i\right) + J_F\left(1-\sigma_F\right)\frac{c_v - c_i}{ln\left(c_v / c\right)} \tag{7}$$

where P is the diffusive permeability, A the surface area of the vessel, c_v and c_i the plasma and interstitial concentrations of the solute, respectively, J_F the net fluid flow across the vessel wall, and $\left(1-\sigma_F\right)$ the coupling between fluid and solute transport.[14]

According to Starling's hypothesis, net fluid flow across a vessel wall is given by

$$J_F = L_P A\left[\left(MVP - IFP\right) - \sigma\left(\pi_v - \pi_i\right)\right] \tag{8}$$

where J_F is the volume flow of fluid across the vessel wall, L_P the hydraulic conductivity of the vessel, MVP and IFP the vascular and interstitial fluid pressures, σ the osmotic reflection coefficient, and π_v and π_i the colloid-osmotic pressures in plasma and interstitial fluid.[36] Due to the elevated IFP in tumors, J_F is extremely low and the diffusive term of Eq. (7) is the dominating.

1.3.3 Interstitial transport

The transport of molecules in the interstitium is also governed by diffusion and convection. One-dimensional interstitial transport J_I can be described as the sum of a diffusive and a convective term as

$$J_I = -D\frac{\partial C}{\partial x} - CR_F K\frac{\partial p}{\partial x} \tag{9}$$

where the diffusive term is identical to Eq. 1 and the convective term is described by the retardation factor R_F, the tissue hydraulic conductivity K for convective flow of solvent through the medium, and the pressure gradient $\partial p / \partial x$.[13]

1.3.4 Intracellular transport and gene delivery

The intracellular pathway for nanomedicine constitutes a complex journey. The therapeutic agents must be transported through the cell membrane by endocytosis and survive in the hostile intracellular environment as they travel to the cell nucleus. In the field of gene delivery, research aims to develop gene vectors that facilitate transport and protect the DNA from degradation. Out of non-viral gene delivery vectors, cationic polymers are one of the major types. Because of their permanent cationic charge, polycations spontaneously self-assembly with the negatively charged DNA and form compacted DNA-polycation complexes (polyplexes). The complexation reduces the extensive size of the DNA molecule and masks its negative charges, and thus aids the transport through the cell membrane and protects the DNA against nuclease degradation.[37,38] The condensation behavior depends on the length of the DNA, the structure of the polycation, and the mixing ratio.[39,40]

Polyplexes are internalized by endocytosis and delivered to endosomes and subsequently to lysosomes. Further delivery of DNA to the nucleus requires escape of the polyplex from endosomes or lysosomes, DNA/polymer dissociation, cytoplasmic DNA diffusion, and nuclear uptake.[41-45] Polymer-based gene transfer requires a balance between sufficient DNA protection and intracellular DNA release, which reflects the degree of interaction between the polycation and the DNA.[46-48] Inside the nucleus the exogenous genes are transcribed. A schematic drawing of the gene delivery pathway of polyplexes is shown in Fig. 2.

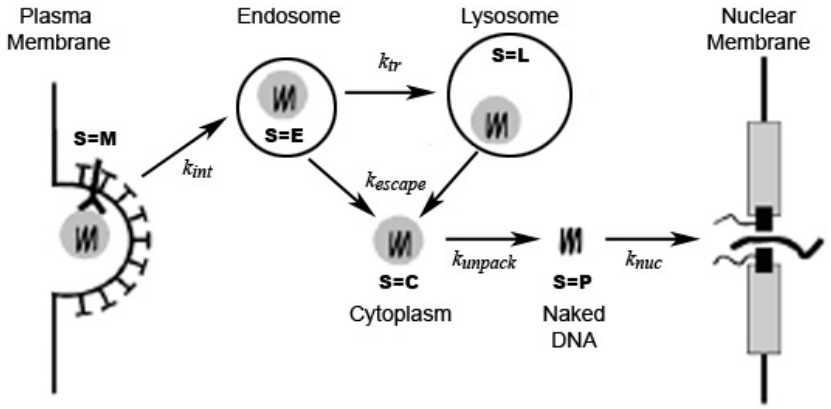

Figure 2. After binding to the cell membrane, the intracellular pathway of a polyplex can be represented by five distinct biophysical states (S): bound to cell membrane (S=M), inside endosomes (S=E), inside lysosomes (S=L), in the cytoplasm (S=C), and unpacked plasmids (S=P). The figure is from Dinh *et al.* [41]

1.4 Experimental methods

This section presents the various techniques applied in the present work. Fluorescence correlation spectroscopy (FCS) was used in three out of four papers, and is therefore more thoroughly described.

1.4.1 Confocal laser scanning microscopy and fluorescence correlation spectroscopy

Confocal laser scanning microscopy (CLSM) and fluorescence correlation spectroscopy (FCS) were performed on an LSM510/Confocor2 (Carl Zeiss Jena GmbH, Germany). The combination of the LSM510 microscope with Confocor2 allows performing FCS at well defined spots which are predefined in CLSM images. CLSM was used for imaging of xenografts growing in dorsal window chambers in mice (Paper IV) and for imaging spheroids (Paper I) and cells (Paper III) before FCS measurements. FCS was used for measuring diffusion and interactions of macromolecules in solution (Paper I and II) as well as extra- (Paper I), and intracellularly (Paper III). Fluorescence cross-correlation spectroscopy (FCCS) was applied to identify bound DNA-chitosan complexes (Paper II).

CLSM is a high-resolution technique and allows 3D reconstruction of thick specimens by optical sectioning. A beam of laser light is directed toward the specimen by a beam splitter and focused onto a small point at the focal plane of the specimen. A computer controlled scanning mirror scans the beam across the specimen in the x-y-direction. Out-of-focus fluorescence emission is blocked from reaching the photomultiplier by placing a pinhole aperture in the conjugate focal plane to the specimen.

In FCS mode the scanning mirror is not in use and the measurement is performed at a single point with a volume defined by the confocal optics (<1 fl). Due to the small detection volume, it is possible to detect even single molecules. FCS was first introduced by Madge, Elson and Webb in 1972.[49] These early measurements suffered from poor signal-to-noise ratios, mainly because of low detection efficiency, large concentrations, and insufficient background suppression. A major improvement was made by Rigler and coworkers by combining the FCS technique with confocal detection.[50] To date, most FCS measurements are performed on fluorescently labeled biomolecules diffusing in aqueous buffer solution, but the technique is increasingly used in tissue and intracellular studies.[51-56] In FCS the parameter of interest is not the emission intensity itself, but spontaneous intensity fluctuations caused by minute deviations from thermal equilibrium. A variety of physical parameters that give rise to fluctuations in the fluorescence signal are accessible by FCS, and the method can be used to determine concentrations, mobility, and characteristic rate constants of molecular reactions. The requirements imposed on a fluorophore in FCS are high photostability, high quantum efficiency, and a large absorption cross section.

Analysis in FCS consists of three basic steps. First, the intensity fluctuations from fluorescent particles diffusing through the detection volume are recorded. Subsequently, the intensity fluctuations are correlated over time, and the third step is to apply a mathematical fitting model that provides access to the desired parameters describing the system. Autocorrelation analysis is sufficient for studying mobility, as well as interactions if the binding parameters can be linked to a measurable change in mobility. Otherwise fluorescent dual-labeling and FCCS are required. In intracellular studies the measured molecular mobility will depend on the environment. FCCS may then be a valuable tool to verify that slow diffusion stems from dual-labeled complexes and not background fluorescence or molecular binding to cellular components. The basic principles of fluorescence auto- and cross-correlation spectroscopy are shown in Fig. 3.

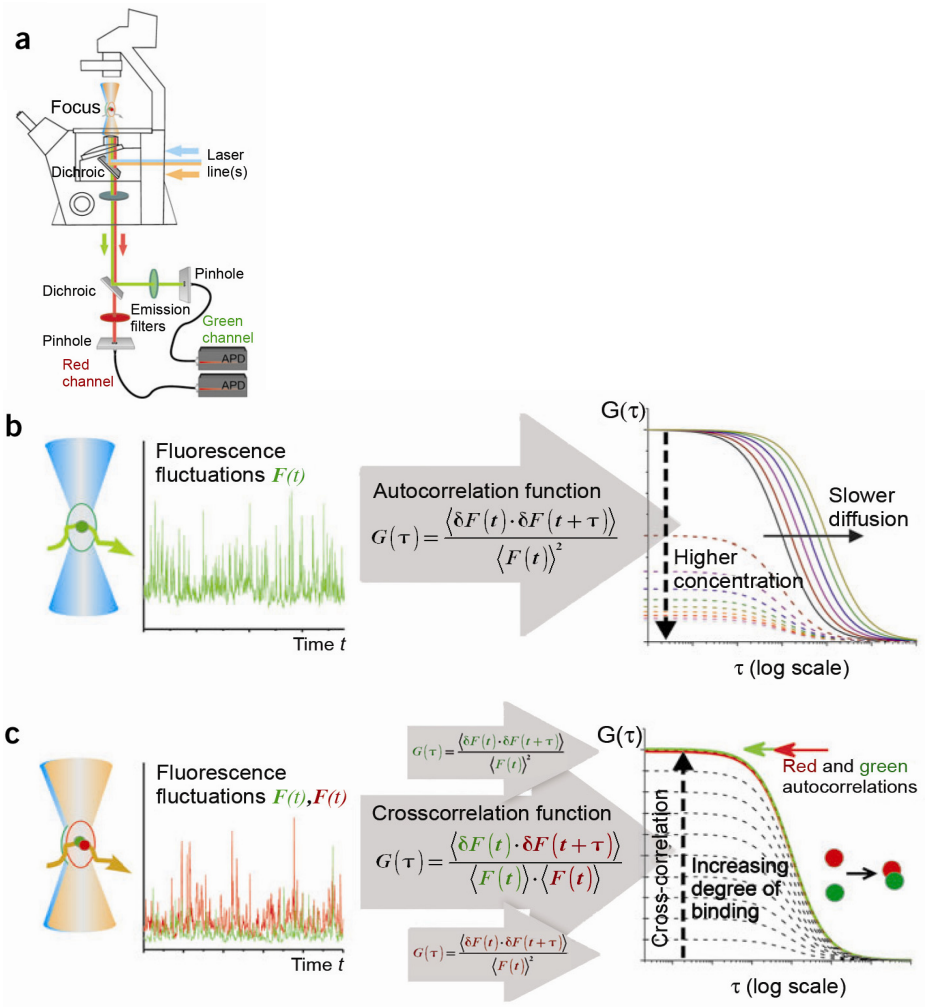

Figure 3. The basic principles of FCS and FCCS. a) Schematic drawing of the confocal instrumental setup. One laser line is used for exciting single-labeled fluorophores. Two laser lines are used for dual-color FCCS, for which red- and green-shifted fluorescence light are separated by a second dichroic mirror and directed through pinholes to their respective detectors. b) Single-color FCS. Fluorescent molecules are excited by a laser beam and fluoresce as they travel through the confocal volume. The fluctuations in the fluorescence intensity are recorded and an autocorrelation algorithm is applied to the time trace. The resulting autocorrelation curve contains information about the concentration of particles in the detection volume (dashed line), the characteristic diffusion time (solid line), and other dynamic processes. c) Dual-color FCCS. Two molecules are fluorescently labeled, and emission from both fluorophores is recorded in separate channels (red and green). When the two molecules are bound, they simultaneously fluoresce as they diffuse through the detection volume, and colocalized intensity peaks can be observed in the time traces for the red and the green channel. The signal in each channel is autocorrelated (solid red and green), and the cross-correlation is computed (dashed black). The relative amplitude of the cross-correlation curve contains information about the degree of binding. The figure is from Schwille *et al.*[52]

A multi-component free diffusion model including triplet decay may be described by

$$G(\tau) = 1 + \frac{1}{\langle N \rangle} \cdot \frac{1 - T + Te^{-\frac{\tau}{\tau_T}}}{1 - T} \cdot \left[\sum_{i=1}^{m} \frac{\Phi_i}{\left(1 + \frac{\tau}{\tau_{D_i}}\right)\sqrt{1 + \left(\frac{\omega_{xy}}{\omega_z}\right)^2 \cdot \frac{\tau}{\tau_{D_i}}}} \right] \tag{10}$$

where $\langle N \rangle$ is the mean number of particles in the detection volume, T and τ_T are the triplet fraction and triplet lifetime, respectively, assumed equal for all components, Φ_i is the fractional intensity of the *i*th species, m the total number of species in the sample, and τ_{D_i} the characteristic translational diffusion time of the *i*th species through the detection volume. ω_{xy} and ω_z are the axial and the radial waists of the Gaussian detection volume, respectively, defined as the distances at which the intensity drops to $1/e^2$ of the maximum intensity.[57] For $m = 1$ and $m = 2$, Eq. (10) is reduced to the one- and two-component diffusion model used in the present work.

The diffusion coefficient D is related to the characteristic diffusion time and the radial waist by

$$D = \frac{{\omega_{xy}}^2}{4\tau_D} \tag{11}$$

For FCS measurements in aqueous solution the free diffusion model is generally adequate. In more complex model systems, however, diffusion may be retarded or facilitated by flow, and the free diffusion model will fail to describe the system. In such cases, an anomalous diffusion model may be more sufficient

$$G(\tau) = 1 + \frac{1}{\langle N \rangle} \cdot \frac{1 - T + Te^{-\frac{\tau}{\tau_T}}}{1 - T} \cdot \frac{1}{\left(1 + \frac{\tau}{\tau_{D_i}}\right)^{\alpha} \sqrt{1 + \left(\frac{\omega_{xy}}{\omega_z}\right)^2 \cdot \left(\frac{\tau}{\tau_{D_i}}\right)^{\alpha}}} \tag{12}$$

where α is the anomaly coefficient.[57] The value of α indicates the degree of anomaly, and equals 1 for free, Brownian diffusion. Obstructed diffusion (anomalous subdiffusion) is indicated by $\alpha < 1$, and $\alpha > 1$ represents facilitated diffusion (anomalous superdiffusion).

When labeling two species (here denoted “red” and “blue”) and studying interactions by FCCS, the mobility and concentration of each of the species can still be analyzed by its respective autocorrelation function. The cross-correlation amplitude, however, gives information about the number of dual-labeled species, i.e. the bound molecules, and can be described as

$$G(0) = 1 + \frac{1}{N_{cc}} = 1 + \frac{N_{br}}{N_{acr} N_{acb}} = 1 + \frac{N_{br}}{(N_r + N_{br})(N_b + N_{br})} \tag{13}$$

where N_r, N_b, N_{acr}, N_{acb}, and N_{br} is the number of free red, free blue, total red, total blue, and bound red-blue species, respectively.[57]

1.4.2 Dynamic contrast enhanced MRI

After imaging by CLSM, dynamic contrast enhanced magnetic resonance imaging (DCE-MRI) was performed and permeability was estimated in xenografts growing in dorsal window chambers (Paper IV). Gadomer was used as a contrast agent.

DCE-MRI was performed at 7.05 T using a Bruker Biospec Avance 70/20 (Bruker Biospin, Ettlingen, Germany). DCE-MRI is a non-invasive technique widely used both in the clinic and in research. It has frequently been applied to quantify tumor microvascular characteristics like angiogenesis, perfusion, and permeability,[20,58-60] and a variety of contrast agents are available.[61-63] The insufficiency of traditional small molecular contrast agents to utilize the hyperpermeability of tumor vasculature has encouraged the development of macromolecular contrast agents.[63] The spatial resolution in DCE-MRI is lower than in CLSM.

1.4.3 Atomic force microscopy

The morphology of DNA-chitosan polyplexes (Paper II) was analysed by applying tapping mode atomic force microscopy (AFM) on a NanoScope IIIa (Digital Instruments, CA) equipped with an E-scanner. In tapping mode AFM a cantilever is driven to oscillate near its resonance frequency by a piezoelectric element. Deflections of the cantilever caused by interactions with the sample surface are detected as the cantilever scans over the dried sample, and a topographic image of the sample is produced.[64,65] AFM can detect heights of structures with sub-nanometer resolution. The

technique has frequently been used for analyzing polyplexes and has demonstrated that condensation of DNA with chitosan forms polyplexes with various shapes, such as rods, toroids and globules. [66-68]

1.4.4 Other applied techniques

Dynamic light scattering (DLS) was used to measure the hydrodynamic diameter of DNA-chitosan polyplexes (Paper II and III) by using the Zetasizer Nano Zs (Malvern Instruments, UK) with a 633 nm laser. DLS is typically used to measure the size of particles dissolved in a liquid by illuminating the solution with the laser and detecting scattered light at a given scattering angle. The intensity of the fluctuations is dependent on the size of the particles and the hydrodynamic diameter of the particles is calculated by the Stokes-Einstein relation (Eq. 3). DLS has frequently been used to measure the size of polyplexes.[40,69]

Gel electrophoresis was performed to analyze the stability of DNA-chitosan polyplexes (Paper II and III). In gel electrophoresis an electric field forces the polyplex fragments to migrate through a gel. DNA molecules normally migrate from negative to positive potential due to the net negative charge of the phosphate backbone of the DNA chain, and longer molecules migrate more slowly through the gel. Upon condensation by polycations, the negative charge is masked. By applying chitosans of various properties, the condensation ability of the respective chitosan and stability of the polyplexes are analyzed.[40,69]

Reporter plasmids (gWiz^{TM}Luc and gWiz^{TM}GFP) containing a cytomegalovirus promoter (CMV) and firefly luciferase (Luc) or green fluorescent protein (GFP) was complexed with chitosan and introduced into human embryonic kidney (HEK) 293 cells by *in vitro transfection* (see Paper III for details). In vitro investigation of transfection efficacy in cell culture is a valuable tool for investigating various promising materials for transfection,[37] and provides an opportunity to study the transgene expression dependence on the chitosan structure on a single cell level.[40]

Flow cytometry analysis of GFP-expressing cells or polyplex uptake with YOYO-1 labeled DNA was performed using a BD LSR1 (Becton Dickinson, San Jose, CA) (Paper III). In flow cytometry, laser light of different wavelengths are being directed to a stream of fluids where single cells flow through. When cells pass the light beams, fluorescence and light scattering are detected and physical and chemical features of the

cells are being analyzed. Flow cytometry of GFP-expressing genes has previously shown that chitosan structure affects gene transfer efficacy.[40]

1.4.5 Data analysis

A wide range of tools for image analysis and quantitation have been applied and are described in the respective papers.

1.5 Molecular tracers

1.5.1 Dextrans

Fluorescently labeled dextrans of various molecular weights were used to measure interstitial diffusion (Paper I) and vascular permeability (Paper IV), and as an intravascular agent to image blood vessels (Paper IV). Dextrans are neutrally charged, complex, branched glucans of various lengths, and are commercially available in a wide range of molecular weights, also with fluorescent probes attached. They are frequently used both as tracers and drug carriers, have no affinity for cells, and are ideal for diffusion measurements.[70-72]

1.5.2 IgG

Extracellular diffusion of antibody immunoglobulin IgG was compared to that of dextrans (Paper I). IgG is a monomeric immunoglobulin, has a globular structure, and a molecular weight of 150 kDa. It is the most abundant immunoglobulin and is approximately equally distributed in blood and in tissue liquids. IgG is also non-specific and suited for diffusion measurements.[73]

1.5.3 DNA-chitosan polyplexes

Complexation, kinetics, and morphology of fluorescently labeled DNA-chitosan polyplexes were studied (Paper II and III). Chitosan, a biopolymer derived from chitin, has been shown to efficiently compact DNA and protect it from degradation by nucleases,[74] and the interest in chitosan as a non-viral vector in gene delivery is

increasing.[75,76] Although not as efficient as its viral counterparts, chitosan is biocompatible, exhibit low immunogenicity and less cytotoxicity than viral vectors.[40,77] Chitosan is a linear polysaccharide composed of $(1\rightarrow 4)$-β-linked N-acetyl-D-glucosamine (acetylated units) and D-glucosamine (de-N-acetylated units) residues. It can be structurally and functionally modified to enhance gene transfer efficacy.[40,77]

1.5.4 Gadomer

The contrast agent Gadomer was used to measure permeability in tumor blood vessels by DCE-MRI (Paper IV), and the results were compared to relevant parameters obtained with CLSM. Gadomer is a synthetic dendritic gadolinium (Gd) chelate carrying 24 Gd. Each of the 24 amino groups of the outmost 12 L-lysine residues are covalently linked to a macrocyclic Gd complex, resulting in a high Gd density per molecule. Gadomer has a molecular weight about 17 kDa. Because of the globular shape of the molecule, the apparent molecular weight is about 30 - 35 kDa.[62] Gadomer is developed as an intravascular agent, but due to the leakiness of tumor blood vessels it extravasates in tumor tissue. The acute systemic tolerance of Gadomer is high and it is rapidly and completely eliminated from the body mainly via glomerular filtration.[62] The T_1 relaxivity of Gadomer at 7T have been estimated to 7 $mM^{-1}s^{-1}$ (personal communication, Bayer Schering Pharma AG, Berlin, Germany, March 2009).

1.6 Model systems

1.6.1 Hydrogels

A 5% gelatin hydrogel was used to mimic the collagen network of ECM in tissue (0.2 - 2%)[78,79] and diffusion of dextrans and IgG was measured by FCS (Paper I). Gelatin is produced by partially hydrolysis of collagen. By heating, the molecular bonds that provide stability to the triple helical structure of collagen are broken. When the melted gelatin is cooled, the hydrogen bonds reestablish in a random fashion and the gelatin strands assemble into a gel network.

1.6.2 Cell lines

Intracellular experiments (in vitro transfection, gel electrophoresis, flow cytometry, CLSM, and FCS) of DNA-chitosan polyplexes were performed using human embryonic kidney 293 cells (HEK293) obtained from ATCC (Rockville, MD, USA) (Paper III).

The human osteosarcoma cell line (OHS) was established at the Norwegian Radium Hospital from a patient with multiple skeletal manifestations of osteosarcoma.[80] In the present work, OHS cells were used for growing multicellular spheroids (Paper I) and for xenografts growing in the intravital window chamber model (Paper IV).

1.6.3 Multicellular spheroids

Multicellular spheroids of OHS cells were used to mimic the ECM of tumor tissue, and diffusion of dextrans and IgG was measured by FCS (Paper I). A multicellular spheroid consists of cells growing in a 3D structure.[81] Multicellular spheroids simulate micrometastases or intravascular microregions of larger tumors, and show growth kinetics similar to those of tumors in vivo. OHS spheroids produce ECM with an intermediate composition to that of xenografts and monolayers.[82]

1.6.4 Dorsal window chambers

Tumors growing in observation chambers in animals give a unique opportunity for intravital studies of tumor pathophysiology.[71,72,83] OHS cells were grown in dorsal window chambers, and implanted in nude mice as described by Endrich *et al.*[84] to provide a vascular tumor model for combined CLSM and MRI (Paper IV). For this purpose, window chambers in MRI-compatible material, poloxy methylene (POM), were produced (Fig. 4). The plastic chambers resemble traditional titanium chambers but the size was made smaller to reduce the burden on the animal. A device for fixing the chamber to the MRI surface coil was produced to prevent movement artifacts during imaging.

a)

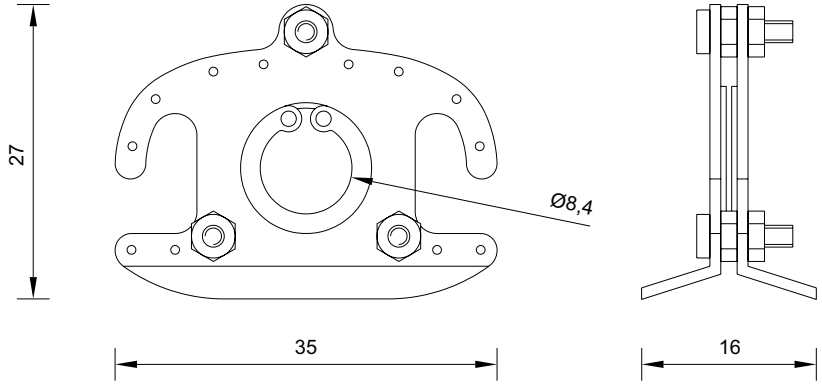

b)

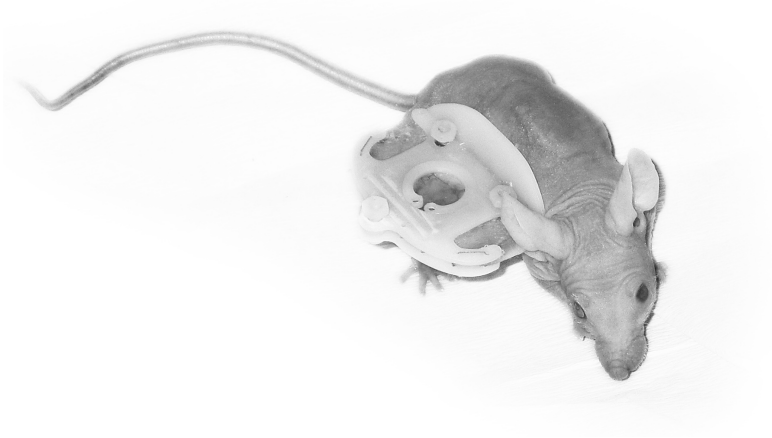

Figure 4. a) Schematic drawing of dorsal window chamber in MRI-compatible material (POM). The hole in the centre is covered by a transparent glass cover slip which is fixed with a clamping ring. The chamber has a total weight of 2.0 g. All parts were produced by the in-house workshop, except for the glass cover slip (Assistent, Germany) b) The MRI-compatible dorsal window chamber implanted in a nude mouse. A circular area is removed from one layer of skin under the glass cover slip, providing a window to the tissue.

2 Objectives of the study

New approaches to drug delivery strive to develop target-selective nanomedicine in order to minimize systemic side-effects. The overall motivation for the present work was to establish robust and accurate tools for determining characteristic properties of nanomedicine and tissue, and for understanding the transport mechanisms in the various tissue subcompartments.

The enhanced permeability of tumor vasculature facilitates passive transport across the capillary walls, and is a source of selective cancer therapy. It has been shown that the permeability may be related to the microvascular structure of the tissue.[14,85-88] DCE-MRI has frequently been used to study vascular permeability of tumor tissue,[58,59,89] but limited spatial resolution makes the technique unsuitable to detect the extensive heterogeneity of tumor tissue. We therefore aimed at complementing DCE-MRI with CLSM to detect local variations in permeability and microvascular morphology. The dorsal window chamber allowed intravital imaging of the same tissue with both methods, and has recently received attention as a potential tumor model for multimodal imaging with MRI.[90,91]

A prerequisite for successful therapy is that the therapeutic agents reach the target cells. Because of the elevated IFP in tumors, both transvascular and interstitial transport of nanomedicine largely depend on diffusion, which is extremely slow for these large sized molecules. It is therefore important to establish methods for studying the nature of diffusion and the properties of nanomedicine and tissue that influence this transport mechanism. We sought to establish FCS as a method for studying interstitial diffusion.

The success of the human genome project has made it possible to diagnose errors in genes. The next challenge is to develop gene therapy based on this knowledge. The size and negative charge of the DNA molecule constitute a barrier to gene delivery and effort is made to develop vectors with properties that facilitate transport, uptake, and transfection efficacy. Chitosan is a nonviral vector which can be structurally modified in order to enhance gene delivery efficacy.[40,47,69,77,92] We wished to explore how various structural properties of chitosan influenced the DNA condensation and the delivery of the DNA-chitosan polyplexes.

The specific aims of the present work were to:

- design an MRI-compatible dorsal window chamber in order to investigate the potential of CLSM and MRI as complementary techniques.

- study microvascular structure and transvascular transport in OHS tumor tissue with CLSM and MRI using the dorsal window chamber model.

- establish FCS as a method for studying extracellular diffusion and correlate results with previously measured diffusion by FRAP.

- establish protocols for fluorescent dual-labeling of DNA-chitosan polyplexes for CLSM and FCS studies.

- characterize DNA-chitosan polyplexes formed by structurally different chitosans.

- study the effect of structural modification of chitosan on intracellular trafficking, dissociation, and transfection efficacy of DNA-chitosan polyplexes in cells.

3 Summary of results

Paper I

FCS was used to study extracellular diffusion of IgG and tetramethylrhodamine(TMR)-labeled dextrans (155 kDa and 2 MDa). A 5% hydrogel and OHS spheroids were used to mimic the extracellular matrix in tissue. The novel aspect of this work was to apply FCS for extracellular diffusion measurements in spheroids. The diffusion coefficients were shown to depend on the complexity of the environment, as well as on the size and structural shape of the diffusing molecules. The results were validated by comparison to diffusion coefficients previously obtained with two-photon fluorescence recovery after photobleaching (FRAP) using the same microscope (Zeiss LSM510 META/Confocor2). However, FCS provided additional information to FRAP by revealing anomalous subdiffusion or two-component diffusion.

Paper II

For the purpose of investigating the structure-function relationship of chitosan as a gene vector, we characterized condensation of DNA in solution by three molecularly tailored chitosans, including linear (LCO), trisaccharide substituted- (TCO), and self-branched trisaccharide substituted (SB-TCO) chitosan oligomers. We used FCS, AFM, and DLS to characterize size, structure, and mobility of the polyplexes, as well as interactions between DNA and chitosan. All three chitosans formed complexes with shapes of globules and rods, and almost no toroids were seen. The asphericity distribution showed that SB-TCO formed a higher fraction (0.84) of globules than LCO (0.58) and TCO (0.61). AFM topographs also revealed that the average heights of SB-TCO were larger than for LCO and TCO for both globules and rods. Using an A/P ratio of 10, we observed a lower fraction of bound chitosan (30%) after complexation of DNA with SB-TCO than with LCO and TCO. We sought to establish a protocol for fluorescently dual-labeling of the polyplexes. FCCS was performed and demonstrated that DNA and chitosan were bound together. Several fluorescent DNA-labels were tested, and YOYO-1 had less effect on the size and structure of the complexes than Cy5 and PicoGreen.

Paper III

The structure-function relationship of chitosan gene delivery was studied intracellularly in HEK293 cells. By varying the A/P ratio and the substitution (LCO and TCO) and chain length (DP_n 21 – 88) of the chitosans, we studied the relationship between these parameters and formulation properties, cellular uptake of polyplexes, and gene transfer efficacy. At a given A/P ratio the various chitosans formed complexes with similar uptake but highly variable transfection efficacy. The maximum gene expression was achieved with DP_n 31-42 and an increase in chain length and A/P ratios reduced and delayed luciferase expression. The gene transfer pattern correlated with the heparin induced unpacking of polyplexes. Substituting the chitosan by uncharged oligosaccharides weakened the interaction with DNA and reduced or enhanced transfection efficacy, depending on the chain length and A/P ratio. The magnitude of gene expression was also controlled by the size of the substituent. CLSM and FCS demonstrated that the polyplexes were internalized as aggregates and that they were transported to the nucleus. Furthermore, FCS revealed that free chitosan was diffusing in the cytoplasm and the nucleus.

Paper IV

For the purpose of combining CLSM and MRI for studying microvascular architecture and function of tumor tissue, we designed a dorsal window chamber in MRI-compatible material (POM). We then applied CLSM and DCE-MRI to study microvascular structure and permeability of OHS tumors growing in dorsal window chambers implanted in mice. The volume transfer coefficient and the time-to-peak extracted from the DCE-MRI concentration-time curves of Gadomer were shown to correlate with the extravasation rate and initial slope of the fluorescence intensity-time curves of 40 kDa dextran, respectively. However, CLSM was able to discriminate between tumors and normal tissue, whereas DCE-MRI was not. Furthermore, the extravasation rate correlated with vascular density, number of branching points, and fractal dimension, which were all significantly higher in tumors than in normal tissue. A high degree of heterogeneity within a tumor was observed.

4 General discussion

A number of techniques were applied to study the delivery of nanomedicine to tissue. We investigated molecular structures and interactions (Paper II, III), and measured transvascular (Paper IV), extracellular (Paper I), and intracellular (Paper III) transport of macromolecules. In such complex environments a wide range of error sources may interfere with the results. We therefore compared several techniques for validation of the results. In light of our results, the following sections will briefly describe vascular, interstitial, and intracellular aspects of drug delivery. The potentials of the main applied techniques (CLSM, MRI, and FCS) will also be discussed.

4.1 Transport of nanomedicine from vasculature to intracellular targets

4.1.1 Transvascular transport and microvascular architecture

Abnormal vasculature and enhanced permeability are characteristics of tumors and may predict therapeutic response.[93-97] To study these phenomena in OHS tumors, extravasation of Gadomer and 40 kDa dextran was successfully measured by CLSM and DCE-MRI, respectively (Paper IV). The two techniques yielded correlating results. Vascular permeability has previously been shown to vary with tumor model, stage, and properties of the molecular tracer.[18-20,58,59,61] In the present work, both CLSM and DCE-MRI indicated lower extravasation of the respective tracers compared to previously measured results.[59,98] Although we used different model systems (tumor model, molecular tracer, and animal), our results may indicate that the permeability of OHS tumor vessels is not very enhanced, even if a difference in extravasation and microvascular structure compared to normal tissue was found in the present work (Paper IV).

Fractal dimension is a structural parameter that gives information about vascular architecture, tumor growth and angiogenesis.[31] In the present study, fractal dimension was shown to correlate positively with extravasation and structural parameters like vascular density, vascular volume fraction, and the number of branching points (Paper IV). However, whereas structural parameters, e.g. the vascular density, vary for different tumor types, the fractal dimension is shown to be a robust, reproducible, and

reliable parameter.[23,30] The strong correlation between extravasation and structural parameters demonstrated in this work supports that microvascular structure can predict transvascular transport of macromolecules. Few previous studies have directly related permeability to microvasculature structure using dorsal window chambers.[90]

Both transvascular and interstitial transport is largely obstructed by the elevated IFP in tumors. The abnormal vasculature in tumors may contribute to malignant properties and prevent successful delivery of therapeutic anti-cancer agents. It has been demonstrated that normalization of the vasculature by applying anti-angiogenetic therapies leads to less leaky and less tortuous vessels, lower IFP, and improved penetration of drugs.[86-88,99-101] This implies that also interstitial transport may be determined by the microvascular architecture.

4.1.2 Interstitial transport; diffusion

The high IFP in the central parts of a tumor induces an outward pressure gradient, and macromolecular therapeutic agents at the periphery of the tumor have to diffuse through the interstitial space against this gradient to penetrate into the tumor.[9,14] The study of mechanisms that determine interstitial diffusion is therefore of high importance to improve the diagnosis and treatment of tumors.

The constituents of the ECM, including collagen, glycosaminoglycans, and proteoglycans, form a complex structured gel that obstructs mobility of macromolecules.[73] This was demonstrated by retarded diffusion of IgG and 155 kDa and 2 MDa dextrans in 5% hydrogel and extracellularly in OHS spheroids compared to solution (Paper I). The concentration of collagen in the ECM may be an important determinant of diffusion.[72,78,102,103] The 5% gelatin hydrogel has comparable collagen density to that of ECM in tissue (0.2 - 2%),[78,79] and was therefore considered a relevant model for tumor ECM. The collagen content in OHS spheroids is lower (0.05%, unpublished data). At a given depth into the spheroids, the effect of the ECM network on diffusion depended on the molecular weight of the tracer (Paper I). The two smaller molecules diffused more slowly in the gel than in spheroids. However, the ECM of spheroids seemed to be a significant barrier for a larger molecules (Paper I), as suggested by a slower diffusion of 2MDa dextran in spheroids than in gel. However, interstitial diffusion depends not only on the weight, but also on structure of the diffusing molecule (Paper I). When one-component (free or anomalous) diffusion was estimated, diffusion of the globular IgG was faster than that of the similar-sized linear

dextran in solution, gel, and spheroids. Berk *et al.*[104] previously demonstrated the same tendency in solution, but contradictory results have also been reported.[70]

In complex, heterogeneous environments, the mobility of molecules may not be sufficiently described by free diffusion. Anomalous diffusion in the interstitium due to various underlying processes has been suggested (e.g. molecular binding, adsorption to chains of the structural meshwork, and molecular crowding).[34,105,106] Another hypothesis is that the interstitial space consists of two phases; a viscous gel compartment containing mainly collagen, elastin, and polysaccharides, and a free-fluid space.[13,107] Diffusion in the free-fluid space has been shown to be close to that in water both in tumors and normal tissue. The higher effective diffusion coefficients that have been measured in tumors compared to normal tissue[108,109] have therefore been attributed to less resistance to macromolecular transport in the gel space of the tumors. This hypothesis has been supported by lower amounts of glycosaminoglycans found in several tumors.[110] However, enhanced diffusion in tumors may also be explained by a larger interstitial space than in normal tissue, which may cause less resistance to diffusion.[13] We demonstrated that diffusion in gel and spheroids could be equally well described by an anomalous and a two-compartment model (Paper I). Studying whether the diffusion mechanism in the interstitium is better described by free, anomalous, or two-compartment diffusion may give valuable information about the structural properties of the ECM.

4.1.3 Intracellular transport

The final target of the therapeutic agents is the cell itself or an intracellular structure. Insight into endocytic pathways and intracellular trafficking is a prerequisite for successful drug delivery. In the present work intracellular transport was investigated by studying chitosan-mediated gene delivery (Paper III).

Chitosan is a nonviral vector that can be structurally modified. Several studies of DNA-chitosan polyplexes have been performed in order to gain basic insight into the complexation mechanisms and the effect of structural modification, both in solution (paper II) and in cells (paper III).[40,47,66,67,69] We complexed DNA with chitosan of different chain lengths and degrees of substitution, including unsubstituted (LCO), trisaccharide substituted (TCO), and self-branched trisaccharide substituted chitosan oligomers (SB-TCO), and demonstrated that these parameters, as well as A/P ratio,

influenced the size, structure, mobility and transfer efficacy of DNA-chitosan polyplexes (Paper II and III).

DNA-chitosan polyplexes have been shown to take various forms; rods, toroids, and globules.[66,67] At A/P 10, DNA condensed by SB-TCO in solution formed larger complexes with a higher fraction of globules to rods than LCO and TCO (Paper II). The length of the DNA used in the present study was 6.7 kb. It has been reported that the length of the DNA is a determinant of the resulting polyplex structure. Whereas a minimum length of about 400 bp has been reported for the formation of toroids,[39,111] it has been suggested that above a certain length, DNA will condense into globules rather than rods. The larger structures of complexes formed by SB-TCO, which was the longer chitosan, may be due to more efficient binding. For longer chitosans, fewer molecules may be necessary to condense DNA, which can explain why SB-TCO formed a higher fraction of free chitosan after complexation compared to LCO and TCO. This is interesting because a high fraction of free polycations may improve the transgene delivery[47,112] due to enhanced buffering capacity leading to endosomal escape of the complexes, and may explain why SB-TCO yields higher transfection efficacy compared to LCO and TCO.[40]

It has previously been demonstrated that low molecular weight chitosan oligomers (DP_n 18-25) mediate more efficient gene transfer than heavier chitosans (210 kDa).[47] In the present study, we identified a narrow interval of chain lengths between DP_n 30-40 that mediated superior transgene expression irrespective to the A/P (Paper III). This enhanced transfection efficacy may be due to more efficient cellular processing of the delivered DNA rather than more efficient delivery of DNA into the cells. Intracellular diffusion of polyplexes demonstrated two diffusing components (Paper III). The fast diffusing component was comparable to that in solution (Paper II) and in cells transfected by free chitosan (Paper III). The fast component was therefore identified as free chitosan. The slow diffusion component in cells (Paper III) was in the lower range of what was found for the respective complexes in solution (Paper II). The slow diffusion may thus origin from complexes diffusing in a more viscous media than solution. It may also arise from complexes, or even free chitosan, that have aggregated or bound to mobile cellular components. Aggregation could also be observed in confocal images (Paper III) but the images revealed no differences between DP_n 31 and 88 in polyplex unpacking and intracellular trafficking that could explain a difference in transfection efficacy. We showed that polyplex formed by linear chitosan at A/P 10 contained about 50% of free unbound chitosan (Paper II) and it seemed like this free chitosan also entered the cells together with the polyplexes (Paper III). The presence of

chitosan in the cytosol and nucleus indicates that chitosans and polyplexes are able to escape lysosomal degradation and are transported to the nucleus.

In this work we showed that substitution of chitosan determined the polyplex structure and mobility (Paper II) which may be related to intracellular trafficking. We further demonstrated that A/P ratio as well as chitosan chain length and substitution influenced the intracellular uptake and transfection efficacy (Paper III).

4.2 The potential of CLSM and MRI as complementary techniques

Microvasculature and vascular permeability of solid tumors may determine therapeutic response and it is of clinical relevance to develop robust methods that quantify these parameters. MRI is frequently used for determining permeability and structural features of tumors.[20,59,90,113-115] However, because tumors are functionally and structurally highly heterogeneous, there are local variations within a tumor that may not be detectable by MRI due to the limited spatial resolution of the technique. By complementing MRI with CLSM we sought to investigate these local variations on a microscopic level and to validate results obtained with MRI.

By using 40 kDa dextran and Gadomer as macromolecular tracers for CLSM and DCE-MRI, respectively, permeability and microvascular structure of OHS tumors growing in dorsal window chambers in mice were studied (Paper IV). For relevant comparison, the two techniques were applied on the same animal. Correlation in permeability was found for the two methods. However, a difference in permeability between normal and tumor tissue was detectable by CLSM, but not by DCE-MRI. This may be due to the differences in the CLSM and MRI experimental setups, which are discussed below.

4.2.1 ROIs and measuring depth in the tissue

A limiting factor of CLSM is the short penetration depth in tissue. Whereas the maximum penetration depth for CLSM was 50 - 140 μm dependent on the tissue, the whole tumor depth was accessible with MRI. Also, whereas the optical section in CLSM was 4.5 μm, DCE-MRI required a larger slice thickness (0.3 mm) for sufficient signal-to-noise ratio. Thus, the measuring depth and the slice thickness of the analyzed tissue were different for the two techniques.

Whereas the CLSM analysis of permeability was performed based on vascular mask of the images (FOV $460.68 \times 460.68\ \mu m^2$), the DCE-MRI ROIs were defined as the 3D volume demonstrating signal enhancement in the chamber. It was our intension to perform pixel-based DCE-MRI analysis.[116] Using this technique the heterogeneity of the tissue detected by DCE-MRI would be taken into account, and coregistration with CLSM could provide information about processes within a single MRI voxel. Due to the thin tissue slice confined in the chamber (~ 0.5 mm for tumors, < 0.5 mm for normal tissue), the SNR was too low to allow pixel-based DCE-MRI.

4.2.2 Molecular tracers

The reason why CLSM detected differences between tumors and normal tissue, whereas DCE-MRI did not, may be the use of different molecular tracers. In a previous study using Gadomer as a contrast agent, a higher permeability was demonstrated in infarcted myocardium compared to normal myocardium, whereas no difference was found between tumor and normal tissue.[58] Ideally, CLSM and DCE-MRI should be performed simultaneously and with the use of the same molecular tracer. In the present work, the multimodal contrast agent AlbuminGd-DTPA (~ 90 kDa) was synthesized according to the procedure described by Ogan,[117] fluorescently labeled and applied (data not shown), but extravasation in OHS tumors was not detected by CLSM or MRI. High-performance liquid chromatography (HPLC) analysis of AlbumGd-DTPA revealed a polydispersity with molecular weights up to 600 kDa, and molecules of this size were not expected to extravasate. We therefore chose the smaller and highly soluble contrast agent Gadomer, which is considered an intravascular contrast agent which extravasates only in diseased tissue.[61] Gadomer17, a precursor of Gadomer, has previously been fluorescently labeled with fluorescein isothiocyanate (FITC).[118] However, all amines on Gadomer are occupied by Gd and it can not be fluorescently labeled.[62] We therefore chose a similar-sized, well characterized, fluorescently labeled dextran (40 kDa) for CLSM.

4.2.3 Mathematical models applied for extracting permeability parameters

The Patlak[119] and Tofts[114] models were the main mathematical models successfully applied to the CLSM and DCE-MRI data, respectively. The more simplified Patlak model requires fewer input parameters and has previously been used to estimate apparent permeability of 40 kDa dextran in P22 sarcomas in rats using the dorsal window chamber model.[98] Whereas the Patlak model assumes irreversible leakage, the

Tofts model take into account the efflux from the tissue compartment into the blood, which may be a more realistic model. The fact that the two models describe somewhat different processes could be a source of error. However, the validity of the Patlak model for tumor tissue was evident by the increasing, linear terminal slope.

4.2.4 The dorsal window chamber

The vascular system of human tumor xenografts growing in dorsal window chambers in nude mice provides an opportunity to extract experimental parameters unavailable in avascular tumor models. A drawback of this model is that the tissue pressure may be elevated and lead to pressure necrosis.[120] Another concern regarding this model is that the risk of infections, which is relatively high, could give artifacts because enhanced vascular permeability is also observed in inflammatory and infected tissue.[121] Tumor tissue may still be identified because macromolecules are cleared more rapidly from normal inflammatory tissue compared to tumor tissue. In this work, an MRI-compatible dorsal window chamber was produced. The size of the chamber was reduced and the material (POM) lighter compared to its titanium counterpart, significantly reducing the stress on the animals and thereby the risk of infections. Although few studies have been published, there is an interest in utilizing dorsal window chambers to cross-validate results from MRI and optical imaging.[90,91,122]

Despite the different basic principles and the different experimental setups of CLSM and MRI, our work shows that the MRI-compatible dorsal window chamber allows combining CLSM and MRI to yield complementary and supportive information about macromolecular permeability in tumors. It has also shown to be a valuable model in revealing the relation between permeability and microvascular structure represented by vascular density, vascular volume, and fractal dimension.

4.3 FCS as a tool for characterizing mobility and molecular interactions in tissue

One-photon FCS was successfully applied as a method for measuring interstitial diffusion in tissue (Paper I). The novel aspect of this work was the use of FCS to measure extracellular diffusion in multicellular spheroids. The diffusion coefficients obtained by FCS were validated with diffusion coefficients measured by two-photon FRAP on the same microscope, showing that these two techniques can support each other. However, FCS is a more sensitive method than FRAP and can detect translational

and rotational diffusion, interactions, concentrations, conformation changes, and triplet state kinetics.[56,123-125] Due to the high sensitivity, FCS can also reveal anomalous sub-diffusion or multiphase diffusion (Paper I) and thus provide additional information to FRAP.

FCS was further used for measuring kinetics and interactions of DNA-chitosan polyplexes (Paper II and III). Effort was made to choose suitable fluorophores (Paper II) for dual-labeling of the polyplexes in order to perform cross-correlation (FCCS) in future cell experiments. In intracellular experiments, FCCS is a valuable tool for verifying that DNA and chitosan are bound together,[125,126] whereas autocorrelation analysis may mistake aggregates or binding to cellular compartments for being complexes. Alexa Fluor 647 and YOYO-1 (both from Molecular Probes, Eugene, OR) was chosen as labels for chitosan and DNA, respectively. YOYO-1 has previously been used as a fluorescent DNA-label in confocal imaging.[127-129] A problem with FCCS of the dual-labeled DNA-chitosan complexes was the large extent of free chitosan, which contributed to a very high count rate for the Alexa Fluor 647 fluorescence. We therefore had to minimize the concentration, which resulted in a very low DNA concentration and a low YOYO-1 count rate. This was not a problem in solution (Paper II), but in cells the YOYO-1 signal was suppressed by the background autofluorescence. Removal of free chitosan was not considered an alternative because it may be disadvantageous for gene transfer efficacy, and we therefore focused on autocorrelation analysis of intracellular mobility and localization of single-labeled DNA-chitosan with Alexa Fluor 647 (Paper III). The ability of FCS to simultaneously detect two diffusing components made it possible to determine the fraction of free chitosan and chitosan bound to complexes (Paper II and III), which provides valuable information about interactions between DNA and chitosan.

Both extra- and intracellular FCS measurements were difficult due to complex and heterogeneous environments. The high sensitivity of the technique makes it vulnerable to scattering, autofluorescence, and photobleaching in cellular environments, and the maximum depth for performing one-photon FCS in tissue is limited. FCS measurements were performed 30 μm into spheroids (Paper I), and the signal quickly diminished with increasing depth. However, by using two-photon FCS and the dorsal window chamber model, Alexandrakis showed that the maximum measuring depth for FCS in solid tumors was 140 μm for 2 MDa dextran and 120 μm for IgG.[54] In intracellular FCS experiments, a complicating factor is that the DNA-chitosan complexes tend to aggregate at physiological pH (Paper II).[40] Aggregation or binding of complexes to the cell membrane may cause FCS to fail as a method, either due to high concentrations

inducing low SNR, too slow diffusion for the accessible time window of the LSM/Confocor2 software, or immobile complexes. In such cases, the autocorrelation function may be distorted or artifacts may yield erroneous quantitative values. FCS should therefore be supported by other methods when performed in complex environments. In Paper I, this was accomplished by comparing FCS and FRAP. In Paper III, the problem was circumvented by qualitatively comparing FCS results for the various chitosans. In Paper II, FCS was qualitatively validated by AFM and DLS. The results obtained in complex environments, like spheroids and cells, were thus supported by other techniques and by pre-characterization of mobility in solution. FCS is, however, a valuable tool for measuring diffusion and detecting molecules where concentrations are too low for detection by other techniques, e.g. CLSM. Therefore, studies of DNA-chitosan with FCCS and CLSM can be performed simultaneously in the same cell and give complementary information about co-localization, kinetics, and interactions. Further effort will be made to establish protocols for intracellular FCCS.

This work has shown that FCS is a versatile method in drug delivery research. Although FCS is a challenging technique in complex environments, we have demonstrated its potential in characterizing molecular structure, mobility, and interactions in solution (Paper I and II), as well as extracellularly in spheroids (Paper I) and in cells (Paper III).

5 Conclusion and future perspectives

Novel and well established methods were used to study structural and functional parameters of tissue. The versatility of fluorescent techniques in studying drug delivery was demonstrated. The confocal microscope was used to validate or support results obtained with a number of other techniques in characterizing extracellular, intracellular and transvascular transport and uptake of nanomedicine.

Permeability in tumor tissue measured by DCE-MRI correlated with results obtained by CLSM, and a relation between microvascular morphology and permeability was observed. This demonstrated that the dorsal window chamber model allowed us to obtain complementary information about structure and function of tumor vasculature by using CLSM and MRI. We designed an MRI-compatible dorsal window chamber which proved to be well functioning for both techniques. The chamber is now ready to be used in combined CLSM and MRI for studying a variety of parameters. The experimental setup may be improved by further optimizing the MRI protocols, and designing a dedicated surface coil may increase the SNR. There is an increasing interest in multimodal imaging and a number of multimodal MRI contrast agents for various applications exist.[130] For future experiments, effort will be made in finding multimodal tracers with suitable properties that can be used both as MRI contrast agents and as fluorescent tracers in CLSM.

The sensitivity of FCS to background noise and autofluorescence constituted a challenge when performing experiments in living tissue. However, FCS proved to be a suitable technique for diffusion measurements both intra- and extracellularly. FCS was successfully used to measure diffusion extracellularly in spheroids and the results corresponded well with previously obtained FRAP measurements on the same microscope and with the same molecular tracers. Extracellular diffusion was shown to depend on molecular weight, structure, and the complexity of the model system. FCS provided additional information to FRAP by revealing a two-phase or an anomalous nature of the transport in gel and spheroids. Hence, to further explore the nature of diffusion in the interstitium may give valuable information about the structural properties of the ECM.

FCS provided new information about the functional and morphological variations of structurally modified gene vectors. By studying the structure-function relationship of chitosan, we sought to determine the relationship between structure and transfection efficacy. In combination with other techniques, FCS revealed that the A/P ratio, chain length, and the degree of substitution of chitosan affected the size, structure, mobility, extent of free chitosan after complexation, aggregation, and transfer efficacy of DNA-chitosan polyplexes. The results are interesting with respect to transfection in several manners. A high fraction of free chitosan may be advantageous for endosomal release,[40] and could be a determinant of transfection efficacy. Free chitosan was detected by FCS in the cytoplasma and the nucleus, which indicates that the polyplexes are able to escape lysosomal degradation and be transported to the nucleus. In conclusion, the results gave no clear evidences on how the transfection efficacy is determined by the chitosan structure. The studies on condensation, uptake, and intracellular trafficking of DNA complexed with structurally modified chitosans in cells will therefore be continued. For future experiments, we will further optimize the protocol for fluorescent dual-labeling in order to perform intracellular FCCS. The high count rate from unbound fluorescently labeled chitosans diminished the fluorescence signal from labeled DNA, and this is a challenge that must be overcome. We will therefore seek to find fluorophores with more sufficient properties for our purpose. Removal of the free chitosan may not be favorable to transfection, but if the fluorescence of the chitosan label is sufficiently high, the detected count rate may be reduced by labeling only a fraction of the chitosans in the sample.

The present work has demonstrated the potential of FCS, CLSM, MRI, and other techniques applied in the study as valuable tools in drug delivery research. By further improving the experimental setups, these techniques may provide new and complementary insight into the structure and function of the vascular, extracellular, and intracellular tissue compartments.

References

1. Duncan, R. Nanomedicines in action. *Pharm J* **273**, 485-488 (2004)
2. Wagner, V.; Dullaart, A.; Bock, A.K.; Zweck, A. The emerging nanomedicine landscape. *Nat Biotechnol* **24**, 1211-1217 (2006)
3. Moghimi, S.M.; Hunter, A.C.; Murray, J.C. Nanomedicine: current status and future prospects. *FASEB J* **19**, 311-330 (2005)
4. Davies, C.deL.; Lundstrom, L.M.; Frengen, J.; Eikenes, L.; Bruland, Ø.S.; Kaahus, O.; Hjelstuen, M.H.B.; Brekken, C. Radiation improves the distribution and uptake of liposomal doxorubicin (Caelyx) in human osteosarcoma xenografts. *Cancer Res* **64**, 547-553 (2004)
5. Eikenes, L.; Bruland, Ø.S.; Brekken, C.; Davies, C.deL. Collagenase increases the transcapillary pressure gradient and improves the uptake and distribution of monoclonal antibodies in human osteosarcoma xenografts. *Cancer Res* **64**, 4768-4773 (2004)
6. Jain, R.K.; Baxter, L.T. Mechanisms of heterogeneous distribution of monoclonal-antibodies and other macromolecules in tumors - significance of elevated interstitial pressure. *Cancer Res* **48**, 7022-7032 (1988)
7. Jain, R.K. Determinants of tumor blood-flow - a review. *Cancer Res* **48**, 2641-2658 (1988)
8. Jain, R.K.; Wardhartley, K. Tumor blood-flow - characterization, modifications, and role in hyperthermia. *IEEE Transactions on Sonics and Ultrasonics* **31**, 504-526 (1984)
9. Jain, R.K. Vascular and interstitial barriers to delivery of therapeutic agents in tumors. *Cancer Metastasis Rev* **9**, 253-266 (1990)
10. Boucher, Y.; Jain, R.K. Microvascular pressure is the principal driving force for interstitial hypertension in solid tumors - implications for vascular collapse. *Cancer Res* **52**, 5110-5114 (1992)
11. Boucher, Y.; Baxter, L.T.; Jain, R.K. Interstitial pressure-gradients in tissue-isolated and subcutaneous tumors - implications for therapy. *Cancer Res* **50**, 4478-4484 (1990)
12. Eikenes, L.; Tari, M.; Tufto, I.; Bruland, Ø.S.; Davies, C.deL. Hyaluronidase induces a transcapillary pressure gradient and improves the distribution and uptake of liposomal doxorubicin (Caelyx (TM)) in human osteosarcoma xenografts. *Brit J Cancer* **93**, 81-88 (2005)
13. Jain, R.K. Transport of molecules in the tumor interstitium - a review. *Cancer Res* **47**, 3039-3051 (1987)

14. Jain, R.K. Transport of molecules across tumor vasculature. *Cancer Metastasis Rev* **6**, 559-593 (1987)
15. Noguchi, Y.; Wu, J.; Duncan, R.; Strohalm, J.; Ulbrich, K.; Akaike, T.; Maeda, H. Early phase tumor accumulation of macromolecules: a great difference in clearance rate between tumor and normal tissues. *Jpn J Cancer Res* **89**, 307-314 (1998)
16. Iyer, A.K.; Khaled, G.; Fang, J.; Maeda, H. Exploiting the enhanced permeability and retention effect for tumor targeting. *Drug Discovery Today* **11**, 812-818 (2006)
17. Matsumura, Y.; Maeda, H. A new concept for macromolecular therapeutics in cancer-chemotherapy -mechanism of tumoritropic accumulation of proteins and the antitumor agent smancs. *Cancer Res* **46**, 6387-6392 (1986)
18. Dreher, M.R.; Liu, W.G.; Michelich, C.R.; Dewhirst, M.W.; Yuan, F.; Chilkoti, A. Tumor vascular permeability, accumulation, and penetration of macromolecular drug carriers. *J Natl Cancer Inst* **98**, 335-344 (2006)
19. Dellian, M.; Yuan, F.; Trubetskoy, V.S.; Torchilin, V.P.; Jain, R.K. Vascular permeability in a human tumour xenograft: molecular charge dependence. *Br J Cancer* **82**, 1513-1518 (2000)
20. Su, M.Y.; Muhler, A.; Lao, X.Y.; Nalcioglu, O. Tumor characterization with dynamic contrast-enhanced MRI using MR contrast agents of various molecular weights. *Magn Reson Med* **39**, 259-269 (1998)
21. Yuan, F.; Salehi, H.A.; Boucher, Y.; Vasthare, U.S.; Tuma, R.F.; Jain, R.K. Vascular-permeability and microcirculation of gliomas and mammary carcinomas transplanted in rat and mouse cranial windows. *Cancer Res* **54**, 4564-4568 (1994)
22. Farma, J.M.; Puhlmann, M.; Soriano, P.A.; Cox, D.; Paciotti, G.F.; Tamarkin, L.; Alexander, H.R. Direct evidence for rapid and selective induction of tumor neovascular permeability by tumor necrosis factor and a novel derivative, colloidal gold bound tumor necrosis factor. *Int J Cancer* **120**, 2474-2480 (2007)
23. Mancardi, D.; Varetto, G.; Bucci, E.; Maniero, F.; Guiot, C. *Theoretical Biology and Medical Modelling* **5**, (2008)
24. Vogel, A.W. Intratumoral vascular changes with increased size of a mammary adenocarcinoma - new methods and results. *J Natl Cancer Inst* **34**, 571-578 (1965)
25. Algire, G.H.; Chalkley, H.W. Vascular reactions of normal and malignant tissues in vivo. I. Vascular reactions of mice to wounds and to normal and neoplastic transplants. *J Natl Cancer Inst* **6**, 73-85 (1945)

26. Leunig, M.; Yuan, F.; Menger, M.D.; Boucher, Y.; Goetz, A.E.; Messmer, K.; Jain, R.K. Angiogenesis, Microvascular Architecture, Microhemodynamics, and Interstitial Fluid Pressure during Early Growth of Human Adenocarcinoma LSI74T in SCID Mice. *Cancer Res* **52**, 6553-6560 (1992)
27. Song, C.W.; Levitt, S.H. Quantitative study of vascularity in Walker carcinoma 256. *Cancer Res* **31**, 587-589 (1971)
28. Song, C.W.; Sung, J.H.; Clement, J.J.; Levitt, S.H. Vascular changes in neuroblastoma in mice following X-irradiation. *Cancer Res* **34**, 2344-2350 (1974)
29. Gullino, P.M.; Grantham, F.H. The vascular space of growth tumors. *Cancer Res* **24**, 1727-1732 (1964)
30. Baish, J.W.; Gazit, Y.; Berk, D.A.; Nozue, M.; Baxter, L.T.; Jain, R.K. Role of tumor vascular architecture in nutrient and drug delivery: An invasion percolation-based network model. *Microvasc Res* **51**, 327-346 (1996)
31. Baish, J.W.; Jain, R.K. Fractals and cancer. *Cancer Res* **60**, 3683-3688 (2000)
32. Sabo, E.; Boltenko, A.; Sova, Y.; Stein, A.; Kleinhaus, S.; Resnick, M.B. Microscopic analysis and significance of vascular architectural complexity in renal cell carcinoma. *Clin Cancer Res* **7**, 533-537 (2001)
33. Gazit, Y.; Berk, D.A.; Leunig, M.; Baxter, L.T.; Jain, R.K. Scale-Invariant Behavior and Vascular Network Formation in Normal and Tumor Tissue. *Phys Rev Lett* **75**, 2428-2431 (1995)
34. Banks, D.S.; Fradin, C. Anomalous diffusion of proteins due to molecular crowding. *Biophys J* **89**, 2960-2971 (2005)
35. Sten-Knudsen, O. Passive transport processes. In *Concept and models*. (ed Tosteson, D.C.) 5-115 (Springer Verlag, Berlin, 1978).
36. Kedem, O.; Katchalsky, A. Thermodynamic analysis of the permeability of biological membranes to non-electrolytes. *Biochim Biophys Acta* **27**, 229-246 (1958)
37. Nguyen, D.N.; Green, J.J.; Chan, J.M.; Langer, R.; Anderson, D.G. Polymeric Materials for Gene Delivery and DNA Vaccination. *Adv Mater* **20**, 1-21 (2008)
38. Minagawa, K.; Matsuzawa, Y.; Yoshikawa, K.; Matsumoto, M.; Doi, M. Direct observation of the biphasic conformational change of dna induced by cationic polymers. *FEBS Lett* **295**, 67-69 (1991)
39. Bloomfield, V.A. Condensation of dna by multivalent cations - considerations on mechanism. *Biopolymers* **31**, 1471-1481 (1991)
40. Strand, S.P.; Issa, M.M.; Christensen, B.E.; Vårum, K.M.; Artursson, P. Tailoring of chitosans for gene delivery: Novel self-branched glycosylated

chitosan oligomers with improved functional properties. *Biomacromolecules* **9**, 3268-3276 (2008)

41. Dinh, A.T.; Pangarkar, C.; Theofanous, T.; Mitragotri, S. Understanding intracellular transport processes pertinent to synthetic gene delivery via stochastic simulations and sensitivity analyses. *Biophys J* **92**, 831-846 (2007)
42. Sonawane, N.D.; Szoka, F.C.; Verkman, A.S. Chloride accumulation and swelling in endosomes enhances DNA transfer by polyamine-DNA polyplexes. *J Biol Chem* **278**, 44826-44831 (2003)
43. Zuber, G.; Dauty, E.; Nothisen, M.; Belguise, P.; Behr, J.P. Towards synthetic viruses. *Adv Drug Deliver Rev* **52**, 245-253 (2001)
44. Xu, Y.H.; Szoka, F.C. Mechanism of DNA release from cationic liposome/DNA complexes used in cell transfection. *Biochemistry* **35**, 5616-5623 (1996)
45. Ogris, M.; Wagner, E. Targeting tumors with non-viral gene delivery systems. *Drug Discov Today* **7**, 479-485 (2002)
46. Chen, H.H.; Ho, Y.P.; Jiang, X.; Mao, H.Q.; Wang, T.H.; Leong, K.W. Quantitative comparison of intracellular unpacking kinetics of polyplexes by a model constructed from quantum Dot-FRET. *Mol Ther* **16**, 324-332 (2008)
47. Köping-Höggård, M.; Vårum, K.M.; Issa, M.; Danielsen, S.; Christensen, B.E.; Stokke, B.T.; Artursson, P. Improved chitosan-mediated gene delivery based on easily dissociated chitosan polyplexes of highly defined chitosan oligomers. *Gene Ther* **11**, 1441-1452 (2004)
48. Schaffer, D.V.; Fidelman, N.A.; Dan, N.; Lauffenburger, D.A. Vector unpacking as a potential barrier for receptor-mediated polyplex gene delivery. *Biotechnol Bioeng* **67**, 598-606 (2000)
49. Magde, D.; Elson, E.; Webb, W.W. Thermodynamic fluctuations in a reacting system - measurement by fluorescence correlation spectroscopy. *Phys Rev Lett* **29**, 705-708 (1972)
50. Rigler, R.; Mets, Ü.; Widengren, J.; Kask, P. Fluorescence correlation spectroscopy with high count rate and low background: analysis of translational diffusion. *Eur Biophys J* **22**, 169-175 (1993)
51. Wachsmuth, M.; Waldeck, W.; Langowski, J. Anomalous diffusion of fluorescent probes inside living cell nuclei investigated by spatially-resolved fluorescence correlation spectroscopy. *J Mol Biol* **298**, 677-689 (2000)
52. Schwille, P.; Haupts, U.; Maiti, S.; Webb, W.W. Molecular dynamics in living cells observed by fluorescence correlation spectroscopy with one- and two-photon excitation. *Biophys J* **77**, 2251-2265 (1999)

53. Weiss, M.; Hashimoto, H.; Nilsson, T. Anomalous protein diffusion in living cells as seen by fluorescence correlation spectroscopy. *Biophys J* **84**, 4043-4052 (2003)
54. Alexandrakis, G.; Brown, E.B.; Tong, R.T.; McKee, T.D.; Campbell, R.B.; Boucher, Y.; Jain, R.K. Two-photon fluorescence correlation microscopy reveals the two-phase nature of transport in tumors. *Nat Med* **10**, 203-207 (2004)
55. Weiss, M.; Elsner, M.; Kartberg, F.; Nilsson, T. Anomalous subdiffusion is a measure for cytoplasmic crowding in living cells. *Biophys J* **87**, 3518-3524 (2004)
56. Clamme, J.P.; Krishnamoorthy, G.; Mély, Y. Intracellular dynamics of the gene delivery vehicle polyethylenimine during transfection: investigation by two-photon fluorescence correlation spectroscopy. *BBA Biomembranes* **1617**, 52-61 (2003)
57. Weisshart, K.; Jüngel, V.; Briddon, S.J. The LSM 510 META - ConfoCor 2 system: an integrated imaging and spectroscopic platform for single-molecule detection. *Curr Pharm Biotechn* **5(2)**, 135-154 (2004)
58. Roberts, H.C.; Saeed, M.; Roberts, T.P.L.; Muhler, A.; Shames, D.M.; Mann, J.S.; Stiskal, M.; Demsar, F.; Brasch, R.C. Comparison of albumin-(Gd-DTPA)(30) and Gd-DTPA-24-cascade-polymer for measurements of normal and abnormal microvascular permeability. *J Magn Reson Imaging* **7**, 331-338 (1997)
59. Verhoye, M.; Boudewijn, P.J.v.d.S.; Rijken, P.; Peters, H.; Van der Kogel, A.J.; Pée, G.; Vanhoutte, G.; Heerschap, A.; Van der Linden, A. *SPIE* **3660**, (1990)
60. Rehman, S.; Jayson, G.C. Molecular imaging of antiangiogenic agents. *The Oncologist* **10**, 92-103 (2005)
61. Weinmann, H.J.; Ebert, W.; Misselwitz, B.; Schmitt-Willich, H. Tissue-specific MR contrast agents. *Eur J Radiol* **46**, 33-44 (2003)
62. Misselwitz, B.; Schmitt-Willich, H.; Ebert, W.; Frenzel, T.; Weinmann, H.J. Pharmacokinetics of Gadomer-17, a new dendritic magnetic resonance contrast agent. *Magn Reson Mat Phys Biol Med* **12**, 128-134 (2001)
63. Fournier, L.S. & Brasch, R.C. In *Dynamic Contrast-Enhanced Magnetic Resonance Imaging in Oncology*. (Springer Berlin, Heidelberg, 2006).
64. Fotiadis, D.; Scheuring, S.; Muller, S.A.; Engel, A.; Muller, D.J. Imaging and manipulation of biological structures with the AFM. *Micron* **33**, 385-397 (2002)
65. Gadegaard, N. Atomic force microscopy in biology: technology and techniques. *Biotech Histochem* **81**, 87-97 (2006)
66. Danielsen, S.; Vårum, K.M.; Stokke, B.T. Structural analysis of chitosan mediated DNA condensation by AFM: Influence of chitosan molecular parameters. *Biomacromolecules* **5**, 928-936 (2004)

67. Danielsen, S.; Maurstad, G.; Stokke, B.T. DNA-polycation complexation and polyplex stability in the presence of competing polyanions. *Biopolymers* **77**, 86-97 (2005)
68. Maurstad, G.; Danielsen, S.; Stokke, B.T. Analysis of compacted semiflexible polyanions visualized by atomic force microscopy: Influence of chain stiffness on the morphologies of polyelectrolyte complexes. *J Phys Chem-US* **107**, 8172-8180 (2003)
69. Strand, S.P.; Danielsen, S.; Christensen, B.E.; Vårum, K.M. Influence of chitosan structure on the formation and stability of DNA-chitosan polyelectrolyte complexes. *Biomacromolecules* **6**, 3357-3366 (2005)
70. Pluen, A.; Netti, P.A.; Jain, R.K.; Berk, D.A. Diffusion of macromolecules in agarose gels: Comparison of linear and globular configurations. *Biophys J* **77**, 542-552 (1999)
71. Schnell, E.A.; Eikenes, L.; Tufto, I.; Erikson, A.; Juthajan, A.; Lindgren, M.; Davies, C.deL. Diffusion measured by fluorescence recovery after photobleaching based on multiphoton excitation laser scanning microscopy *J Biomed Opt* **13**, 064037 (2008)
72. Erikson, A.; Andersen, H.N.; Naess, S.N.; Sikorski, P.; Davies, C.deL. Physical and chemical modifications of collagen gels: Impact on diffusion. *Biopolymers* **89**, 135-143 (2008)
73. Davies, C.deL.; Berk, D.A.; Pluen, A.; Jain, R.K. Comparison of IgG diffusion and extracellular matrix composition in rhabdomyosarcomas grown in mice versus *in vitro* as spheroids reveals the role of host stromal cells. *Br J Cancer* **86**, 1639-1644 (2002)
74. Richardson, S.C.W.; Kolbe, H.V.J.; Duncan, R. Potential of low molecular mass chitosan as a DNA delivery system: biocompatibility, body distribution and ability to complex and protect DNA. *Int J Phar* **178**, 231-243 (1999)
75. Prabaharan, M. Chitosan derivatives as promising materials for controlled drug delivery. *J Biomater Appl* **23**, 5-36 (2008)
76. Issa, M.M.; Köping-Höggård, M.; Artursson, P. Chitosan and the mucosal delivery of biotechnology drugs. *Drug discovery today: Technologies* **2**, 1-6 (2005)
77. Köping-Höggård, M.; Tubulekas, I.; Guan, H.; Edwards, K.; Nilsson, M.; Vårum, K.M.; Artursson, P. Chitosan as a nonviral gene delivery system. Structure-property relationships and characteristics compared with polyethylenimine in vitro and after lung administration in vivo. *Gene Ther* **8**, 1108-1121 (2001)

78. Netti, P.A.; Berk, D.A.; Swartz, M.A.; Grodzinsky, A.J.; Jain, R.K. Role of extracellular matrix assembly in interstitial transport in solid tumors. *Cancer Res* **60**, 2497-2503 (2000)
79. Davies, C.deL.; Engesaeter, B.O.; Haug, I.; Ormberg, I.W.; Halgunset, J.; Brekken, C. Uptake of IgG in osteosarcoma correlates inversely with interstitial fluid pressure, but not with interstitial constituents. *Br J Cancer* **85**, 1968-1977 (2001)
80. Fodstad, Ø.; Brøgger, A.; Bruland, Ø.; Solheim, Ø.P.; Nesland, J.M.; Pihl, A. Characteristics of a cell-line established from a patient with multiple osteosarcoma, appearing 13 years after treatment for bilateral retinoblastoma. *Int J Cancer* **38**, 33-40 (1986)
81. Sutherland, R.M. Cell and environment interactions in tumor microregions - the multicell spheroid model. *Science* **240**, 177-184 (1988)
82. Davies, C.deL.; Muller, H.; Hagen, I.; Garseth, M.; Hjelstuen, M.H. Comparison of extracellular matrix in human osteosarcomas and melanomas growing as xenografts, multicellular spheroids, and monolayer cultures. *Anticancer Res* **17**, 4317-4326 (1997)
83. Tufto, I.; Hansen, R.; Byberg, D.; Nygaard, K.H.H.; Tufto, J.; Davies, C.deL. The effect of collagenase and hyaluronidase on transient perfusion in human osteosarcoma xenografts grown orthotopically and in dorsal skinfold chambers. *Anticancer Res* **27**, 1475-1481 (2007)
84. Endrich, B.; Asaishi, K.; Gotz, A.; Messmer, K. Technical report - a new chamber technique for micro-vascular studies in unanesthetized hamsters. *Res Exp Med (Berl)* **177**, 125-134 (1980)
85. Hashizume, H.; Baluk, P.; Morikawa, S.; McLean, J.W.; Thurston, G.; Roberge, S.; Jain, R.K.; McDonald, D.M. Openings between defective endothelial cells explain tumor vessel leakiness. *Am J Pathol* **156**, 1363-1380 (2000)
86. Kadambi, A.; Carreira, C.M.; Yun, C.; Padera, T.P.; Dolmans, D.E.J.G.J.; Carmeliet, P.; Fukumura, D.; Jain, R.K. Vascular endothelial growth factor (VEGF)-C differentially affects tumor vascular function and leukocyte recruitment: Role of VEGF-receptor 2 and host VEGF-A. *Cancer Res* **61**, 2404-2408 (2001)
87. Tsuzuki, Y.; Fukumura, D.; Oosthuyse, B.; Koike, C.; Carmeliet, P.; Jain, R.K. Vascular endothelial growth factor (VEGF) modulation by targeting hypoxia-inducible factor-1 alpha -> hypoxia response element -> VEGF cascade differentially regulates vascular response and growth rate in tumors. *Cancer Res* **60**, 6248-6252 (2000)

88. Yuan, F.; Chen, Y.; Dellian, M.; Safabakhsh, N.; Ferrara, N.; Jain, R.K. Time-dependent vascular regression and permeability changes in established human tumor xenografts induced by an anti-vascular endothelial growth factor vascular permeability factor antibody. *Proc Natl Acad Sci U S A* **93**, 14765-14770 (1996)
89. Ewing, J.R.; Brown, S.L.; Lu, M.; Panda, S.; Ding, G.L.; Knight, R.A.; Cao, Y.; Jiang, Q.; Nagaraja, T.N.; Churchman, J.L.; Fenstermacher, J.D. Model selection in magnetic resonance imaging measurements of vascular permeability: Gadomer in a 9L model of rat cerebral tumor. *J Cereb Blood Flow Metab* **26**, 310-320 (2006)
90. Gaustad, J.V.; Brurberg, K.G.; Simonsen, T.G.; Mollatt, C.S.; Rofstad, E.K. Tumor vascularity assessed by magnetic resonance imaging and intravital microscopy imaging. *Neoplasia* **10**, 354-362 (2008)
91. van Vliet, M.; van Dijke, C.F.; Wielopolski, P.A.; ten Hagen, T.L.M.; Veenland, J.F.; Preda, A.; Loeve, A.J.; Eggermont, A.M.M.; Krestin, G.P. MR angiography of tumor-related vasculature: From the clinic to the microenvironment. *Radiographics* **25**, S85-U97 (2005)
92. Lavertu, M.; Méthot, S.; Tran-Khanh, N.; Buschmann, M.D. High efficiency gene transfer using chitosan/DNA nanoparticles with specific combinations of molecular weight and degree of deacetylation. *Biomaterials* **27**, 4815-4824 (2006)
93. Kumar, S.; Ghellal, A.; Li, C.; Byrne, G.; Haboubi, N.; Wang, J.M.; Bundred, N. Breast carcinoma: Vascular density determined using CD105 antibody correlates with tumor prognosis. *Cancer Res* **59**, 856-861 (1999)
94. Weidner, N.; Folkman, J.; Pozza, F.; Bevilacqua, P.; Allred, E.N.; Moore, D.H.; Meli, S.; Gasparini, G. Tumor angiogenesis - a new significant and independent prognostic indicator in early-stage breast-carcinoma. *J Natl Cancer Inst* **84**, 1875-1887 (1992)
95. Vermeulen, P.B.; Verhoeven, D.; Hubens, G.; Vanmarck, E.; Goovaerts, G.; Huyghe, M.; Debruijn, E.A.; Vanoosterom, A.T.; Dirix, L.Y. Microvessel density, endothelial-cell proliferation and tumor-cell proliferation in human colorectal adenocarcinomas. *Ann Oncol* **6**, 59-64 (1995)
96. Ellis, L.M.; Takahashi, Y.; Fenoglio, C.J.; Cleary, K.R.; Bucana, C.D.; Evans, D.B. Vessel counts and vascular endothelial growth factor expression in pancreatic adenocarcinoma. *Eur J Cancer* **34**, 337-340 (1998)
97. Duarte, I.G.; Bufkin, B.L.; Pennington, M.F.; Gal, A.A.; Cohen, C.; Kosinski, A.S.; Mansour, K.A.; Miller, J.I. Angiogenesis as a predictor of survival after surgical resection for stage I non-small-cell lung cancer. *J Thorac Cardiovasc Surg* **115**, 652-658 (1998)

98. Reyes-Aldasoro, C.C.; Wilson, I.; Prise, V.E.; Barber, P.R.; Ameer-Beg, S.M.; Vojnovic, B.; Cunningham, V.J.; Tozer, G.M. Estimation of apparent tumor vascular permeability from multiphoton fluorescence microscopic images of P22 rat sarcomas in vivo. *Microcirculation* **15**, 65-79 (2008)
99. Duda, D.G.; Batchelor, T.T.; Willett, C.G.; Jain, R.K. VEGF-targeted cancer therapy strategies: current progress, hurdles and future prospects. *Trends Mol Med* **13**, 223-230 (2007)
100. Jain, R.K. Normalizing tumor vasculature with anti-angiogenic therapy: A new paradigm for combination therapy. *Nat Med* **7**, 987-989 (2001)
101. Fukumura, D.; Jain, R.K. Tumor microenvironment abnormalities: Causes, consequences, and strategies to normalize. *J Cell Biochem* **101**, 937-949 (2007)
102. Pluen, A.; Boucher, Y.; Ramanujan, S.; McKee, T.D.; Gohongi, T.; di Tomaso, E.; Brown, E.B.; Izumi, Y.; Campbell, R.B.; Berk, D.A.; Jain, R.K. Role of tumor-host interactions in interstitial diffusion of macromolecules: Cranial vs. subcutaneous tumors. *Proc Natl Acad Sci U S A* **98**, 4628-4633 (2001)
103. Ramanujan, S.; Pluen, A.; McKee, T.D.; Brown, E.B.; Boucher, Y.; Jain, R.K. Diffusion and convection in collagen gels: Implications for transport in the tumor interstitium. *Biophys J* **83**, 1650-1660 (2002)
104. Berk, D.A.; Yuan, F.; Leunig, M.; Jain, R.K. Fluorescence photobleaching with spatial fourier-analysis - measurement of diffusion in light-scattering media. *Biophysical J* **65**, 2428-2436 (1993)
105. Saxton, M.J. Anomalous diffusion due to binding: A Monte Carlo study. *Biophys J* **70**, 1250-1262 (1996)
106. Fadda, G.C.; Lairez, D.; Arrio, B.; Carton, J.P.; Larreta-Garde, V. Enzyme-catalyzed gel proteolysis: an anomalous diffusion-controlled mechanism. *Biophys J* **85**, 2808-2817 (2003)
107. Wiederhielm, C.A. Dynamics of capillary fluid exchange: A nonlinear computer simulation. *Microvasc Res* **18**, 48-82 (1979)
108. Nugent L J.; Jain R K. Extravascular diffusion in normal and neoplastic tissues. *Cancer Res* **44**, 238-244 (1984)
109. Clauss, M.A.; Jain, R.K. Interstitial transport of rabbit and sheep antibodies in normal and neoplas tic tissues. *Cancer Res* **50**, 3487-3492 (1990)
110. Gullino P M. Extracellular compartments of solid tumors. (ed Becker, F. F.) In *Cancer a comprehensive treatise,* **3** *ISBN 0-306-35203-6* 327-354 (1975)
111. Widom, J.; Baldwin, R.L. Cation-induced toroidal condensation of dna studies with co3+(nh3)6. *J Mol Biol* **144**, 431-453 (1980)

112. Boeckle, S.; von Gersdorff, K.; van der Piepen, S.; Culmsee, C.; Wagner, E.; Ogris, M. Purification of polyethylenimine polyplexes highlights the role of free polycations in gene transfer. *The Journal of Gene Medicine* **6**, 1102-1111 (2004)
113. Verhoye, M.; van der Sanden, B.P.J.; Rijken, P.F.J.W.; Peters, H.P.W.; Van der Kogel, A.J.; Pee, G.; Vanhoutte, G.; Heerschap, A.; Van der Linden, A. Assessment of the neovascular permeability in glioma xenografts by dynamic T-1 MRI with Gadomer-17. *Magn Reson Med* **47**, 305-313 (2002)
114. Tofts, P.S.; Brix, G.; Buckley, D.L.; Evelhoch, J.L.; Henderson, E.; Knopp, M.V.; Larsson, H.B.W.; Lee, T.-Y.; Mayr, N.A.; Parker, G.J.M.; Port, R.E.; Taylor, J.; Weisskoff, R.M. Estimating Kinetic Parameters From Dynamic Contrast-Enhanced T1-Weighted MRI of a Diffusable Tracer: Standardized Quantities and Symbol. *J Magn Reson Imaging* **10**, 223-232 (1999)
115. Vestvik, I.K.; Egeland, T.A.M.; Gaustad, J.V.; Mathiesen, B.; Rofstad, E.K. Assessment of microvascular density, extracellular volume fraction, and radiobiological hypoxia in human melanoma xenografts by dynamic contrast-enhanced MRI. *J Magn Reson Imaging* **26**, 1033-1042 (2007)
116. Demsar, F.; Roberts, T.P.L.; Schwickert, H.C.; Shames, D.M.; vanDijke, C.F.; Mann, J.S.; Saeed, M.; Brasch, R.C. A MRI spatial mapping technique for microvascular permeability and tissue blood volume based on macromolecular contrast agent distribution. *Magn Reson Med* **37**, 236-242 (1997)
117. Ogan, M.D. Albumin labeled with Gd-DTPA: an intravascular contrast-enhancing agent for magnetic resonance blood pool imaging: preparation and characterization. *Invest Radiol* **23**, 961-961 (1988)
118. Schneider, G.; Seidel, R.; Uder, M.; Wagner, D.; Weinmann, H.J.; Kramann, B. In vivo microscopic evaluation of the microvascular behavior of FITC-labeled macromolecular MR contrast agents in the hamster skinfold chamber. *Invest Radiol* **35**, 564-570 (2000)
119. Patlak, C.S.; Blasberg, R.G.; Fenstermacher, J.D. Graphical evaluation of blood-to-brain transfer constants from multiple-time uptake data. *J Cereb Blood Flow Metab* **3**, 1-7 (1983)
120. Youngner, J.S.; Algire, G.H. The effect of vascular occlusion on transplanted tumors. *J Natl Cancer Inst* **10**, 565-579 (1949)
121. Murakami, Y.; Tabata, Y.; Ikada, Y. Tumor accumulation of poly(ethylene glycol) with different molecular weights after intravenous injection. *Drug Delivery* **4**, 23-31 (1997)
122. Lin, Y.; Salek, M.F.S.; Jenning, N.; Gmitro, A.F. *Proceeding of SPIE* **6849**, (2008)

123. Widengren, J.; Chmyrov, A.; Eggeling, C.; Lofdahl, P.A.; Seidel, C.A.M. Strategies to improve photostabilities in ultrasensitive fluorescence spectroscopy. *J Phys Chem A* **111**, 429-440 (2007)
124. Widengren, J.; Mets, U.; Rigler, R. Photodynamic properties of green fluorescent proteins investigated by fluorescence correlation spectroscopy. *Chem Phys* **250**, 171-186 (1999)
125. Kim, S.A.; Heinze, K.G.; Bacia, K.; Waxham, M.N.; Schwille, P. Two-photon cross-correlation analysis of intracellular reactions with variable stoichiometry. *Biophys J* **88**, 4319-4336 (2005)
126. Bacia, K.; Schwille, P. Practical guidelines for dual-color fluorescence cross-correlation spectroscopy. *Nature Protocols* **2**, 2842-2856 (2007)
127. Perry, H.A.; Saleh, A.F.A.; Aojula, H.; Pluen, A. YOYO as a dye to track penetration of LK15 DNA complexes in spheroids: Use and limits. *J Fluoresc* **18**, 155-161 (2008)
128. Breunig, M.; Lungwitz, U.; Liebl, R.; Fontanari, C.; Klar, J.; Kurtz, A.; Blunk, T.; Goepferich, A. Gene delivery with tow molecular weight linear polyethytenimines. *The Journal of Gene Medicine* **7**, 1287-1298 (2005)
129. Remy-Kristensen, A.; Clamme, J.P.; Vuilleumier, C.; Kuhry, J.G.; Mely, Y. Role of endocytosis in the transfection of L929 fibroblasts by polyethylenimine/DNA complexes. *BBA-Biomembranes* **1514**, 21-32 (2001)
130. Frullano, L.; Meade, T.J. Multimodal MRI contrast agents. *JBIC* **12**, 939-949 (2007)

Paper I

Journal of Biomedical Optics 13(5), 054040 (September/October 2008)

Macromolecular diffusion in the extracellular matrix measured by fluorescence correlation spectroscopy

Nina Kristine Reitan
Aphirak Juthajan*
Tore Lindmo
Catharina de Lange Davies
The Norwegian University of Science and Technology
Department of Physics
7491 Trondheim, Norway

Abstract. Diffusion of therapeutic macromolecules through the extracellular matrix of tumor tissue is a crucial step in drug delivery. We use fluorescence correlation spectroscopy (FCS) to measure diffusion of IgG (150 kDa) and dextrans (155 kDa and 2 MDa) in solution, 5% gelatin hydrogel, and multicellular spheroids. Gel and spheroids are used as model systems for the extracellular matrix. The diffusion depends on the complexity of the environment, as well as on the size and structural shape of the diffusing molecules. The results based on one-photon FCS are in good agreement with diffusion coefficients obtained with two-photon fluorescence recovery after photobleaching (FRAP) using the same microscope (Zeiss LSM510 META/Confocor2). However, FCS reveals anomalous or multicomponent diffusion in gel and spheroids, which are not resolvable with FRAP. This study demonstrates that one-photon FCS can be used to study the extracellular transport of macromolecules in tumor tissue, and that FCS provides additional information about diffusion properties compared to FRAP.
 [DOI: 10.1117/1.2982530]

Keywords: fluorescence spectroscopy; correlation; tissues; confocal optics; diffusion; biology.

Paper 08046R received Feb. 5, 2008; revised manuscript received Jun. 9, 2008; accepted for publication Jun. 15, 2008; published online Oct. 14, 2008.

1 Introduction

The study of molecular dynamics in tissue provides valuable information about processes in the living organism. Insight into molecular binding, interactions, transport, and distribution, as well as the development of noninvasive techniques that provide such information, are crucial. In cancer research, it is important to acquire knowledge about delivery and pharmacokinetics of macromolecular anticancer agents (e.g., antibodies, liposomes, and DNA vectors), which are of great interest in therapy due to their specificity for tumor tissue. However, these large molecules have to overcome severe physiological barriers on their way from the blood vessels, through the extracellular matrix (ECM) and into the cancer cells, and only a minor fraction of the injected therapeutic macromolecules accumulates in tumor tissue.[1,2] Due to the high interstitial fluid pressure in tumors,[1,3] diffusion is the major interstitial transport mechanism. The ECM consists of a protein network embedded in a hydrophilic gel of glycosaminoglycans and proteoglycans, and this complex structure slows down diffusion of the therapeutic agents.[4] It is therefore of clinical importance to study diffusion and factors that influence transport behavior in the ECM.

Fluorescence correlation spectroscopy (FCS)[5,6] is a technique for measuring molecular dynamics and interactions, and the number of studies in living cells and tissue is increasing.[7–11] The principle of FCS is to detect intensity fluctuations from fluorescent molecules in a small detection volume defined by a focused laser beam. The temporal correlation of the intensity fluctuations yields valuable information about molecular properties like translational and rotational diffusion, interactions, concentration, and conformation changes. A low concentration of fluorescent molecules is essential to obtain proper correlation amplitudes, and this is an advantage when studying biological tissue.

FCS is a highly sensitive technique and not straightforward in complex systems like cellular environments. Heterogeneity, scattering, tissue absorption, low detection efficiency, photodamage, autofluorescence, and a distorted detection volume are all possible sources of error.[8,12] This degradation of information can partly be compensated for by increasing the laser power. This may, however, induce unwanted effects like autofluorescence, photobleaching, and optical saturation.[13,14]

Fluorescence recovery after photobleaching (FRAP) is an alternative technique for studying diffusion.[15] The basic principle is to photobleach fluorescent molecules in a chosen region of interest, and subsequently measure the rate of fluorescence recovery. As opposed to FCS, a high concentration of fluorophores is necessary to detect the influx of unbleached molecules during recovery. FRAP has a lower time resolution than FCS, because recovery may occur during the bleaching period in cases of fast diffusion. FRAP is therefore better suited for measuring slow diffusion on a time scale of milliseconds to seconds, whereas FCS operates best on a time scale of microseconds to milliseconds (the diffusion time window in the Confocor2 covers the range 0.2 μs to 1 s).[12] The

*Current affiliation: Carl Zeiss AS, 1086 Oslo, Norway.
Address all correspondence to: Nina Reitan, Dept. of Physics, Norwegian University of Science and Technology, Høgskoleringen 5, 7491 Trondheim, Norway; Tel: +47 73598709; Fax: +47 73597710; E-mail: nina.reitan@ntnu.no

1083-3668/2008/13(5)/054040/9/$25.00 © 2008 SPIE

highest diffusion coefficient that can be measured with two-photon FRAP is limited by the characteristic diffusion time and the bleaching time. According to Meyvis et al.,[16] the bleaching time should be less than $1/15$ of the characteristic diffusion time, but a factor of $1/2$ is also shown to be sufficient.[17]

Although FCS is a frequently used method for intracellular studies,[7–9,11,18] only a few FCS studies of extracellular diffusion in tissue have been published.[10] To our knowledge, there are no published results on extracellular diffusion in multicellular spheroids using FCS. In cellular environments, two-photon excitation has the advantage of increased depth penetration, reduced photobleaching, and a more well-defined detection volume.[8,19] However, the feasibility of one-photon FCS in living cells and tissue has been demonstrated.[8,20] The purpose of the present work was thus to explore the capabilities and limitations of a one-photon FCS system (ConfoCor2, Carl Zeiss Jena GmbH, Germany) to measure diffusion of macromolecules in tissue. Diffusion of IgG and dextran molecules was measured extracellularly in multicellular spheroids, as well as in gelatin hydrogel and solution, and compared to previously obtained results with FRAP.[17] Gel and spheroids were used as model systems for the ECM. Due to the structural obstacles in the ECM and interactions between the ECM constituents and macromolecules, a single, free diffusion coefficient may not be sufficient for characterizing diffusion. In the present work, three different theoretical fitting models were therefore applied and compared.

2 Materials and Methods

2.1 *Fluorescence Correlation Spectroscopy*

FCS is based on recording of intensity fluctuations from fluorescent molecules in the detection volume. Data processing yields a correlation function that compares the signal at time t with the signal at a short time τ later. The normalized autocorrelation function is given by[12]

$$G(\tau) = 1 + \frac{\langle \partial F(t) \cdot \partial F(t+\tau) \rangle}{\langle F(t) \rangle^2} = \frac{\langle F(t) \cdot F(t+\tau) \rangle}{\langle F(t) \rangle^2}, \quad (1)$$

where $F(t)$ is the measured fluorescence signal intensity at time t, and $\partial F(t)$ is the deviation from the mean signal intensity $\langle F(t) \rangle$.

To retrieve relevant information, the correlation function is represented by a proper mathematical model. A general fitting model for multiple diffusive species undergoing free translational diffusion in a 3-D Gaussian detection volume, including a triplet fraction, can be described by[12]

$$G(\tau) = 1 + \frac{1}{\langle N \rangle} \cdot \frac{1 - T + T \exp\left(-\frac{\tau}{\tau_T}\right)}{1 - T} \cdot \left\{ \sum_{i=1}^{m} \frac{\Phi_i}{\left[1 + \left(\frac{\tau}{\tau_{D_i}}\right)\right]\left[1 + \frac{1}{S^2}\left(\frac{\tau}{\tau_{D_i}}\right)\right]^{1/2}} \right\}, \quad (2)$$

where $\langle N \rangle$ is the mean number of particles in the detection volume, T and τ_T are the triplet fraction and triplet lifetime, respectively (both assumed equal for all components), Φ_i is the fractional intensity of the i'th species, m is the total number of species in the sample, and τ_{D_i} is the translational diffusion time of the i'th species through the detection volume.

The structure parameter,

$$S = \omega_z / \omega_{xy}, \quad (3)$$

denotes the ratio of the axial to the radial waist of the Gaussian detection volume, defined as the distances at which the intensity drops to $1/e^2$ of the maximum intensity.[12]

The diffusion coefficient D is calculated by

$$D = \frac{\omega_{xy}^2}{4\tau_D}. \quad (4)$$

For anomalous diffusion, D is the apparent diffusion coefficient and depends on the time scale, or equivalently the length scale, of the experiment.[21] The autocorrelation function for anomalous diffusion can be described by[12]

$$G(\tau) = 1 + \frac{1}{\langle N \rangle} \cdot \frac{1 - T + T \exp\left(-\frac{\tau}{\tau_T}\right)}{1 - T} \cdot \frac{1}{\left[1 + \left(\frac{\tau}{\tau_D}\right)^{\alpha}\right]\left[1 + \frac{1}{S^2}\left(\frac{\tau}{\tau_D}\right)^{\alpha}\right]^{1/2}}, \quad (5)$$

where α is the anomaly coefficient. The value of α indicates the degree of anomaly, and equals 1 for free, Brownian diffusion. Obstructed diffusion is indicated by $\alpha < 1$, and is called anomalous subdiffusion.[7,21,22]

2.2 *Materials and Sample Preparation*

Tetramethylrhodamine (TMR)-dextran, MW 155 kDa (Sigma-Aldrich, Saint Louis, Missouri) and 2 MDa (Molecular Probes, Eugene, Oregon), and 150-kDa Alexa Fluor 546-IgG (Molecular Probes, Eugene, Oregon) were used as fluorescent tracers. TMR and Alexa dyes are highly suitable for FCS due to high quantum yields, photostability, and aqueous solubility.

For maximum detection efficiency, concentrations of the tracers were chosen individually for the different model systems, using a lower limit of photon count rate equal to ten times the background signal[8] of an unstained sample. Due to difficulties dissolving the 2-MDa TMR-dextran molecule, the solution was successively vortexed and heated to 37 °C before filtering through a 0.45-μm membrane filter (Millex-HV, PVDF, Millipore, Billerica, Massachusetts) to eliminate large aggregates. For measurements of free diffusion in solution, the tracers were diluted in phosphate buffered saline (PBS) to concentrations on the order of 10^{-8} M.

Bovine gelatin powder (Kebo, Oslo, Norway) was weighed and dissolved in PBS to produce a hydrogel concentration of 5% (w/v). Tracers were added to final concentrations on the order of 10^{-8} M, and the mixture was given a quick stir before incubation at 45 °C for at least 20 min.

Multicellular spheroids were made from the human osteosarcoma cell line (OHS).[23] Tumor cell populations of 2×10^6 were seeded in 75-cm^2 cell culture flasks (Corning

Incorporated, Corning, New York) precoated with 9 ml of 1% soft agar, and containing 25-ml growth medium (RPMI-1640) supplemented with 10% fetal bovine serum, 100-units/ml penicillin/streptomycin, and 1-mM L-glutamine (all from Sigma-Aldrich, Saint Louis, Missouri). The spheroids were grown at 37 °C and 5% CO_2. Half the growth medium was changed after 3 days, and the spheroids were allowed to grow for 2 more days to reach a convenient size of 150 to 250 μm diameter.[24]

Spheroids were transferred to tubes and tracers were added to final concentrations of 10^{-7} to 10^{-6} M for 155-kDa dextran and 10^{-8} to 10^{-7} M for IgG and 2-MDa dextran. Several concentrations were prepared before each experiment, and the concentration that gave the best signal-to-noise ratio was chosen. FCS measurements were performed after incubation of the spheroids on a roller at 37 °C. The incubation time was 5 to 7 h for the smallest tracers. To ensure penetration into the spheroids, the 2-MDa dextran was allowed 10 to 12 h of incubation.

2.3 *Experimental Setup and Optimization of Parameters*

One-photon FCS measurements were performed using the LSM510/ConfoCor2 (Carl Zeiss Jena GmbH, Germany) with a C-Apochromat 40×/1.2-W corr objective. All tracers were excited by a 543-nm laser, and fluorescence was detected through a BP 560 to 615 filter and a pinhole diameter of 80 μm (1 Airy unit).

The dimension of the detection volume for the 543 HeNe laser line was estimated using rhodamine 6 G (Sigma-Aldrich, Saint Louis, Missouri) with a known diffusion coefficient of $2.8 \cdot 10^{-6}$ cm^2/s. The radial waist was calculated to 0.19 μm using Eq. (4).

Laser powers were kept low (0.9 to 2.3 μW incident on the sample) to avoid artifacts like photobleaching and optical saturation. Photobleaching was indicated by falling baselines in the intensity fluctuation data. Saturation was investigated for all tracers in solution, and was detected as a deviation from linearity between the photon count rate per molecule and laser power. Measured characteristic diffusion times remained constant in the chosen laser power range (data not shown).

To minimize the probability of having to discard data due to tracer aggregates passing through the detection volume, short measurement times were used (2 to 5 s). Statistics were improved by calculating the diffusion coefficients from the average correlation function of several (5 to 30) repetitive runs.[25]

The spheroids were imaged by confocal laser scanning microscopy (CLSM) to define the position of the FCS measurements in the ECM. Cells were visualized by detecting reflection of the argon 488 laser through a BP 480 to 520 filter [Fig. 1(a)], and the labeled macromolecules, which were located in the ECM, were imaged using a HeNe 543 laser and a LP 560 filter [Fig. 1(b)]. The resulting images were sufficient for localizing the extracellular space. The pixel size of the images was 0.11 (zoom 4) to 0.45 μm (zoom 1), i.e., the same order as the radial dimension of the detection volume. FCS measurements were typically performed in extracellular areas with a distance of 4 to 8 μm between cells [Fig. 1(d)]. The extracellular composition has previously been characterized.[26]

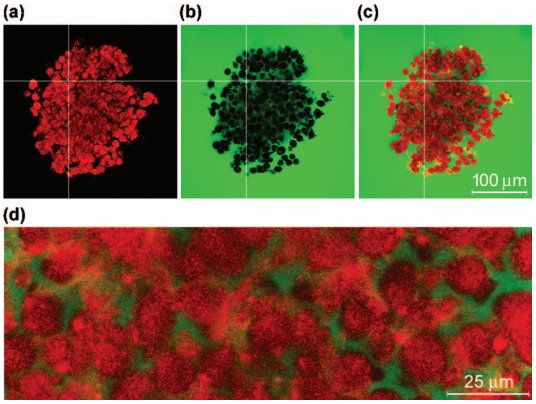

Fig. 1 CLSM image of an OHS multicellular spheroid incubated with Alexa Fluor 546 IgG. (a) Reflection of Ar 488 laser (red), (b) emission (BP 560 to 615 nm) of Alexa Fluor 546 (green), and (c) superposition of both images. The crosshair indicates the localization of the focal volume. (d) An enlarged section of the spheroid indicates the dimensions of the extracellular space.

The measurements were taken at a depth in the spheroids of 20 to 30 μm. FCS could not be performed farther into the spheroids due to scattering and absorption of light, resulting in a low signal-to-noise ratio. Images were compared before and after FCS measurements to exclude measurements influenced by movement artifacts.

2.4 *Data Analysis*

For the 2-MDa TMR-dextran, large peaks in the intensity time traces due to aggregates were carefully deleted from the raw data files. For all tracers, measurements were discarded if the fluctuation data showed a successively falling baseline, or if the normalized autocorrelation curve was distorted in any way. For data analysis, an anomalous fitting model and a two-component free diffusion model were applied whenever the one-component free diffusion model gave an unsatisfactory fit. The available fitting models in the LSM510/ConfoCor2 software are based on Eq. (2) and were used for one- and two-component fittings. The anomalous model based on Eq. (5) was applied using MATLAB (Mathworks Incorporated, Natick, Massachusetts) (gfit; open-source software for global analysis of experimental data, see http://gfit.sourceforge.net/).

A two-sample, two-tailed student's T-test (Minitab, Minitab Incorporated, State College, Pennsylvania) assuming nonequal variances was used to perform statistical comparison of the Gaussian-distributed diffusion coefficients obtained with FCS and FRAP. The Mann-Whitney test was applied when the normality assumption was violated and the sample size was less than 30. A significance criterion of $p \leqslant 0.05$ was used. The goodness of fit was quantified by R^2 (the correlation index).[27] To statistically compare the fitting models, the difference between R^2 for the two-component and the anomalous model ($R^2_{\text{two-component}} - R^2_{\text{anomalous}}$) was calculated for each dataset and grouped according to tracers and model systems. The probability of this difference being equal to zero was tested with a 95% confidence interval.

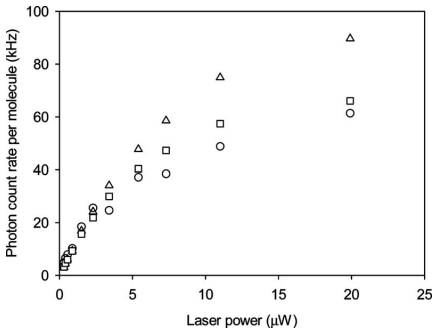

Fig. 2 Investigation of optical saturation for Alexa Fluor 546-IgG (□), 155-kDa TMR-dextran (△), and 2-MDa TMR-dextran (○) in solution. The plot shows the photon count rate per molecule as a function of the laser power incident on the sample.

3 Results

3.1 *Optimization and Calibration of Experimental Setup*

Optimal illumination of the samples was achieved by keeping the laser power at a low level to minimize photobleaching and optical saturation. Photobleaching was occasionally observed as a falling baseline in the fluorescence intensity time traces (data not shown). For all tracers in solution, saturation effects were observed as a deviation from the linear dependence between the photon count rate per molecule and laser power, and occurred above laser powers of 3.4 μW incident on the sample (Fig. 2). Based on this, the maximum laser power used in the FSC experiments was 2.3 μW incident on the sample.

To confirm that our instrumental setup was well calibrated, the diffusion of all tracers was measured in aqueous solution as a first step. As expected, the one-component free diffusion model was found to be appropriate (Table 1). Fitting the anomalous model to measurements of free diffusion in solution yielded average anomaly coefficients for the three tracers in the range of $0.91 < \alpha < 0.93$. Fitting a two-component model to the same experimental data did not give interpretable results, as one of the components indicated unlikely fast diffusion.

3.2 *Diffusion Measurements*

Representative intensity time traces for IgG and dextrans in gel and spheroids are shown in Fig. 3. Aggregates are visible as peaks in the fluctuation data for the 2-MDa dextran. The higher average photon count rate for measurements in sphe-

Table 1 Mean values of experimental diffusion coefficients (10^{-8} cm^2/s) and standard deviations obtained with FCS for IgG and dextrans (155 kDa and 2 MDa) in solution, 5% gelatin hydrogel, and OHS multicellular spheroids. For measurements in solution, the one-component free diffusion model was used. For measurements in gel and spheroids, diffusion coefficients are estimated by the two-component free diffusion model and the anomalous diffusion model. The anomaly coefficients α are presented, together with the anomalous diffusion coefficients.

System	One-component free or anomalous diffusion		Two-component free diffusion	
	D	α	*D*1	*D*2
150-kDa IgG				
Solution	31.99±0.88	-	-	-
Gel	9.65±3.01	0.76±0.04	14.42±3.93	1.58±1.08
Spheroids	20.95±4.83	0.81±0.05	22.51±4.49	1.96±1.41
155-kDa dextran				
Solution	18.13±1.64	-	-	-
Gel	5.81±1.13	0.82±0.08	16.26±8.86	2.97±1.52
Spheroids	12.68±2.79	0.86±0.09	17.28±3.65	2.77±2.07
2-MDa dextran				
Solution	7.33±0.95	-	-	-
Gel	2.97±0.42	0.85±0.06	12.86±6.06	1.35±0.56
Spheroids	1.23±0.32	0.81±0.08	4.81±2.62	0.54±0.31

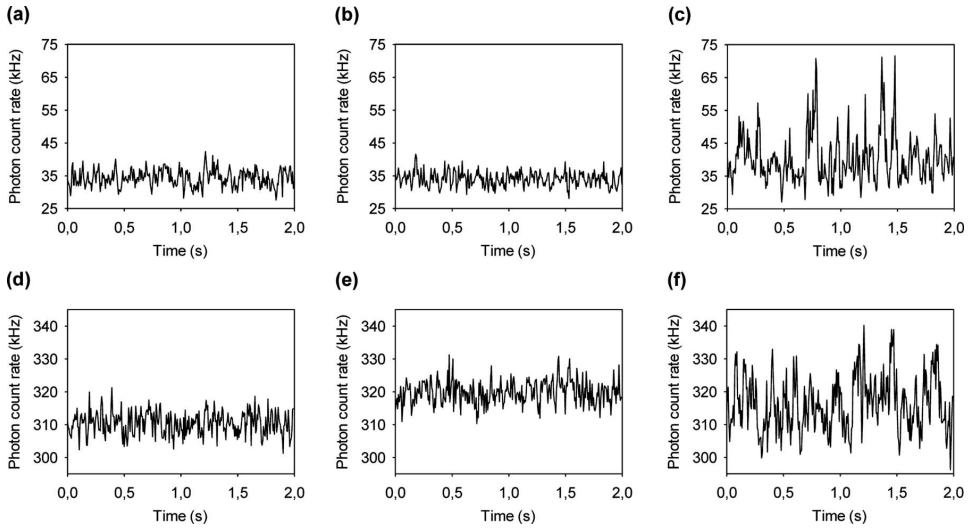

Fig. 3 Intensity fluctuations during the measurement for (a) and (d) Alexa Fluor 546–IgG, (b) and (e) 155-kDa TMR-dextran, and (c) and (f) 2-MDa TMR-dextran in (a), (b), and (c) 5% gelatin hydrogel, and (d), (e), and (f) OHS multicellular spheroids.

roids reflects the higher concentration of tracer needed to overcome the cellular autofluorescence. Typically, the one-component free diffusion model failed when fitted to the autocorrelation curves obtained from measurements in gel and spheroids. An anomalous diffusion model and a free diffusion model with two species were therefore applied (Table 1), as shown for IgG in Fig. 4. However, the quality of fit by the two latter models could not be distinguished based on R^2.

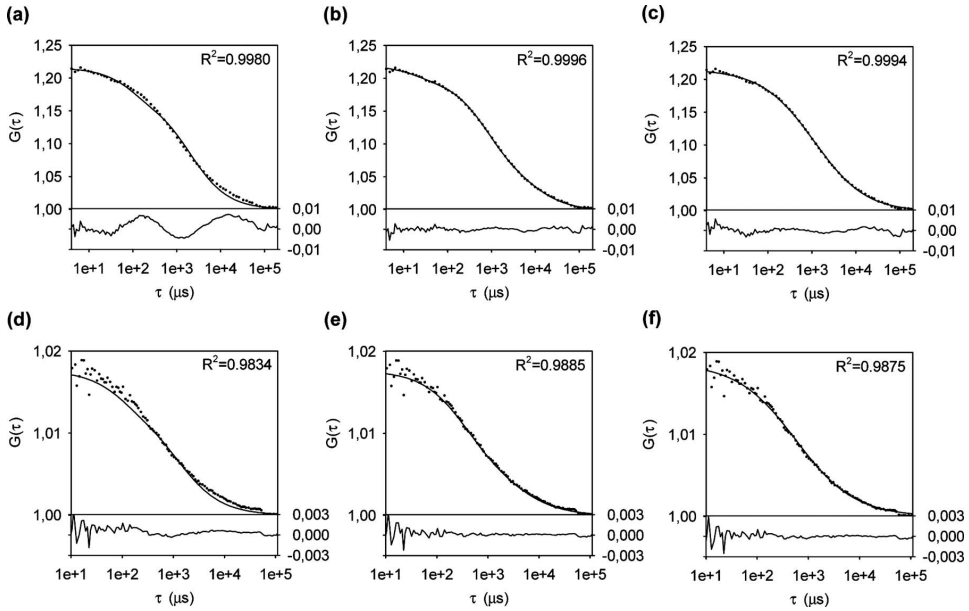

Fig. 4 Autocorrelation function (…….) and curve fitting (—) by (a) and (d) one-component, (b) and (e) anomalous, and (c) and (f) two-component model for (a), (b), and (c) IgG in 5% gelatin hydrogel and (d), (e), and (f) OHS multicellular spheroids. The goodness of fit is indicated by R^2, and residuals are shown in the lower part of each panel.

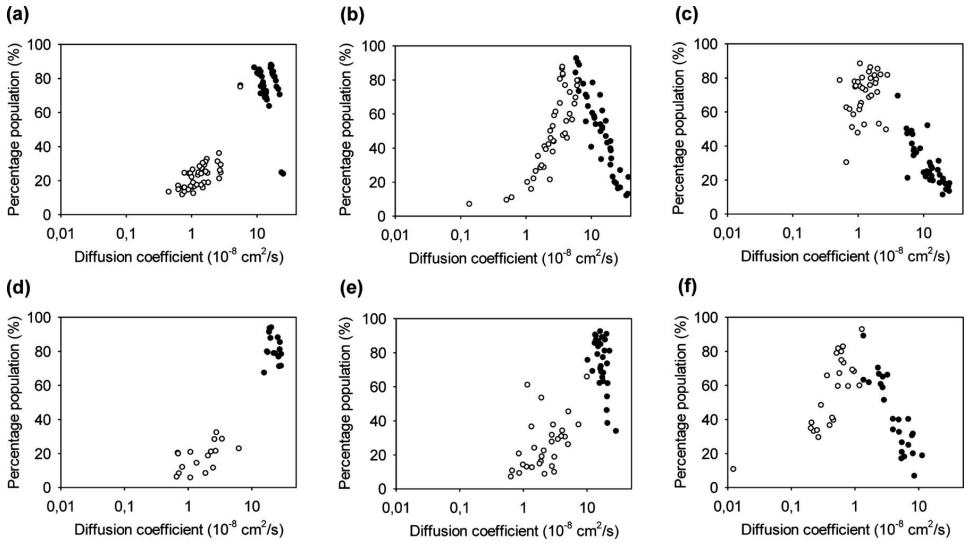

Fig. 5 Percentage populations of the fast (●) and slow (○) diffusion components obtained by fitting the two-component free diffusion model for (a) and (d) IgG, (b) and (e) 155-kDa dextran, and (c) and (f) 2-MDa dextran in (a), (b), and (c) 5% gelatin hydrogel and (d), (e), and (f) OHS multicellular spheroids.

Using the anomalous model, all three tracers showed subdiffusive properties in both gel and spheroids. The two-component model gave significantly different diffusion coefficients for the two components. The ratios of the fast to slow diffusing components were in the range of 5 to 11. The average populations (Fig. 5) of the two diffusing components were especially well separated for IgG. For IgG in gel, a further separation in two groups can be seen within each component [Fig. 5(a)]. This reflects the variability between gels produced on two different days. In gel, the ratios of the diffusion coefficients of the fast components relative to those in solution were 0.45, 0.90, and 1.75, and the percentage populations of the fast components were (75 ± 13), (50 ± 23), and (30 ± 13)% for IgG, 155-kDa dextran, and 2-MDa dextran, respectively. In spheroids, the ratios of the diffusion coefficients of the fast components relative to those in solution were 0.71, 0.95, and 0.66, and the percentage populations of the fast components were (82 ± 8.1), (74 ± 16), and (42 ± 22)% for IgG, 155-kDa dextran, and 2-MDa dextran, respectively.

Diffusion coefficients obtained from the one-component free diffusion model for solution and the anomalous model for gel and spheroids were compared (Fig. 6). The diffusion coefficients in solution, gel, and spheroids are significantly different for all tracers. The diffusion coefficients for 2-MDa dextran are significantly lower than for the smaller molecules in all model systems. IgG experienced a significantly faster diffusion than 155-kDa dextran in all model systems. The ratios of the diffusion coefficients in gel to those in solution are approximately the same (0.30 to 0.41) for all tracers. Diffusion measured extracellularly in spheroids is approximately twice as fast as in gels for both IgG and 155-kD dextran. The 2-MDa molecule, on the other hand, experiences a markedly retarded diffusion in spheroids. The ratios of the diffusion coefficients in spheroids to those in solution are approximately 0.66 and 0.70 for IgG and 155-kDa dextran, respectively, and 0.16 for 2-MDa dextran.

3.3 *Comparison of Diffusion Coefficients Measured with Fluorescence Correlation Spectroscopy and Fluorescence Recovery after Photobleaching*

Anomalous diffusion coefficients determined by FCS was compared to free diffusion coefficients obtained with FRAP[17] for tracers in solution, 5% gelatin hydrogel, and OHS multicellular spheroids (Fig. 7). The FRAP measurements, which were previously performed in our laboratory, were best repre-

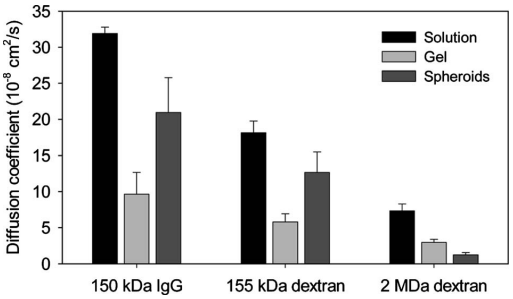

Fig. 6 Mean diffusion coefficients with standard deviations for IgG, 155-kDa dextran, and 2-MDa dextran in solution (black), 5% gelatin hydrogel (light gray), and OHS multicellular spheroids (dark gray). Diffusion coefficients for measurements in solution are based on the one-component free diffusion model, whereas the anomalous diffusion model was used to estimate diffusion coefficients in gel and spheroids. Mean values represent 18 to 45 measurements.

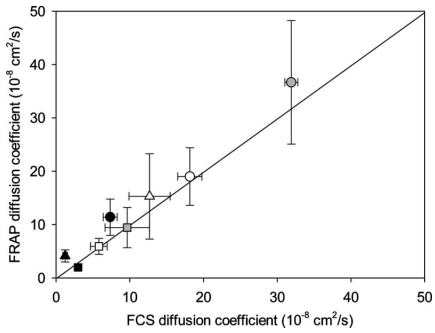

Fig. 7 Mean diffusion coefficients calculated from FCS and FRAP measurements of IgG (gray), 155-kDa dextran (white), and 2-MDa dextran (black) in solution (circle), 5% gelatin hydrogel (square), and OHS multicellular spheroids (triangle). Standard deviations are indicated by error bars. The one-component free diffusion model was used for FRAP in all model systems and for FCS in solution, whereas the anomalous diffusion model was applied for FCS in gel and spheroids. Mean FCS values represent 18 to 45 measurements. FRAP measurement of FITC-IgG in spheroids was not obtained due to internalization of the labeled molecules into the cells.

sented by the one-component free diffusion model. The differences between the diffusion coefficients estimated by the two techniques are in the range of one standard deviation.

4 Discussion

One-photon FCS measurements of macromolecular diffusion in solution, 5% gelatin hydrogel, and extracellularly in OHS multicellular spheroids were successfully achieved and compared to previously reported two-photon FRAP data.[17] A novel aspect is to use FCS to measure extracellular diffusion in multicellular spheroids, which is a well-established model for avascular tumor tissue.[4,24,28,29] Whereas FRAP has been used for this purpose,[4,30] no FCS studies on extracellular diffusion in multicellular spheroids have, to our knowledge, previously been published. In the present study, the main goal was to investigate whether FCS measurements give comparable results to FRAP data obtained on the same microscope, and whether results obtained with FCS indicate anomalous or multiphase diffusion, and thereby provide additional information to FRAP.

4.1 *Diffusion of Macromolecules in 5% Gelatin Hydrogel Multicellular Spheroids*

The diffusion coefficient for dextrans decreased with increasing molecular size. IgG experienced a faster diffusion than the dextran of approximately the same size. This has been previously reported,[31] and is due to the configurational difference between the globular IgG and the linear, flexible dextran.

The diffusion of IgG and dextrans in gel and spheroids was slower than in solution, and deviated from the one-component free diffusion model. This demonstrates that molecular mobility is subject to obstruction by the polymer network. However, tracer aggregates or a distorted Gaussian focus profile may also cause the one-component free diffusion model to fail, giving an erroneous impression of anomalous or multiphase diffusion.[19] To avoid distortion of the focus profile, the laser power was kept low.

Fitting of the anomalous model to autocorrelation functions for all three tracers in gel and spheroids yielded anomaly coefficients close to, but significantly different from, the anomaly coefficients measured in solution. This result is supported by a diffusion study conducted by Lead, Starchev, and Wilkinson,[32] which showed that increasing a gel concentration from 0 to 3% resulted in only a slight increase of anomaly. Anomalous diffusion in heterogeneous systems has been reported in several FCS studies.[7,9,11,21,32–34] Various underlying causes for anomalous diffusion have been suggested, such as molecular binding of the diffusing particles,[35] adsorption to chains in the structural meshwork,[34] molecular crowding,[11] and infrequent and large jumps that particles make between distinct pores in the network in which they are constrained.[36]

The two-component diffusion model was successfully fitted to all measurements in gel and spheroids. In all cases, the diffusion coefficients of the two components were significantly different. The fastest diffusion components were found to be of the same order as the free diffusion coefficient measured in solution, hence indicating an aqueous phase. Only for the 2-MDa dextran in gel was the fast component significantly higher than the free diffusion coefficient in solution. The slow components were five to eleven times slower than the fast components.

It has been suggested that the interstitial space consists of two phases; a viscous gel compartment and a free-fluid space, which offers less resistance to interstitial transport,[37,38] thus supporting the relevance of the two-component model. FCS has also revealed a two-phase diffusion process in tumors.[10] However, in complex and heterogeneous environments like the interstitium, molecules may aggregate, bind to structures of various sizes, or be trapped in compartments. Diffusion may thus be more diverse than what can be represented by the two-component model.

To determine whether diffusion is anomalous or if there are, in fact, two components diffusing with different speed, would give valuable information about the structural geometry of the ECM and interactions between the ECM and the diffusing particles. However, based on visual inspection of the curve fits and the corresponding residuals, together with a statistical analysis of R^2, it was not possible to conclude which model gives a true representation of the diffusion process. This is in accordance with previous findings of molecular dynamics in complex systems.[7,9,33] On the other hand, several factors suggest that the two-component model is less reliable, the lack of a visible two-component shape of the autocorrelation curve, the unlikely high diffusion coefficient of the fast component for 2-MDa dextran in gel, and the large standard deviations for the mean diffusion coefficients calculated from the two-component model (Table 1). The fact that the anomalous model fits the data equally well with a lower number of variables further suggests that this model is more robust.

4.2 *Relevance of Tissue Models*

Gelatin hydrogel mimics the structural collagen network in the ECM, and the multicellular spheroid represents a 3-D *in-*

vitro model of an avascular tumor.[28] A gelatin gel of 5% has a density of collagen fibers comparable to the collagen content in the ECM of tissue, which is reported to be 0.2 to 2%.[39,40] The collagen concentration in OHS multicellular spheroids, however, has been measured to 0.05% (unpublished data). Also other multicellular spheroids have been shown to have ten times less collagen content compared to the corresponding xenografts growing *in vivo*.[4] In the present study, diffusion is clearly more obstructed in gel than in spheroids for IgG and 155-kDa dextran. However, in contrast to the two smaller molecules, the 2-MDa dextran experiences a slower diffusion in the ECM than in gel. This indicates that up to a certain size, the particles are mainly retarded because of their molecular shape and increased viscosity of the solvent. For the 2-MDa molecule, however, the size of the particle relative to the mesh size of the geometrical network provides an additional retarding factor. The ECM is therefore a more severe barrier for larger molecules.

4.3 *Fluorescence Correlation Spectroscopy Compared to Fluorescence Recovery after Photobleaching*

One-photon FCS data were compared to results previously obtained with two-photon FRAP.[17] The FCS measurements revealed both anomalous and two-component diffusion, which were not detectable in the FRAP study. This demonstrates that FCS is a more sensitive technique than FRAP, and provides information with a higher time resolution. The anomaly coefficients for the FCS data indicate little deviation from free diffusion, and we therefore assume that the anomalous diffusion coefficients can be compared to the free diffusion coefficients obtained with FRAP. Except for the 2-MDa molecule, diffusion coefficients from FCS measurements equal the FRAP diffusion coefficients within the range of one standard deviation. This demonstrates that although the two methods differ in principle and in practical applications, FCS and FRAP can be applied to the same system within a certain time scale of the molecular dynamics.

FCS and FRAP are both based on fluorescence detection, and are commonly used in diffusion studies.[4,10,11,18,33,39] There are, however, several fundamental differences between the two methods, making them suitable for different purposes. FRAP is based on equilibrium perturbation by photobleaching of a predefined area with a high laser intensity and subsequently detecting the influx of unbleached tracers. The photobleaching process may induce uncharacterized chemical and biological disturbances in the sample. In FCS, the system is in equilibrium throughout the FCS measurement, and photobleaching is avoided by using low laser intensities. This implies that the two techniques require fluorophores with different photostability. In addition, whereas one single particle is detectable in FCS, high concentrations are required to perform a FRAP experiment. FCS is thus less invasive than FRAP when studying living tissue, because substantially less chemical substance is injected and no perturbation of the system occurs. For measuring immobile fractions, FRAP is a better suited technique because FCS cannot detect immobile or very slowly moving particles. For small particles in solution, the diffusion is too rapid for FRAP detection, but ideal for FCS. Another advantage of FCS over FRAP is that it is a more versatile technique, giving information about translational and rotational diffusion, triplet fractions, interactions, and concentrations.

5 Conclusion

The present work demonstrates that one-photon FCS is suitable for measuring diffusion of macromolecules extracellularly in tissue. One-photon FCS and two-photon FRAP[17] measurements on the LSM510/ConfoCor2 gave comparable diffusion coefficients. In addition, FCS revealed a two-phase or an anomalous nature of the transport in gel and spheroids, which was not possible to detect with FRAP performed on the same microscope.

FCS is an important technique for studying the delivery of macromolecules in cancer therapy. The method may provide information about the interactions and transport barriers extracelluarly as well as intracellularly.[18] FCS and related techniques[41–44] are constantly being refined, and are valuable tools for investigating fundamental processes in molecular biology.

Acknowledgments

We gratefully acknowledge Mikhail Levin, UCHC, Farmington, Connecticut, for assistance on the *gfit* software; Kristin Sæterbø, Department of Physics, NTNU, for cultivating cells; and Henning Omre, Department of Mathematical Sciences, NTNU, for advice on statistical analysis. The work was supported by the Norwegian Cancer Society.

References

1. L. Eikenes, Ø. S. Bruland, C. Brekken, and C. de L. Davies, "Collagenase increases the transcapillary pressure gradient and improves the uptake and distribution of monoclonal antibodies in human osteosarcoma xenografts," *Cancer Res.* **64**(14), 4768–4773 (2004).
2. M. Ferrari, "Cancer nanotechnology: Opportunities and challenges," *Nat. Rev. Cancer* **5**(3), 161–171 (2005).
3. Y. Boucher, L. T. Baxter, and R. K. Jain, "Interstitial pressure-gradients in tissue-isolated and subcutaneous tumors-implications for therapy," *Cancer Res.* **50**(15), 4478–4484 (1990).
4. C. de L. Davies, D. A. Berk, A. Pluen, and R. K. Jain, "Comparison of IgG diffusion and extracellular matrix composition in rhabdomyosarcomas grown in mice versus *in vitro* as spheroids reveals the role of host stromal cells," *Br. J. Cancer* **86**(10), 1639–1644 (2002).
5. D. Magde, E. Elson, and W. W. Webb, "Thermodynamic fluctuations in a reacting system-measurement by fluorescence correlation spectroscopy," *Phys. Rev. Lett.* **29**(11), 705–708 (1972).
6. R. Rigler, Ü. Mets, J. Widengren, and P. Kask, "Fluorescence correlation spectroscopy with high count rate and low background: analysis of translational diffusion," *Eur. Biophys. J.* **22**(3), 169–175 (1993).
7. M. Wachsmuth, W. Waldeck, and J. Langowski, "Anomalous diffusion of fluorescent probes inside living cell nuclei investigated by spatially-resolved fluorescence correlation spectroscopy," *J. Mol. Biol.* **298**(4), 677–689 (2000).
8. P. Schwille, U. Haupts, S. Maiti, and W. W. Webb, "Molecular dynamics in living cells observed by fluorescence correlation spectroscopy with one- and two-photon excitation," *Biophys. J.* **77**(4), 2251–2265 (1999).
9. M. Weiss, H. Hashimoto, and T. Nilsson, "Anomalous protein diffusion in living cells as seen by fluorescence correlation spectroscopy," *Biophys. J.* **84**(6), 4043–4052 (2003).
10. G. Alexandrakis, E. B. Brown, R. T. Tong, T. D. McKee, R. B. Campbell, Y. Boucher, and R. K. Jain, "Two-photon fluorescence correlation microscopy reveals the two-phase nature of transport in tumors," *Nat. Med.* **10**(2), 203–207 (2004).
11. M. Weiss, M. Elsner, F. Kartberg, and T. Nilsson, "Anomalous subdiffusion is a measure for cytoplasmic crowding in living cells," *Biophys. J.* **87**(5), 3518–3524 (2004).

12. K. Weisshart, V. Jüngel, and S. J. Briddon, "The LSM 510 META-ConfoCor 2 system: an integrated imaging and spectroscopic platform for single-molecule detection," *Curr. Pharm. Biotechnol.* **5**(2), 135–154 (2004).
13. I. Gregor, D. Patra, and J. Enderlein, "Optical saturation in fluorescence correlation spectroscopy under continuous-wave and pulsed excitation," *ChemPhysChem* **6**(1), 164–170 (2005).
14. G. Nishimura and M. Kinjo, "Systematic error in fluorescence correlation measurements identified by a simple saturation model of fluorescence," *Anal. Chem.* **76**(7), 1963–1970 (2004).
15. D. Axelrod, D. E. Koppel, J. Schlessinger, E. Elson, and W. W. Webb, "Mobility measurement by analysis of fluorescence photobleaching recovery kinetics," *Biophys. J.* **16**(9), 1055–1069 (1976).
16. T. K. L. Meyvis, S. C. De Smedt, P. Van Oostveldt, and J. Demeester, "Fluorescence recovery after photobleaching: a versatile tool for mobility and interaction measurements in pharmaceutical research," *Pharm. Res.* **16**(8), 1153–1162 (1999).
17. E. A. Schnell, L. Eikenes, I. Tufto, A. Erikson, A. Juthajan, M. Lindgren, and C. de L. Davies, "Diffusion measured by fluorescence recovery after photobleaching based on multiphoton excitation laser scanning microscopy," submitted to *J. Biomed. Opt.* (2008).
18. J. P. Clamme, G. Krishnamoorthy, and Y. Mély, "Intracellular dynamics of the gene delivery vehicle polyethylenimine during transfection: investigation by two-photon fluorescence correlation spectroscopy," *Biochim. Biophys. Acta* **1617**(1–2), 52–61 (2003).
19. S. T. Hess and W. W. Webb, "Focal volume optics and experimental artifacts in confocal fluorescence correlation spectroscopy," *Biophys. J.* **83**(4), 2300–2317 (2002).
20. S. A. Tatarkova, A. K. Verma, D. A. Berk, and C. J. Lloyd, "Quantitative fluorescence microscopy of macromolecules in gel and biological tissue," *Phys. Med. Biol.* **50**(23), 5759–5768 (2005).
21. D. S. Banks and C. Fradin, "Anomalous diffusion of proteins due to molecular crowding," *Biophys. J.* **89**(5), 2960–2971 (2005).
22. A. Masuda, K. Ushida, and T. Okamoto, "New fluorescence correlation spectroscopy enabling direct observation of spatiotemporal dependence of diffusion constants as an evidence of anomalous transport in extracellular matrices," *Biophys. J.* **88**(5), 3584–3591 (2005).
23. Ø. Fodstad, A. Brøgger, Ø. Bruland, Ø. P. Solheim, J. M. Nesland, and A. Pihl, "Characteristics of a cell-line established from a patient with multiple osteosarcoma, appearing 13 years after treatment for bilateral retinoblastoma," *Int. J. Cancer* **38**(1), 33–40 (1986).
24. M. H. Hjelstuen, K. Rasch-Halvorsen, C. Brekken, Ø. Bruland, and C. de L. Davies, "Penetration and binding of monoclonal antibody in human osteosarcoma multicell spheroids: Comparison of confocal laser scanning microscopy and autoradiography," *Acta Oncol.* **35**(3), 273–279 (1996).
25. O. Krichevsky and G. Bonnet, "Fluorescence correlation spectroscopy: the technique and its applications," *Rep. Prog. Phys.* **65**(2), 251–297 (2002).
26. C. de L. Davies, H. Müller, I. Hagen, M. Gårseth, and M. H. Hjelstuen, "Comparison of extracellular matrix in human osteosarcomas and melanomas growing as xenografts, multicellular spheroids, and monolayer cultures," *Anticancer Res.* **17**(6D), 4317–4326 (1997).
27. A. M. Brown, "A step-by-step guide to non-linear regression analysis of experimental data using a Microsoft Excel spreadsheet," *Comput. Methods Programs Biomed.* **65**, 191–200 (2001).
28. R. M. Sutherland, "Cell and environment interactions in tumor microregions-the multicell spheroid model," *Science* **240**(4849), 177–184 (1988).
29. M. H. Hjelstuen, K. Rasch-Halvorsen, Ø. Bruland, and C. de L. Davies, "Uptake, penetration, and binding of monoclonal antibodies with increasing affinity in human osteosarcoma multicell spheroids," *Anticancer Res.* **18**(5A), 3153–3161 (1998).
30. H. Sauer, V. Pütz, K. Fischer, J. Hescheler, and M. Wartenberg, "Increased doxorubicin uptake and toxicity in multicellular tumour spheroids treated with DC electrical fields," *Br. J. Cancer* **80**(8), 1204–1213 (1999).
31. D. A. Berk, F. Yuan, M. Leunig, and R. K. Jain, "Fluorescence photobleaching with spatial Fourier-analysis: measurement of diffusion in light-scattering media," *Biophys. J.* **65**(6), 2428–2436 (1993).
32. J. R. Lead, K. Starchev, and K. J. Wilkinson, "Diffusion coefficients of humic substances in agarose gel and in water," *Environ. Sci. Technol.* **37**(3), 482–487 (2003).
33. P. Schwille, J. Korlach, and W. W. Webb, "Fluorescence correlation spectroscopy with single-molecule sensitivity on cell and model membranes," *Cytometry* **36**(3), 176–182 (1999).
34. G. C. Fadda, D. Lairez, B. Arrio, J. P. Carton, and V. Larreta-Garde, "Enzyme-catalyzed gel proteolysis: an anomalous diffusion-controlled mechanism," *Biophys. J.* **85**(5), 2808–2817 (2003).
35. M. J. Saxton, "Anomalous diffusion due to binding: a Monte Carlo study," *Biophys. J.* **70**(3), 1250–1262 (1996).
36. I. Y. Wong, M. L. Gardel, D. R. Reichman, E. R. Weeks, M. T. Valentine, A. R. Bausch, and D. A. Weitz, "Anomalous diffusion probes microstructure dynamics of entangled F-actin networks," *Phys. Rev. Lett.* **92**(17), 178101 (2004).
37. R. K. Jain, "Transport of molecules in the tumor interstitium: a review," *Cancer Res.* **47**(12), 3039–3051 (1987).
38. C. A. Wiederhielm, "Dynamics of capillary fluid exchange: A nonlinear computer simulation," *Microvasc. Res.* **18**, 48–82 (1979).
39. P. A. Netti, D. A. Berk, M. A. Swartz, A. J. Grodzinsky, and R. K. Jain, "Role of extracellular matrix assembly in interstitial transport in solid tumors," *Cancer Res.* **60**(9), 2497–2503 (2000).
40. C. de L. Davies, B. Ø. Engesæter, I. Haug, I. W. Ormberg, J. Halgunset, and C. Brekken, "Uptake of IgG in osteosarcoma correlates inversely with interstitial fluid pressure, but not with interstitial constituents," *Br. J. Cancer* **85**(12), 1968–1977 (2001).
41. N. O. Petersen, "Scanning fluorescence correlation spectroscopy. I. Theory and simulation of aggregation measurements," *Biophys. J.* **49**(4), 809–815 (1986).
42. J. Ries and P. Schwille, "Studying slow membrane dynamics with continuous wave scanning fluorescence correlation spectroscopy," *Biophys. J.* **91**(5), 1915–1924 (2006).
43. M. A. Digman, P. Sengupta, P. W. Wiseman, C. M. Brown, A. R. Horwitz, and E. Gratton, "Fluctuation correlation spectroscopy with a laser-scanning microscope: Exploiting the hidden time structure," *Biophys. J.* **88**(5), L33–L36 (2005).
44. R. P. Kulkarni, D. D. Wu, M. E. Davis, and S. E. Fraser, "Quantitating intracellular transport of polyplexes by spatio-temporal image correlation spectroscopy," *Proc. Natl. Acad. Sci. U.S.A.* **102**(21), 7523–7528 (2005).

Paper II

Is not included due to copyright

Paper III

Supporting information:

FCS multi-component free diffusion fitting model.

Assuming a 3D Gaussian detection volume, the general multi-component free diffusion fitting model is described by

$$G(\tau)=1+\frac{1}{\langle N\rangle}\cdot\frac{1-T+Te^{-\frac{\tau}{\tau_T}}}{1-T}\cdot\left[\sum_{i=1}^{m}\frac{\Phi_i}{\left(1+\frac{\tau}{\tau_{D_i}}\right)\sqrt{1+\left(\frac{\omega_{xy}}{\omega_z}\right)^2\cdot\frac{\tau}{\tau_{D_i}}}}\right]$$

where $\langle N\rangle$ is the mean number of particles in the detection volume, T and τ_T are the triplet fraction and triplet lifetime, respectively (both assumed equal for all components), Φ_i is the fractional intensity of the ith species, m is the total number of species in the sample, and τ_{D_i} is the characteristic diffusion time of the ith species through the detection volume. For m=1, Eq. (1) is reduced to the one-component free diffusion model. ω_{xy} and ω_z are the axial and the radial waist of the Gaussian detection volume, respectively, defined as the distances at which the intensity drops to $1/e^2$ of the maximum intensity.

Structure-function relationship in chitosan-mediated gene delivery: controlling polyplex disassembly through chitosan design

Sabina P. Strand[1*], *Sylvie Lelu*[2], *Nina K. Reitan*[2], *Per Artursson*[3], *Catharina de Lange Davies*[2], *Kjell M. Vårum*[1]

[1]Department of Biotechnology, Norwegian Biopolymer Laboratory (NOBIPOL), Norwegian University of Science and Technology (NTNU), 7491 Trondheim, Norway

[2]Department of Physics, Norwegian University of Science and Technology, 7491 Trondheim, Norway

[3]Department of Pharmacy, Uppsala University, Box 580, 751 23 Uppsala, Sweden

Keywords: chitosan, gene delivery, transfection, DNA nanoparticles, chain length

---

Manuscript in preparation.

[*] Corresponding author: sabina.strand@biotech.ntnu.no

Abstract

Despite growing interest in chitosans as gene delivery vehicles, the understanding of the structure-function relationship is still incomplete. Here, we have systematically varied the degree of interaction between the chitosan and its pDNA cargo by controlling i) chain length of the chitosan and ii) degree of hindrance, and examined the influence of these parameters on gene transfer. For this purpose, we have prepared series of six low molecular weight chitosans with constant charge density and a degree of polymerization (DP_n) in the range of 21 – 88 (Mw 4.7 – 33 kDa). Using these chitosans, we have studied the relationship between the chain length and formulation properties, cellular uptake of polyplexes, and gene transfer efficacy. At a given amino-phosphate (A/P) ratio, the various chitosans complexed pDNA into nanoparticles of comparable size and surface charge which showed similar cellular uptake but highly variable transfection efficacy. The maximum gene expression was achieved with DP_n31 – 42 and an increase in chain length and A/P ratios reduced and delayed luciferase expression. The gene transfer pattern correlated with the heparin induced unpacking of polyplexes. Substituting the chitosan by uncharged oligosaccharides weakened the interaction with pDNA and reduced or enhanced transfection efficacy, depending on the DP_n and A/P. The more stable polyplexes, the higher increase in transfection efficacy was achieved after substitution. Furthermore, the magnitude of gene expression was also controlled by the size of the substituent. Confocal laser scanning microscopy (CLSM) and fluorescence correlation spectroscopy (FCS) investigation of intracellular trafficking and dissociation of the polyplexes did not provide any direct evidence of differences in polyplex unpacking but demonstrated that the polyplexes were internalized as large aggregated structures and were transported to the nucleus. FCS revealed that chitosan molecules were diffusing in the cytoplasm and nucleus. Altogether, these findings suggest that the chitosan-mediated gene delivery may be controlled by modulation of the interaction strength between the chitosan vector and its plasmid cargo which determines the timing and extent of polyplex disassembly.

Introduction

Chitosans, linear copolymers of β-1-4 linked N-acetyl-D-glucosamine (GlcNAc) and D-glucosamine (GlcN), are naturally derived cationic polysaccharides that are highly attractive as drug and gene delivery candidates [1-3]. The interest in chitosan is related to its availability, excellent safety profile, biodegradability, ease of modification as well as unique biological properties. Due to its polycationic nature, chitosans spontaneously self-assembly with nucleic acids to form nanosized complexes that may be employed for gene delivery. Since chitosan is a weak polybase with the pK_a of 6.6 [4, 5], the charge density of chitosan depends on pH and implies that chitosan may be regarded as a pH-responsive polymer. High charge density of chitosan below pK_a may be beneficial for polyplex preparation and escape from endocytotic vesicles, whereas low charge density at pH 7.4 contributes to low cytotoxicity and may facilitate intracellular pDNA release. However, the low charge density at physiological pH also leads to low solubility, aggregation and poor stability of chitosan-based formulations depending on type of chitosan used. The majority of the chitosan-mediated gene delivery studies are performed with a few off-the shelf chitosans of given composition and properties. Bearing in mind that the family of chitosans spans over a range of polymers with highly variable properties, it is clear that different chitosan samples may give highly variable outcome in a particular application. On the other hand, understanding of the structure-property relationship will open for tailoring of chitosans with optimal properties for a given application.

General consensus is that a successful polymer-based gene transfer requires a subtle balance between sufficient DNA protection and intracellular DNA release which reflects the degree of interaction between the gene carrier and its DNA cargo [6-8]. Therefore, the structure of the polymer carrier (charge density, chain length) and stoichiometry of the complexes are key determinants of the transfection efficacy. A clear correlation between chain length of the polymer and transfection efficacy has been reported for poly-L-lysine (PLL) [8] and

polyethylenimine (PEI) [9, 10] but conflicting results may be found for chitosan [7, 11-13]. Although a few studies promote the use of high molecular weight (M_w) chitosans [11, 13, 14], the chitosans of lower M_w seem to be superior for gene delivery [7, 12]. It has been shown that the chitosan with M_w of 10 kDa and fraction of acetylation (F_A) 0.08 – 0.2 seemed particularly efficient compared to 40 kDa chitosan and higher M_w [12]. On the other hand, chitosan oligomers below 5 kDa and F_A 0 showed poor gene delivery in vitro [7, 15]. Based on the data available, it seems that the optimal chitosans for gene delivery have M_w in the range of 5 – 40 kDa. This range of molecular weights has not been systematically investigated yet and we have hypothesized that by creating a series of chitosans with chain lengths within this range and studying their gene transfer capabilities, the optimum chain length may be revealed with finely tuned balance between DNA protection and polyplex unpacking.

Apart from chitosan chain length, the degree of interactions between chitosan and DNA may also be controlled by targeted derivatisation inducing hindrance. Our recent work with glycosylated chitosans revealed that the substitution of chitosan with uncharged GlcNAc-containing trimers weakened the binding interactions but increased transfection efficacy [16, 17].

The overall goal of this study was to gain insights into the structure-function relationship in chitosan-mediated transfection. We hypothesized that polyplex disassembly depends on the degree of interaction between chitosan and its pDNA cargo which may be controlled by the chitosan design. To test this hypothesis, we have prepared series of low molecular weight chitosans with constant charge density where we systematically varied i) degree of polymerization (Mw 4.7 – 40 kDa) and ii) degree of hindrance, and examined the influence of these parameters on gene transfer. Using these chitosans, we have studied the relationship between the chain length and formulation properties, cellular uptake, gene transfer efficacy, and intracellular trafficking. Furthermore, systematic substitution of chitosans with GlcNAc-

containing oligosaccharides has been performed to create series with variable degree of substitution, degree of polydispersity, and size of substituents. Studying the structure-activity relationship across the series verified that the charge-based interaction between chitosan and pDNA and thereby the gene transfer efficacy may be controlled by tailoring of the chitosan structure.

Materials and methods

Cell culture. Human embryonic kidney cell line HEK293 was obtained from ATCC (Rockville, MD) and cells between passage nr. 39 and 60 were used in all experiments. The HEK293 were grown in MEM (Gibco Invitrogen) supplemented with 1 mM of non-essential amino acids and 10 % fetal bovine serum (FBS) (Gibco Invitrogen) at 37^0C and 5 % CO_2.

Plasmid DNA. Reporter plasmids (gWiz^{TM}Luc and gWiz^{TM}GFP) (approximately 6.7 kb) containing a cytomegalovirus promoter (CMV) and firefly luciferase (Luc) or green fluorescent protein (GFP) were purchased (Aldevron, Fargo, ND). When indicated, plasmid DNA was labeled by YOYO-1 (Molecular Probes, Eugene, OR) using a molar ratio of 1 dye molecule per 100 base pairs at room temperature in the dark.

Chitosans. Chitosan oligomers with number average degrees of polymerization (DP_n) in the range of 21 – 88 were prepared by nitrous acid depolymerization of fully de-N-acetylated chitosan ($F_A < 0.002$, M_w 146 kDa) as described earlier [18]. To obtain desired chain length, the amount of sodium nitrite were varied from 0.02 to 0.14 mol/mol GlcN. To prepare the substituted oligomers (TCO), depolymerized chitosans were then reduced by $NaBH_4$ and reductively N-alkylated with the trimer 2-acetamido-2-deoxy-D-glucopyranosyl-β-(1-4)2-acetamido-2-deoxy-D-glucopyranosyl-β-(1-4)-2,5-anhydro-D-mannofuranose (A-A-M) as described previously [19]. All TCO samples were characterized by ^{1}H-NMR to determine the degree of substitution. The average degrees of polymerization and chain length distributions for

both series were analyzed by size-exclusion chromatography (SEC) with refractive index (RI) detector (Dawn Optilab 903, Wyatt Technology Corp., CA) and a multiangle laser light scattering detector (MALLS, Dawn DSP, Wyatt Technology Corp., CA) [20]. All samples were dissolved in Milli-Q (MQ) water (5 – 7 mg/mL) and filtered through 0.22 μm syringe filter (Millipore Corp., MA). The column used was TSK 3000 PWXL, and the sample was eluted with 0.2 M ammonium acetate (pH 4.5) at a flow rate of 0.5 mL/min. For simplicity, the linear chitosan oligomers are denoted as linear whereas the trisaccharide substituted chitosan oligomers are denoted as TCO. The characteristics of the chitosans used in the study are given in Table 1.

When indicated, a low-molecular-weight chitosan with a number average DP_n21 was fractionated by size-exclusion chromatography on Superdex 30 columns into fractions corresponding to DP intervals of 10 – 15, 16 – 22, 23 – 27 and 28 – 50.

For CLSM and FCS, chitosan was labeled by Alexa Fluor 647 carboxylic acid, succinimidyl ester (Molecular Probes, Eugene, OR) using a molar ratio of 1 dye per 200 glucosamine residues. The transfection efficacy of labeled chitosans was comparable to that of unlabeled chitosans.

Solubility of chitosans. 0.05 mL aliquots of 2 mg/mL solution of chitosans in MQ water were transferred to 96-well plate and diluted to 0.1 mL by double strength Hanks balanced salt solution (HBSS, Gibco Invitrogen) supplemented with 20 mM HEPES (Sigma-Aldrich, MO) with pH in the range of 6.5 – 8.0. After 1 h incubation at room temperature and shaking, the absorbance of the solution was measured at 400 nm on TECAN Safire^2 (Tecan Austria GmbH, Austria).

Preparation of chitosan/pDNA polyplexes. Polyplexes with different amino/phosphate (A/P) ratios and pDNA concentration of 13.3 μg/mL were prepared by the self-assembly method. The

constant amount of pDNA solution (0.5 mg/mL) was diluted in MQ water and then required amount of sterile filtered chitosan stock solution in MQ-grade water (2 mg/mL) was added during intense stirring on a vortex mixer (1200 rpm). The complexes were incubated for 30 minutes at room temperature prior to transfection.

Size and surface charge analysis. The size of the chitosan/pDNA polyplexes was determined by dynamic light scattering on a Zetasizer Nano Zs (Malvern Instruments, UK). The measurements were performed at an angle of 173^0 and a temperature of 25°C and each sample was analyzed in triplicate. The size of the polyplexes is expressed as mean diameter (z-average) obtained by cumulant analysis of the correlation function using the viscosity and refractive index of water in the calculations. For measurements of aggregation kinetics, the polyplexes were diluted 1:2 with double HBSS pH 7.0 to obtain the isotonic formulations similarly as in transfection experiments, and the size was repeatedly measured over a period of 120 min. Surface charge (zeta potential) was determined by Doppler velocimetry on the same instrument.

Gel retardation assay. The pDNA retention capacity of the polyplexes and heparin induced release of pDNA was studied using gel electrophoresis. The polyplexes were prepared as described above at a constant pDNA concentration of 13 μg/mL and A/P ratios of 5, 10, 20, and 30 and incubated for 30 min. Next, the polyplexes were diluted 1:2 in transfection medium with and without 100 μg/mL heparin and incubated at 37°C and 5 % CO_2 for 4 h and overnight, respectively. After incubation, 10 μL of the complex solution was mixed with 5 μL of loading buffer and loaded on 0.8 % agarose gel containing 0.5 μg/ml ethidium bromide (EtBr). The gel electrophoresis was run in 40 mM Tris-acetate-EDTA (TAE) buffer at pH 7.4 at 80 V for 45 min.

In vitro transfection experiments. HEK293 cells were seeded in 96-well tissue culture plates 24 h prior to the transfection experiments to obtain cell confluency of 80 – 90 % on the day of transfection. The polyplexes formulated in MQ water were diluted 1:2 by OptiMEM (OptiMEM

I, Gibco Invitrogen) supplemented by 270 mM mannitol and 20 mM HEPES to adjust osmolality and pH. Cells were washed with pre-heated OptiMEM and 50 µL of isotonic formulation containing 0.33 µg pDNA was added to each well. After 5 h of incubation, the formulations were replaced by 200 µL of fresh culture medium (MEM, 10 % FBS). Culture medium was changed every second day. To determine luciferase expression, cells were washed twice with pre-heated PBS, lysed with luciferase lysis buffer (Promega) and the luciferase activity (expressed in relative luciferase units, RLU) was measured on a luminometer (Molecular Devices, CA). The total cell protein was determined by bichinchoninic acid assay (Pierce).

Flow cytometry. Flow cytometry analysis of GFP expressing cells or polyplex uptake with YOYO-1 labeled pDNA was performed using a BD LSR1 (Becton Dickinson, San Jose, CA). Cells were incubated with YOYO-1 labeled polyplexes for 3 h and washed twice with 1 mg/mL heparin solution to dissociate and remove cell surface associated complexes. Cells expressing GFP were analyzed 48 h after transfection. Prior to flow cytometry analysis, cells were washed twice in PBS, trypsinised, resuspended in ice-cold PBS supplemented with 2 % FBS and kept on ice. For each sample, 10 000 events were counted and a dot plot of forward light scatter against side scatter was used to establish a collection gate to exclude the cell debris and dead cells showing reduction in the forward scatter as well as aggregates of cells. The GFP or YOYO-1 positive cells were excited by 488 nm laser line and detected using a 530/30 nm band pass filter. To distinguish between autofluorescence and fluorescently labeled cells, non-transfected cells were run as negative controls. The percentage of cells expressing GFP was calculated and the relative amount of expressed GFP was estimated from the median fluorescence intensity of GFP positive population. The cellular uptake of the polyplexes was calculated as the percentage of YOYO-1 labeled cells and the relative amount of internalized pDNA was estimated from the median fluorescence intensity of YOYO-1 positive population.

Confocal laser scanning microscopy (CLSM). HEK293 cells were seeded on 8-chambered microscopic slides (Ibidi GmbH, Germany) and transfected as described above. After 2 h of incubation at 37°C and 5 % CO_2, live cells were examined using LSM 510 (Carl Zeiss Jena GmbH, Germany) with a C-Apochromat 40x/1.2 W corr objective. The cell nuclei were stained by incubating the cells with 5 µg/mL Hoechst 33342. YOYO-1 and Alexa Fluor 647 were excited by 488 nm argon laser line and 633 nm HeNe laser line, respectively and the emitted light was detected through BP500-550 and LP650 filter. Hoechst 33342 was excited using two-photon excitation obtained by a modelocked Ti:Sapphire laser (Mira Model 900-F, coherent Inc., Laser Group, Santa Clara, CA, USA) at 780 nm.

Fluorescence correlation spectroscopy (FCS). FCS measurements were performed using the LSM 510/Confocor2 (Carl Zeiss Jena GmbH, Germany) with a C-Apochromat 40x/1.2 W corr objective as previously described [21]. Briefly, Alexa Fluor 647 was excited using a 633 nm HeNe laser line and the emitted light was filtered through a LP650 filter before being collected. A pinhole diameter of 90 µm was used. The point of interest in a cell (either in the nucleus or in the cytoplasm) located 3 to 8 µm above the cover glass was chosen using confocal microscopy. The point of interest was bleached for 20 seconds previous to measurements to eliminate possible noise caused by cell autofluorescence or by completely immobilized fluorescent molecules. Autocorrelation curves were obtained by performing 5 measurements for 15 seconds at the point of interest and analyzed as previously described [22] using the two-component free diffusion model provided by the Confocor2 software. The apparent concentration was defined as the observed number of particles in the detection volume divided by the detection volume. The size of the detection volume was calibrated as previously described. [21]

Statistical analysis. All measurement data were collected and expressed as mean values ± standard deviation (SD). Statistical differences between mean values were investigated using

ANOVA in conjunction with a multiple comparison test (Tukey test). Differences between means were considered significant at $p \leq 0.05$.

Table 1 Characterization of chitosan samples used. The molecular weights (M_w, M_n) and molecular weight distribution were analyzed by SEC-MALLS. The degree of substitution (d.s.) of A-A-M was determined by ^{1}H NMR.

Sample	**F_A**	**linear**			**TCO**			
		M_n	M_w	PDI	M_n	M_w	PDI	d.s.
DP_n21	< 0.002	4200	4700	1.12	5000	6000	1.20	8.0
DP_n31	< 0.002	6300	8000	1.28	7100	9800	1.36	7.8
DP_n42	< 0.002	8500	11600	1.37	9900	14100	1.42	7.8
DP_n54	< 0.002	10800	16400	1.52	12800	20100	1.56	7.5
DP_n72	< 0.002	14500	24800	1.71	17600	30100	1.71	7.8
DP_n88	< 0.002	17600	32900	1.87	21800	39500	1.81	7.6
DP_n400	< 0.002	85900	146000	1.70	102000	174000	1.71	8.3

Results

Effect of chain length on gene transfer efficacy of chitosan

To investigate how the chain length of chitosan affects transfection efficacy, a series of low molecular weight chitosans was prepared and used as gene carriers for transfection of HEK293 cells. After preliminary screening of optimal A/P ratios for all chitosans (data not shown), three to four formulations with A/P ratios from 3 to 20 were prepared from each chitosan and compared for luciferase gene expression. As reported previously [17], transfection efficacy of chitosan oligomers is highly pH-dependent and impaired at pH 7.4 and the experiments were thus performed at pH 7.0. The results presented in Fig. 1a,b show that both the DP_n and the A/P ratio clearly affected transgene expression. The polyplexes formed by DP_n31 and DP_n42 mediated the highest luciferase expression in HEK293 at 48 h (Fig. 1b). For all chitosans, gene expression varied with the composition of polyplexes given by the A/P ratio. Generally, the transgene expression increased with increasing A/P ratio to a certain point and then declined.

This effect was most pronounced for the shortest and longest oligomers in the series, DP_n21 and DP_n88. The optimal A/P ratio depended on the chain length of chitosan following a general trend showing the higher DP, the lower the optimal A/P ratio. The luciferase gene expression mediated by the non-degraded original chitosan sample with DP_n 400 (M_w 146 kDa) at any A/P ratio was far below the levels obtained with the depolymerized chitosans. Furthemore, comparison of the total cellular protein levels in cell lysates during the luciferase analysis revealed similar extent of cell proliferation, and thereby no differences in relative toxicity of the formulations.

To compare transgene expression on a single cell level, the HEK293 were transfected with an identical plasmid carrying GFP instead of luciferase and the percentage of GFP expressing cells in the population was determined 48 h after transfection as shown in Fig. 1c. Despite large differences in luciferase production, all oligomers showed close to 50 % of transfected cells at optimal A/P ratios. The percentage of transfected cells decreased at suboptimal A/P ratios for all formulations.

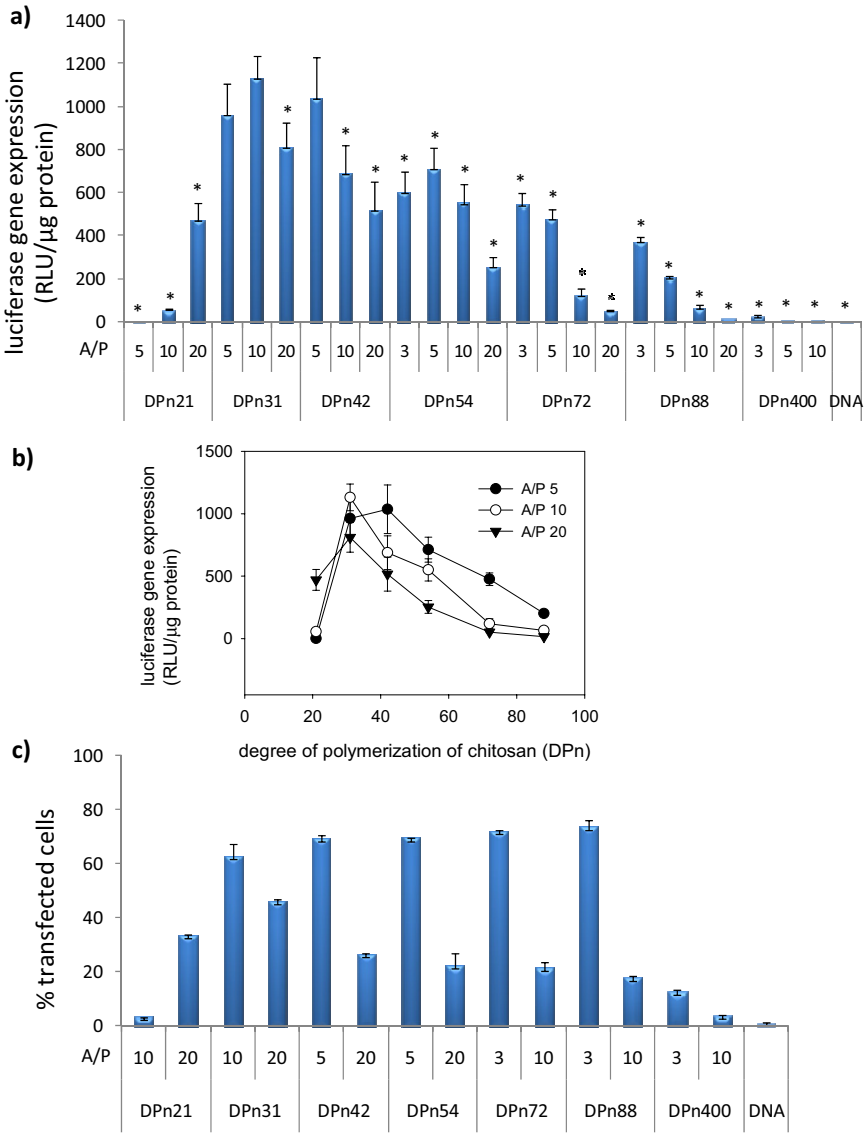

Figure 1 Transfection efficacy of depolymerized chitosans in HEK293 cells. a) Luciferase gene expression 48 h after transfection using polyplexes formed with chitosans with degrees of polymerization (DP_n) from 21 to 400 and amino-phosphate (A/P) ratios of 3 – 20. b) Results of a) plotted as a function of degree of polymerization of chitosan. c) Percentage of GFP transfected cells 48 h after transfection. All data points represent mean ± SD, n = 4. Formulations yielding efficiency significantly different from the DP_n31 formulation at A/P 10 are indicated by an asterisk ($n = 4$, $p < 0.05$).

Fig. 1 shows transfection efficacy at 48 h after transfection. To examine whether the different chitosan formulations exhibited different transgene expression kinetics, the time course of the luciferase expression was measured. As shown in Fig. 2, the kinetics of transgene expression was influenced by the A/P ratio. In case of DP_n31 (Fig. 2a), the formulations with A/P 3 and 5 mediated the highest expression at 48 – 72 h and then the luciferase production declined. On the contrary, in cells transfected with formulations with A/P 10 and 30, luciferase levels continuously increased up to 96 h. Similar trends in transgene expression kinetics were found for DP_n31 and DP_n88, but the total luciferase production was substantially lower after transfection with DP_n88.

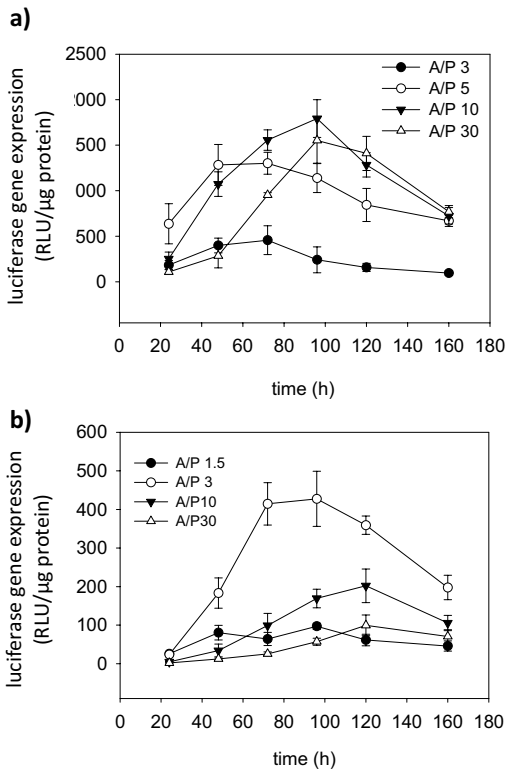

Figure 2 Time course of luciferase gene expression in HEK293 cells transfected by a) DP_n31 and b) DP_n88 at different A/P ratios. Data points represent mean ± SD, n = 4.

Physicochemical characterization of polyplexes

To scrutinize the reasons for variable efficacy of depolymerized chitosans, we examined the sequence of events during a transfection experiment to reveal in what stage of the transfection process the chain length is important.

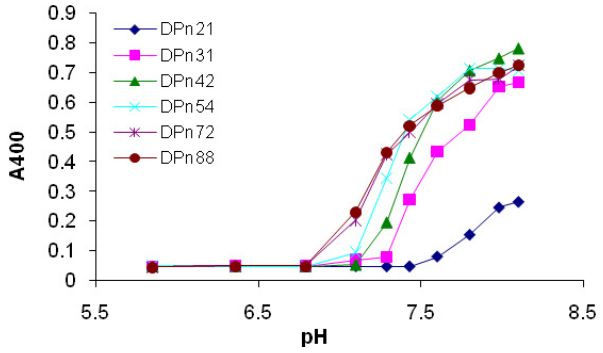

Supplementary Figure S1 pH-dependent solubility of chitosan in HBSS measured as absorbance at 400 nm (A400).

The complexation of pDNA by chitosan was carried out in MQ water at pH < 5.5 to assure full solubility of chitosans (see Fig. S1 in supporting information), strong electrostatic interactions, and large entropic contribution driving the formation of complexes. Under these conditions, all depolymerized chitosans (DP_n21 – DP_n88) at A/P 5 formed polyplexes with z-average diameter in the range of 60 – 70 nm and zeta potential of 18 ± 6 mV. The diameters of polyplexes slightly increased with increasing chain length from 59.6 ± 2.5 nm for DP_n21 to 69.9 ± 3.1 nm for DP_n88. The chitosan with DP_n400 formed larger polyplexes, approximately 85 ± 4 nm. The size of polyplexes remained stable from about a few minutes after preparation to at least 2 weeks after preparation, provided storage in MQ water (data not shown).

Prior to cell transfection, the polyplexes were diluted with hypertonic medium (OptiMEM with 20 mM Hepes and 270 mM mannitol, 590 mM) in order to obtain isotonic formulations. In agreement with a previous report, polyplexes rapidly aggregated in transfection medium but were

still able to transfect the cells [16, 17]. To examine possible chain length influence on the extent of aggregation, we have compared the kinetics of aggregation of all polyplexes at A/P 5. Fig. 3 shows that following dilution of polyplexes in transfection medium, all complexes rapidly aggregated into micrometer large structures. The degree of aggregation slightly increased with increasing DP_n.

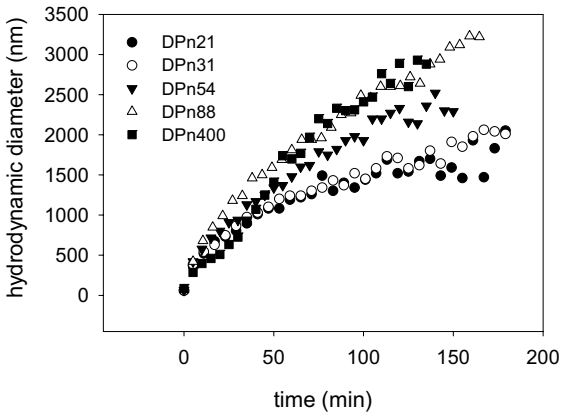

Figure 3 Time-dependent aggregation of polyplexes formed by linear chitosans with DP_n21 – 400 at A/P 5 following dilution in HBSS at pH 7.0 (final concentration of pDNA 6.6 µg/mL).

Cellular uptake of polyplexes

The aggregation of polyplexes leads to increased sedimentation of polyplexes on the cell surface. To compare the degree of uptake of polyplexes by HEK293 cells, internalized polyplexes labeled by YOYO-1 were determined by flow cytometry after extensive washing of the transfected cells by medium containing 1 mg/mL of heparin. Almost all cells internalized the polyplexes, each formulation was taken up by 95 ± 2 % cells. The exceptions were polyplexes of DP_n21 at A/P 10 and DP_n400 at A/P 10 which were internalized only by 85 % cells. Naked pDNA (pWizLuc) was detected in 40 % cells. Although the percentage of YOYO-1 positive cells was similar for all chitosans and A/P, the amount of internalized pDNA determined from median fluorescence intensity levels varied as shown in Fig. 4a. Cells transfected with naked pDNA and DP_n21 at A/P 10 exhibited extremely low fluorescence. The

highest fluorescence levels were measured in cells transfected by DP_n72 and 88 at A/P 3. Interestingly, formulations with higher A/P ratios showed lower amounts of internalized pDNA. As shown in Fig. 4b, there was no apparent correlation between the uptake of pWizLuc and luciferase gene expression.

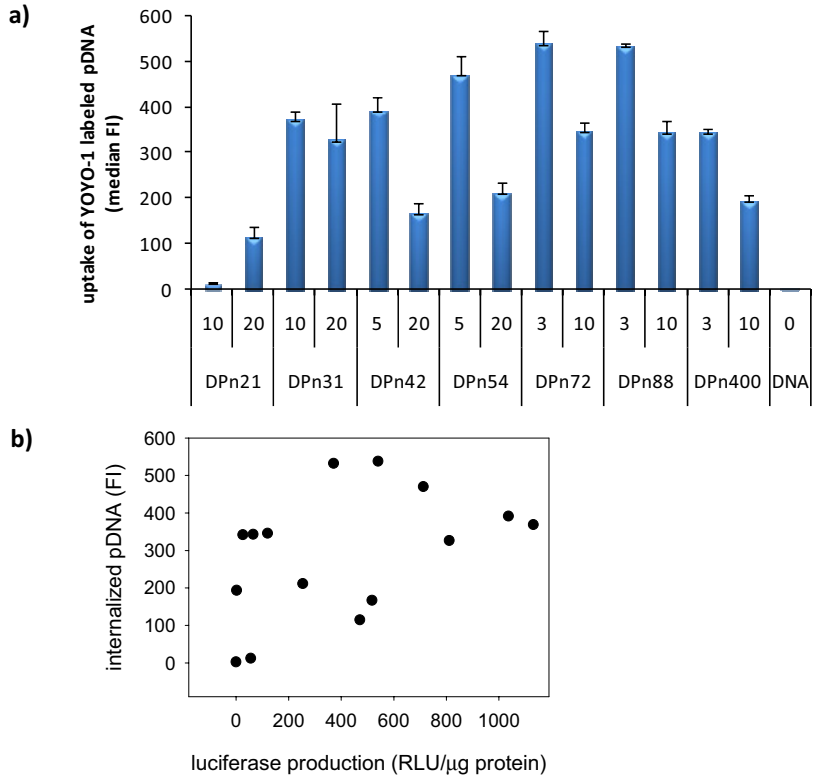

Figure 4 Uptake of YOYO-1 labeled polyplexes in HEK293. The percentage of YOYO-1 positive cells and the median of fluorescence intensity (FI) was determined by flow cytometry. a) median FI of YOYO-1 positive cells transfected by different chitosan formulations and b) correlation between pWizLuc uptake and expression. Data points represent mean ± SD, n = 4.

Polyplex dissociation

Bearing in mind the lacking correlation between the uptake of polyplexes by HEK293 cells and transfection efficacy, the differences in relative transfection efficacy of chitosans seem to result

from different intracellular fate of the polyplexes. Clearly, the chain length of the polycation and the amount of polycation in the polyplex are crucial factors governing the stability of the polyplex. To compare the pDNA retention ability under transfection conditions, the polyplexes were incubated in transfection medium at 37°C for 4 h and then subjected to gel electrophoresis at pH 7.4. As shown in Fig. 5A, with exception of the polyplexes formed by DP_n21 at A/P 5 and 10, all polyplexes were stable and retained all complexed pDNA. To mimic intracellular conditions, the polyplexes were incubated overnight in the transfection medium supplemented by 100 µg/mL heparin as a competing polycation. As shown in Fig. 5b, pDNA was released from all complexes formed at A/P 5 and 10 except those formed by DP_n400. The extent of the release of pDNA decreased with increasing A/P of the formulation and chain length of the chitosan. Whereas formulations prepared from DP_n21 released almost all pDNA at all A/P, polyplexes formed by DP_n54 and DP_n88 retained all pDNA at A/P 20. Interestingly, pDNA released from the polyplexes showed lower fractions of supercoiled conformation and higher fractions of open circular form compared to naked pDNA.

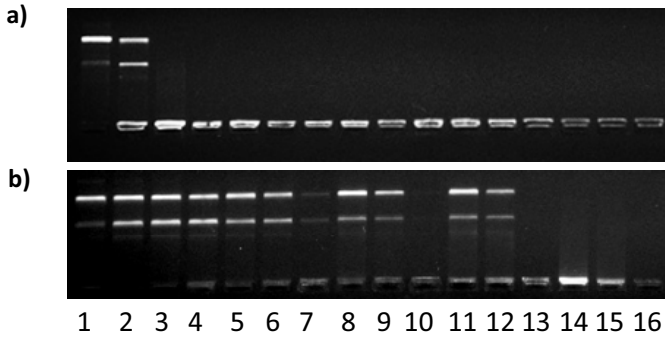

Figure 5 Stability of chitosan/pDNA polyplexes elucidated by gel electrophoresis. Complexes with chitosans with DP_n 21, 31, 54, 88 and 400 and A/P 5, 10, 20 were incubated in Optimem at 37°C for a) 4 h and b) overnight in presence of 100 µg/mL heparin and subjected to gel electrophoresis in TAE buffer at pH 7.4. Lane 1: naked pDNA, lane 2 – 4: DP_n21 at A/P 5, 10, 20, lane 5 – 7: DP_n31 at A/P 5, 10, 20, lane 8 – 10: DP_n54 at A/P 5, 10, 20, lane 11 – 13: DP_n88 at A/P 5, 10, 20, lane 14 – 16: DP_n400 at A/P 5, 10, 20.

Gene transfer efficacy of glycosylated chitosans: effect of chain length

To further strengthen the hypothesis that it is the interaction strength between pDNA and chitosan that determines the gene transfer efficacy, we have prepared a series of trimer substituted chitosan oligomers (TCO) and compared the effect of chain length and A/P ratio before and after substitution. Fig. 6 shows the transfection efficacy in the series of TCO (8 % d.s) differing in chain length.

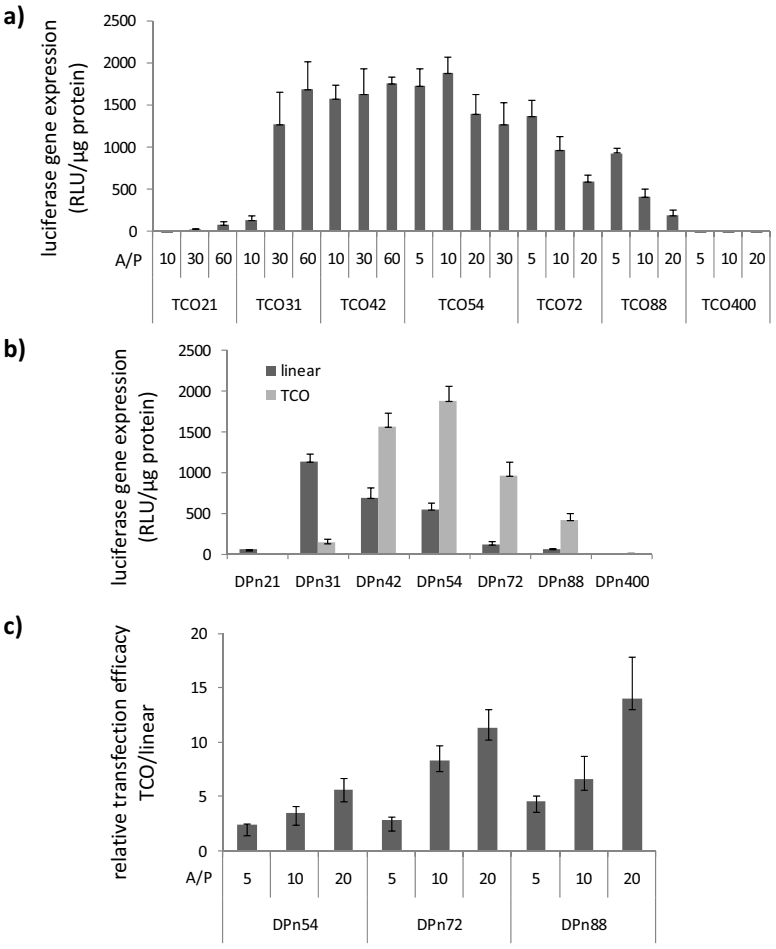

Figure 6 Transfection efficacy of glycosylated oligomers in HEK293 cells. a) Luciferase gene expression 48 h after transfection. b) Comparison of linear and TCO oligomers at A/P 10. c) Relative transfection efficacy (TCO/linear) as a function of A/P ratio.

Compared to unsubstituted oligomers (Fig. 1a), there is a noticeable shift towards higher effective A/P ratios for short oligomers, i.e. more polycation had to be used to complex pDNA. As demonstrated in Fig. 6a, several formulations showed a comparable transfection efficacy, however at widely differing A/P ratios; DP_n31 at A/P 60 was equal to DP_n54 at A/P 5. The interval of optimal transfection efficacy was broader for TCOs than that for linear oligomers and the effect of A/P was less dominating.

Fig. 6b shows the comparison of transfection efficacies of linear oligomers and TCOs at a constant A/P ratio of 10. The effect of A-A-M substitution on transfection efficacy is strictly dependent on the chain length of the chitosan. In case of shorter oligomers such as DP_n21 and 31, the substitution resulted in a dramatic decrease or even a complete loss of activity, whereas it increased the efficacy of chitosans over DP_n42. The longer the chain, the higher increase in transfection efficacy after substitution. Similarly, the positive effect of glycosylation is more apparent at higher A/P ratios as shown in Fig. 6c.

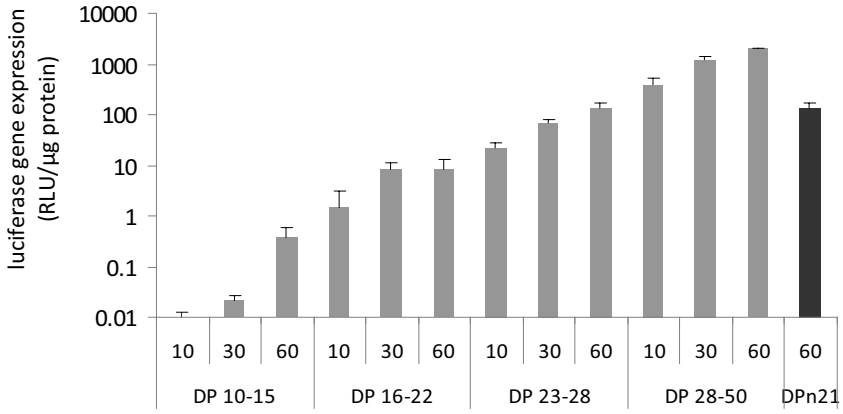

Figure 7 Luciferase gene expression in HEK293 cells transfected with fractionated TCO with DP_n21. TCO21 was fractionated into four different fractions DP 10 – 15, DP 16 – 22, DP 23 – 28 and DP 28 – 50 using gel permeation chromatography. The original chitosan oligomer (DP_n21) is shown in black and the fractionated chitosans are shown in grey.

Clearly, the substitution of DP_n21 almost completely eliminated gene transfer. To investigate the critical chain length necessary to mediate transfection, TCO21 was fractionated by gel permeation chromatography into defined fractions of DP 10 – 15, 16 – 22, 23 – 28 and 28 – 50. These fractions were then substituted by A-A-M and evaluated as gene carriers. As shown in Fig. 7, the transfection efficacy exponentially increased with increasing chain length and A/P ratio and only the fraction containing the chains in the range of DP 28 – 50 showed efficient delivery. The unfractionated original sample DP_n21 had one order of magnitude lower transfection efficacy than the fraction containing chains with DP 28 – 50. Apparently, only the chitosan chains above 28 monomer residues were able to mediate transfection.

Effect of the length of substituent

To confirm the crucial role of well-balanced interactions between chitosan and pDNA, we chose two depolymerized chitosans with average DP_n34 and DP_n88 and synthesized a systematic series of glycosylated chitosans where we varied the length of the substituent from dimer A-M to pentamer A-A-A-A-M. Gel electrophoresis assay confirmed that the polyplex stability decreased with the length of the substituent (data not shown). Fig. 8 shows that the effect of substitution is strongly linked to the charge ratio and the length of the chitosan backbone. For polyplexes formed by DP_n34 (Fig. 8a) at A/P higher than 10, the substitution of chitosan by the dimer and trimer increased transfection efficacy whereas the pentamer substitution decreased transfection efficacy. At A/P 10, gene transfer efficacy was negatively influenced by glycosylation and luciferase expression was found to decrease with increasing size of the substituents. For DP_n88 (Fig. 8b), all substitutions improved gene transfer efficacy. The maximum luciferase expression was achieved with trimer- and pentamer-substituted chitosans, with the latter less sensitive to A/P ratio.

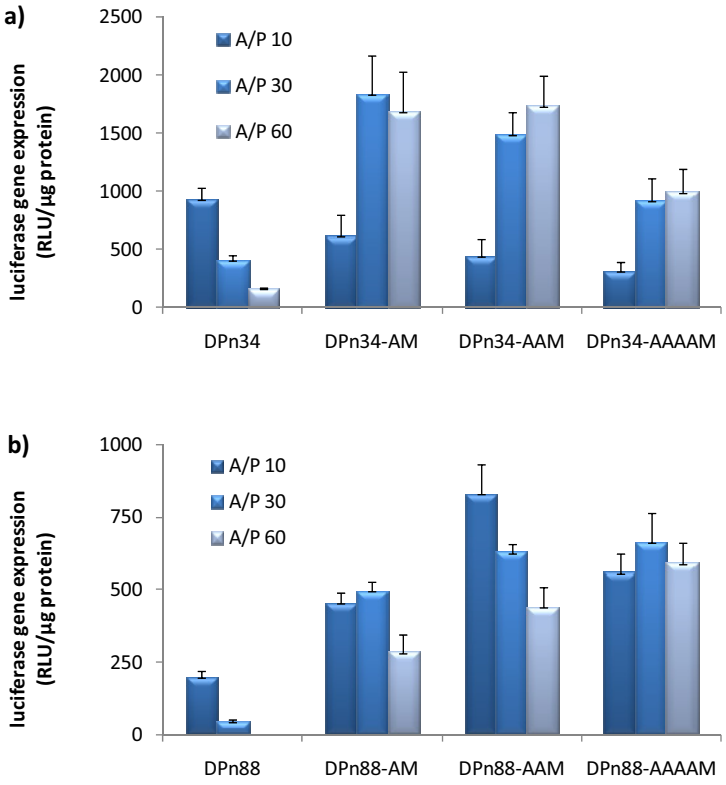

Figure 8 Transfection efficacy of glycosylated DP_n34 (a) and DP_n88 (b) in HEK293 cells. Chitosans were substituted with dimer (A-M), trimer (A-A-M) and pentamer (A-A-A-A-M) at a degree of substitution of 7 % .

CLSM and FCS

To elucidate the intracellular polyplex stability and transport within the cells, HEK293 cells were transfected with polyplexes that were double-labeled with YOYO1 and Alexa Fluor 647, and imaged by CLSM to investigate whether and where they remained intact or disintegrated within the cells. Chitosans DP_n31 and DP_n88 were used as delivery vehicles based on the highly different transfection efficacy of their respective polyplexes at A/P 10.

CLSM images were acquired of living cells transfected by polyplexes formed by DP_n31 (Fig. 9a,b) and DP_n88 (Fig. 9c,d). The polyplexes were clearly aggregated and large structures were

observed both inside and outside the cells, especially for DP_n88. For both chitosans, it was possible to find cells where most of the pDNA appeared free (Fig. 9b,d) as well as cells where large chitosan aggregates but no pDNA were seen (Fig. 9a,c). There was a larger variation within a cell population treated by the same polyplex than between the different chitosan formulations. Apparently, the cells internalized the polyplexes and both pDNA (free and chitosan-associated) and free chitosans were found in the nucleus approximately 1 h after transfection.

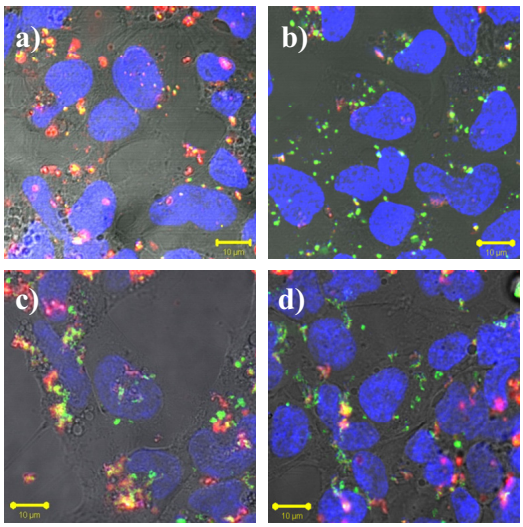

Figure 9 CLSM images of HEK293 cells transfected with polyplexes formed by chitosans DP_n31 (a,b) and DP_n88 (c,d). Chitosans were labeled by Alexa Fluor 647 (red) and pDNA by YOYO-1 (green). The cell nuclei were labeled with Hoechst 33342 (blue). The bar size is 10 µm.

To obtain more quantitative characterization of the dynamics of the intracellular transport of polyplexes to the cytoplasm and nucleus, FCS was used to measure the diffusion times and determine the apparent concentration of Alexa Fluor 647-labeled chitosans. The essential pre-requisite for FCS is that the measured molecules are mobile, i.e. free to diffuse through the excitation volume. Therefore, low mobility of free pDNA as well as the autofluorescence of HEK293 cells complicated the measurements of YOYO-1-labeled pDNA, which emits

fluorescence in the same spectral interval as autofluorescence. Thus only chitosan could be tracked by FCS. Intracellular trafficking of both polyplexes and free chitosan were studied, and in both cases the experimental autocorrelation curves were well fitted by the two-component free diffusion model, demonstrating a fast and slowly diffusing population. The fast and slow diffusion coefficients, D_1 and D_2, presented in Table 2 are representative of diffusion in cytoplasm and nucleus 1 h and 24 h after incubation with either free chitosans or polyplexes. The fast diffusing population in cells incubated with polyplexes is probably free chitosan as the diffusion coefficient is equal to the fast diffusion coefficient measured in cells incubated with free chitosan. This diffusion coefficient was lower than the diffusion of chitosan measured in solution (data not shown), demonstrating that the diffusion of the chitosans are somewhat hindered intracellularly. The slow diffusion coefficient D_2 was attributed to chitosan bound to cellular components or pDNA. Because of the similarity of D_2 after incubation with free chitosan and polyplexes, it was not possible to distinguish whether chitosan was bound to cellular components or to pDNA in cells after incubation with polyplexes.

Table 2 Diffusion coefficients of free chitosan and polyplexes in HEK293 nucleus 24 h after transfection. The diffusion coefficients were calculated from FCS autocorrelation functions analyzed with a two-component free diffusion model.

Sample	**Diffusion coefficients of free chitosan ($\times 10^{-12} m^2 s^{-1}$)**		**Diffusion coefficients of polyplexes ($\times 10^{-12} m^2 s^{-1}$)**	
	$D_1 \pm SD$	$D_2 \pm SD$	$D_1 \pm SD$	$D_2 \pm SD$
DP_n31	51.7 ± 5.1	5.7 ± 0.6	46.3 ± 3.8	4.8 ± 0.6
DP_n88	61.8 ± 2.3	6.2 ± 0.5	57.0 ± 3.6	4.3 ± 1.1

Analysis of autocorrelation curves enabled determination of the apparent intracellular concentration of chitosan in the excitation volume. Fig. 10 compares the concentration of chitosans DP_n31 (Fig. 10a) and DP_n88 (Fig. 10b) in HEK 293 cytoplasm and nucleus, 1 h and

24 h after incubation with either free chitosans or polyplexes. Apparently, the cells internalized more chitosan after incubation with polyplexes than with free DP_n31 and DP_n88. The amounts of internalized DP_n31 and DP_n88 in cytosol and nucleus seem to be comparable when measured 1 h after incubation of cells with free chitosan. On the contrary, when incubating HEK 293 cells with polyplexes, differences were observed in the accumulation of DP_n31 and DP_n88. Only polyplexes of DP_n88 showed intranuclear accumulation after 24 h. The same amount of polyplexes of DP_n31 was found in the nucleus at the two time points, whereas the concentration of the slowly diffusing population increased in the cytoplasm.

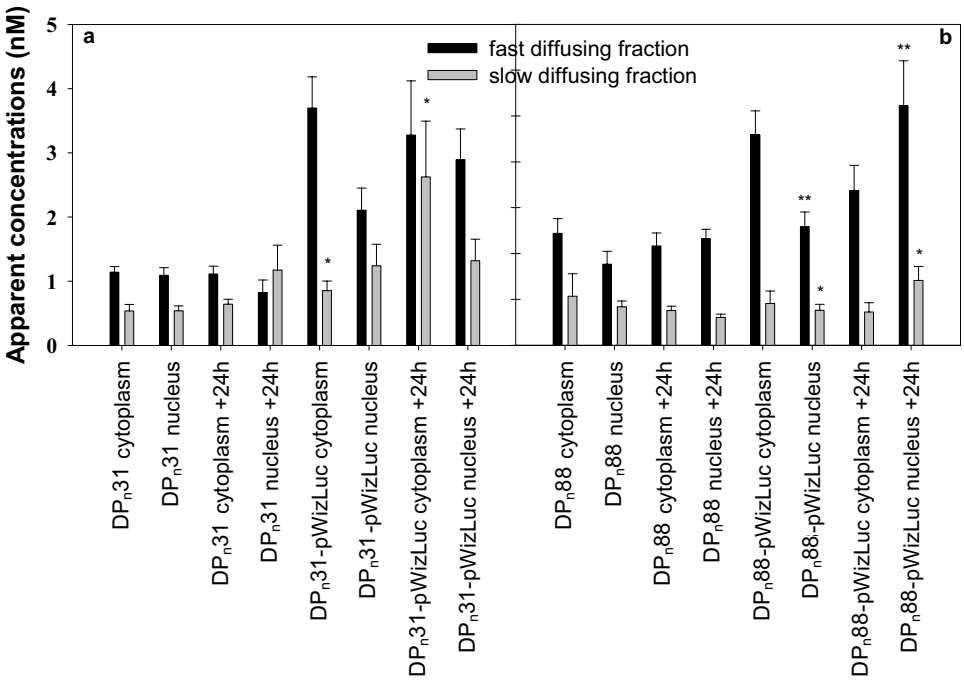

Figure 10 Apparent concentrations of chitosans DP_n31 (a) and DP_n88 (b) in the cytosol and nucleus of HEK293 cells 1 h and 24 h after incubation with free chitosan or polypexes. Significant differences in the apparent concentrations of bound chitosan and/or polyplexes after 1 h and 24 h incubation are indicated by an asterisk while significant differences in the apparent concentrations of freely diffusing chitosan after 1 h and 24 h incubation are indicated by two asterisks.

Discussion

Despite numerous reports on the use of chitosan for gene delivery, the understanding of the relationship between the structure of chitosan and its transfection efficacy is still incomplete. The transfection efficacy has been shown to depend on molecular weight [7, 11, 12], chemical composition [12, 14, 23, 24], pH [24], and serum presence [25], but the reported results are not always consistent and there is a lack of consensus what are the ideal molecular parameters and conditions for efficient transfection as well as rational explanation for these. The discrepancy may be partly explained by poor availability of suitable samples with precisely defined molecular structure and differences in the formulation properties. Here, we have performed a systematic structure-function study on chitosan-mediated gene transfer to test the hypothesis that it is the strength of charge-based interaction with pDNA which determines the polyplex dissociation and thereby the magnitude of gene transfer with chitosan. By precise tuning of the chitosan properties such as the chain length and the extent of hindrance, ideal balance between pDNA protection and release may be obtained, leading to high gene transfer efficacy.

We have previously shown that chitosan oligomers in the range of DP_n 18 – 25 mediated more efficient gene transfer than high M_w chitosan (210 kDa) but had still relatively low gene expression in vitro compared to 25 kDa PEI [7]. To improve the transfection efficacy, derivatisation strategies based on glycosylation have been developed [16, 17, 26]. Although having lower gene transfer efficacy than the glycosylated chitosans, the linear low molecular weight chitosans with constant charge density and M_n in the range of 4 – 20 kDa used in this study, represent an ideal model system to study the role of charge-based interaction with pDNA in chitosan-mediated gene transfer. The transfection efficacy of linear oligomers clearly depended both on chitosan chain length (DP_n) as well as its amount available for complex formation (A/P) (Fig. 1a). As the DP_n is proportional to the valency of the polycation and the A/P ratio is proportional to the total number of charges, these results highlight the principal role

of charge-based interactions [27]. Similarly as for low molecular weight linear PEIs [9], it was possible to compensate for lower affinity by increasing the amount of charges to a certain degree, as decreasing chain lengths lead to higher amounts of chitosan necessary to form a functional polyplex and vice versa. However, we were able to identify a narrow interval of chain lengths between DP_n 30 – 40 (M_n 6.3 – 8.5 kDa) mediating superior transgene expression irrespective to the A/P ratio (Fig. 1b). Interestingly, comparing the magnitude of transgene expression with the percentage of transfected cells indicates that the differences between different chitosans are due to the higher protein production rather than the amount of cells which were transfected (Fig. 1c). The differences in transfection efficacy cannot be explained by the differences in the size and surface charge of polyplexes or the cellular uptake of the formulation. The missing correlation between cellular uptake of polyplexes and transgene expression (Fig. 4b) indicates that increased transfection efficacy of chitosans with DP_n30 – 40 is due to more efficient cellular processing of the delivered pDNA rather than the more efficient delivery of pDNA into the cells.

Comparing the kinetics of transgene expression for eight different formulations based on chitosan DP_n31 and DP_n88 (Fig. 2) showed that increasing the amount of chitosan above the optimal A/P lead not only to lower gene expression, but also delayed the onset of transgene production. Combining the results in Fig. 1 and 2, it is possible to hypothesize that chitosans with DP_n 30 – 40 produce polyplexes with optimal pDNA binding strength which show optimal unpacking kinetics intracellularly whereas increasing the chain length and A/P of formulation lead to tighter polyplexes which exhibit slower and less efficient pDNA release. This is supported by a recent report where polyplexes formed by high molecular weight chitosan (390 kDa) showed slow unpacking kinetics [6] as well as previously reported data showing correlation between chitosan structure and polyplex stability [28-30]. Furthermore, general correlation between transfection efficacy and heparin-induced pDNA release was found in this study (Fig. 5). Formulations not able to release pDNA after heparin treatment, such as DP_n400,

showed poor transfection efficacy. On the other hand, formulations showing premature dissociation in transfection medium such as DP_n21 at A/P < 10 showed both low cellular uptake and low transfection efficacy.

Due to the interest in glycosylated chitosan, we decided to investigate the chain length effect also in the series of trimer substituted chitosans (TCO) prepared by grafting the uncharged trisaccharide A-A-M to the linear chitosans described above. The presence of the substituent induces hindrance and weakens the affinity between pDNA and TCOs, yielding polyplexes which release pDNA more easily than the polyplexes of unsubstituted chitosans. Consequently, it may be expected that A-A-M substitution of short chitosans forming unstable complexes such as DP_n21 will reduce the transfection efficacy, whereas the substitution of long chitosans forming too stable complexes such as DP_n88 will enhance the gene delivery. Indeed, the results in Fig. 6 confirmed this assumption and further strengthen the primary role of chitosan-pDNA interaction strength in chitosan-mediated transfection. As shown in Fig. 6b,c the longer the chain and the more stable polyplexes, the stronger enhancement of the transfection efficacy after glycosylation. The same is true about the A/P ratio (Fig. 6c), the reduced stability of complexes following glycosylation may be compensated by higher amount of polymer available.

The differences in the influence of A/P ratio on transfection efficacy observed for linear (Fig. 1) and TCO chitosans (Fig. 6) further support the critical role of charge-based interactions. The nitrous acid degradation of chitosan produce polydisperse samples and the polydispersity index increases with DP_n (see Table 1). This means that at given A/P, the polyplexes are formed by mixture of chains with variable chain length. With increasing A/P ratio, increased amounts of chitosan and higher amounts of longer chains are available in the formulation, yielding more stable polyplexes. Therefore, in case of linear chitosan (Fig. 1), transfection efficiency drastically decreased above the optimal A/P ratio similarly as it does when the chain length increases. However, in case of TCOs (Fig. 6), this effect was counterweighted by hindrance

imposed by uncharged substituent and despite chain length, the polyplexes were still able to disassembly. This was confirmed in the experiment with TCO21 fractionated into narrow DP's (Fig. 7), where the transfection efficacy of the TCO with DP > 28 was 10-fold higher than the parent sample and TCO with DP below 28 were practically inefficient. Apparently, the TCO samples contain large fraction of short chains which are unable to yield competent polyplexes, necessitating the need of high A/P ratios. The importance of charge-based interactions was further emphasized in the experiment where the strength of the chitosan-pDNA interaction was controlled by the size of the substituent and the degree of substituent grafting.

The confocal laser scanning microscopy of cells transfected by polyplexes DP_n31 and DP_n88 at A/P 10 did not reveal any substantial differences in polyplex unpacking or intracellular trafficking of DP_n31 versus DP_n88 polyplexes. HEK293 cells were able to internalize large aggregates of complexes (Fig. 9) similarly as reported by Ishii et al [31], and cells transfected by DP_n88 appeared to contain larger aggregates compared to those transfected by DP_n31. CLSM was able to detect merely the large assemblies of fluorescent molecules of the entire transfected cells. FCS measurements in the nucleus and cytoplasm revealed that free chitosan was present in both compartments 1 h post incubation with complexes. We have previously shown that polyplex formulation of linear chitosan at A/P 10 contain typically about 50 % of free unbound chitosan [21] and this free chitosan also enters the cells together with polyplexes. However, HEK293 cells internalized more chitosan after incubation with polyplexes than with free chitosan. The presence of the chitosan in the cytosol and nucleus indicates that chitosan and polyplexes are able to escape lysosomal degradation and are transported to the nucleus. Even though the accumulation of slowly diffusing DP_n31 inside the cytoplasm 24 h post transfection might be attributed to a dissociation of the polyplexes in the cytoplasm, it is not clear whether the accumulation of free and bound DP_n88 in the nucleus is more likely due to a partial binding of free DP_n88 following a migration of free DP_n88 from the cytoplasm to the nucleus and/or to a

dissociation of the polyplexes in the nucleus. Therefore future FCS work should focus on the intracellular fate of pDNA rather than of chitosan.

Conclusion

A better understanding of the structure-function relationship in chitosan-mediated gene delivery is important for future design of chitosan-based delivery systems. Here we have shown that by varying the chain length of the chitosan and the degree of hindrance, it is possible to control the degree of interaction between the chitosan and its pDNA cargo in the polyplex and thereby the magnitude of the gene transfer. The gene delivery efficacy depended strongly on the valency of the chitosan and maximum transgene expression was achieved in a narrow optimal window of DP_n31 – 42. The differences between different chitosans were due to more efficient protein production rather than the amount of cells which were transfected. Increasing chain length and A/P above the optimum, both reduced and delayed the transgene expression. Furthermore, introduction of hindrance reduced or enhanced transfection efficacy, depending on the DP_n, A/P, size of the substituent, and degree of grafting. These findings provide evidence that the transfection efficacy is governed by the interaction strength between the chitosan vector and its plasmid cargo in the polyplex which determines the timing and extent of polyplex disassembly.

References

1. Issa MM, Köping-Höggård M, Artursson P. Chitosan and the mucosal delivery of biotechnology drugs. Drug Discovery Today: Technologies 2005;2(1):1-6.
2. Lee KY. Chitosan and its derivatives for gene delivery. Macromol Res 2007 Apr;15(3):195-201.
3. Dang JM, Leong KW. Natural polymers for gene delivery and tissue engineering. Adv Drug Deliv Rev 2006 Jul;58(4):487-499.
4. Strand SP, Tømmeraas K, Vårum KM, Østgaard K. Electrophoretic light scattering studies of chitosans with different degrees of N-acetylation. Biomacromolecules 2001 Win;2(4):1310-1314.
5. Filion D, Lavertu M, Buschmann MD. Ionization and solubility of chitosan solutions related to thermosensitive chitosan/glycerol-phosphate systems. Biomacromolecules 2007 Oct;8(10):3224-3234.
6. Chen HH, Ho YP, Jiang X, Mao HQ, Wang TH, Leong KW. Quantitative comparison of intracellular unpacking kinetics of polyplexes by a model constructed from quantum Dot-FRET. Molecular Therapy 2008 Feb;16(2):324-332.
7. Köping-Höggard M, Varum KM, Issa M, Danielsen S, Christensen BE, Stokke BT, et al. Improved chitosan-mediated gene delivery based on easily dissociated chitosan polyplexes of highly defined chitosan oligomers. Gene Ther 2004 Oct;11(19):1441-1452.
8. Schaffer DV, Fidelman NA, Dan N, Lauffenburger DA. Vector unpacking as a potential barrier for receptor-mediated polyplex gene delivery. Biotechnology and Bioengineering 2000 Mar;67(5):598-606.
9. Breunig M, Lungwitz U, Liebl R, Fontanari C, Klar J, Kurtz A, et al. Gene delivery with tow molecular weight linear polyethytenimines. Journal of Gene Medicine 2005 Oct;7(10):1287-1298.

10. Godbey WT, Wu KK, Mikos AG. Size matters: Molecular weight affects the efficiency of poly(ethylenimine) as a gene delivery vehicle. J Biomed Mater Res 1999 JUN 5;45(3):268-275.

11. Huang M, Fong CW, Khor E, Lim LY. Transfection efficiency of chitosan vectors: Effect of polymer molecular weight and degree of deacetylation. Journal of Controlled Release 2005 Sep;106(3):391-406.

12. Lavertu M, Methot S, Tran-Khanh N, Buschmann MD. High efficiency gene transfer using chitosan/DNA nanoparticles with specific combinations of molecular weight and degree of deacetylation. Biomaterials 2006 Sep;27(27):4815-4824.

13. MacLaughlin FC, Mumper RJ, Wang JJ, Tagliaferri JM, Gill I, Hinchcliffe M, et al. Chitosan and depolymerized chitosan oligomers as condensing carriers for in vivo plasmid delivery. Journal of Controlled Release 1998 Dec;56(1-3):259-272.

14. Kiang T, Wen H, Lim HW, Leong KW. The effect of the degree of chitosan deacetylation on the efficiency of gene transfection. Biomaterials 2004 Oct;25(22):5293-5301.

15. Köping-Höggard M, Mel'nikova YS, Vårum KM, Lindman B, Artursson P. Relationship between the physical shape and the efficiency of oligomeric chitosan as a gene delivery system in vitro and in vivo. Journal of Gene Medicine 2003 Feb;5(2):130-141.

16. Issa MM, Köping-Höggard M, Tømmeraas K, Vårum KM, Christensen BE, Strand SP, et al. Targeted gene delivery with trisaccharide-substituted chitosan oligomers in vitro and after lung administration in vivo. Journal of Controlled Release 2006 Sep;115(1):103-112.

17. Strand SP, Issa MM, Christensen BE, Vårum KM, Artursson P. Tailoring of Chitosans for Gene Delivery: Novel Self-Branched Glycosylated Chitosan Oligomers with Improved Functional Properties. Biomacromolecules 2008 Nov;9(11):3268-3276.

18. Tømmeraas K, Vårum KM, Christensen BE, Smidsrod O. Preparation and characterisation of oligosaccharides produced by nitrous acid depolymerisation of chitosans. Carbohydr Res 2001 Jul;333(2):137-144.

19. Tømmeraas K, Köping-Höggard M, Vårum KM, Christensen BE, Artursson P, Smidsrod O. Preparation and characterisation of chitosans with oligosaccharide branches. Carbohydr Res 2002 Nov;337(24):2455-2462.
20. Christensen BE, Vold IMN, Vårum KM. Chain stiffness and extension of chitosans and periodate oxidised chitosana studied by size-exclusion chromatography combined with light scattering and viscosity detectors. Carbohydrate Polymers 2008;74(3):559-565.
21. Reitan NK, Maurstad G, Davies C de L, Strand SP. Characterizing DNA Condensation by Structurally Different Chitosans of Variable Gene Transfer Efficacy. Biomacromolecules;0(0).
22. Weisshart K, Jungel V, Briddon SJ. The LSM 510 META ConfoCor 2 system: An integrated imaging and spectroscopic platform for single-molecule detection. Current Pharmaceutical Biotechnology 2004 Apr;5(2):135-154.
23. Köping-Höggard M, Tubulekas I, Guan H, Edwards K, Nilsson M, Vårum KM, et al. Chitosan as a nonviral gene delivery system. Structure-property relationships and characteristics compared with polyethylenimine in vitro and after lung administration in vivo. Gene Ther 2001 Jul;8(14):1108-1121.
24. Romoren K, Pedersen S, Smistad G, Evensen O, Thu BJ. The influence of formulation variables on in vitro transfection efficiency and physicochemical properties of chitosan-based polyplexes. Int J Pharm 2003 Aug 11;261(1-2):115-127.
25. Sato T, Ishii T, Okahata Y. In vitro gene delivery mediated by chitosan. Effect of pH, serum, and molecular mass of chitosan on the transfection efficiency. Biomaterials 2001 Aug;22(15):2075-2080.
26. Hashimoto M, Morimoto M, Saimoto H, Shigemasa Y, Sato T. Lactosylated chitosan for DNA delivery into hepatocytes: The effect of lactosylation on the physicochemical properties and intracellular trafficking of pDNA/chitosan complexes. Bioconjugate Chemistry 2006 Mar-Apr;17(2):309-316.

27. Plank C, Tang MX, Wolfe AR, Szoka FC. Branched cationic peptides for gene delivery: Role of type and number of cationic residues in formation and in vitro activity of DNA polyplexes. Hum Gene Ther 1999 Jan;10(2):319-332.

28. Danielsen S, Maurstad G, Stokke BT. DNA-polycation complexation and polyplex stability in the presence of competing polyanions. Biopolymers 2005 Feb;77(2):86-97.

29. Danielsen S, Strand S, Davies C de L, Stokke BT. Glycosaminoglycan destabilization of DNA-chitosan polyplexes for gene delivery depends on chitosan chain length and GAG properties. Biochim Biophys Acta-Gen Subj 2005 Jan;1721(1-3):44-54.

30. Strand SP, Danielsen S, Christensen BE, Vårum KM. Influence of chitosan structure on the formation and stability of DNA-chitosan polyelectrolyte complexes. Biomacromolecules 2005 Nov-Dec;6(6):3357-3366.

31. Ishii T, Okahata Y, Sato T. Mechanism of cell transfection with plasmid/chitosan complexes. Biochim Biophys Acta-Biomembr 2001 Sep;1514(1):51-64.

Paper IV

Characterization of tumor microvascular structure and permeability: comparison between MRI and intravital confocal imaging

Nina K. Reitan[1], Marte Thuen[2], Pål Erik Goa[3], Catharina de Lange Davies[1]*

[1]Department of Physics,
The Norwegian University of Science and Technology, 7491 Trondheim, Norway

[2]Department of Circulation and Medical Imaging,
The Norwegian University of Science and Technology, 7489 Trondheim, Norway

[3]Department of Radiology, St. Olavs Hospital, 7006 Trondheim, Norway

Keywords: CLSM, MRI, dorsal window chamber, permeability, vasculature

---

Manuscript in preparation.

* Corresponding author: nina.reitan@ntnu.no

Abstract

Solid tumors are characterized by abnormal organization, structure, and function of blood vessels. These abnormalities give rise to enhanced vascular permeability and may predict therapeutic response. Permeability and architecture of the microvasculature were measured in human osteosarcoma tumors growing in dorsal window chambers in mice by confocal laser scanning microscopy (CLSM) and dynamic contrast enhanced MRI (DCE-MRI). 40 kDa dextran and Gadomer were used as molecular tracers for CLSM and DCE-MRI, respectively. The volume transfer coefficient K^{trans} estimated by DCE-MRI and the extravasation rate K_i measured by CLSM were found to correlate. This demonstrates that the two techniques may give complementary information. Extravasation was related to the microvascular structure and was found to correlate with fractal dimension, vascular volume fraction, and vascular density. The vascular structural parameters were higher for the abnormal tumor vasculature than for normal vessels.

Introduction

The blood supply in tumors plays a critical role in cancer therapy. The flow rate, vascular structure, and permeability are responsible for the microenvironment characterized by hypoxia and acidosis.[1,2] The vasculature and microenvironment determine the efficacy of radiotherapy and chemotherapy, as well as drug delivery to solid tumors. Most tumors develop their vascular network by angiogenesis, and the tumor vasculature differs markedly from that of the host tissue. Tumor vasculature has abnormal structure and function characterized by complex branching patterns, tortuous and bending vessels, and heterogeneous spatial distribution. These characteristics result in high geometric resistance to blood flow, leading to both spatial and temporal heterogeneous blood flow rate.[2-5]

The heterogeneity of the tumor vasculature also includes the vessel wall. In general, the capillary wall is poorly developed with fenestrae between the endothelial cells, a discontinuous endothelial cell layer, and partly lacking basal lamina, resulting in leaky blood vessels. However, parts of the vessel wall may also resemble normal vessels, contributing to the heterogeneous vessel permeability. The high permeability favor the transcapillary transport of therapeutic macromolecules,[2,6] and delivery of novel nanomedicine such as proteins and encapsulated drugs or genes benefits from the increased permeability. Although extravasation of macromolecules in tumors may be enhanced compared to normal vessels, the macromolecules face severe problems penetrating the extracellular matrix and reaching their targets. Thus, the uptake of nanomedicine in tumor tissue is low and the therapeutic macromolecules are heterogeneous distributed.[7,8] The vascular permeability is shown to depend on the tumor type as well as the molecular weight and charge of the molecular tracer.[9-11] Structural parameters, such as vascular density and fractal dimension, can be used to characterize complexity of tumor vasculature.[12,13] Fractal dimension describes irregularly tortuous contours and branching structures which are characteristic for tumor microvasculature, and it has been shown that the fractal dimension calculated by the box-counting method is higher for tumors than for normal microvasculature.[14,15]

The crucial effect of the vasculature on the microenvironment and cancer therapy illustrates the need for methods to study the vascular structure and permeability. MRI is a non-invasive imaging technique commonly used to study the structure and function of the vasculature.[16-18] Tracer kinetic analysis of contrast-enhanced images allows estimation of physiological parameters such as blood volume, blood flow and vessel permeability.[19] However, MRI does not have sufficient spatial resolution to visualize cellular and subcellular structures. Intravital optical microscopy using confocal laser scanning or two-photon microscopy has superior spatial resolution, and several cellular and extracellular characteristics can be imaged simultaneously and colocalized in three dimensions.[20,21]

The purpose of the present work was to compare vascular parameters obtained with confocal laser scanning microscopy (CLSM) and dynamic contrast enhanced MRI (DCE-MRI) to investigate how these techniques may complement each other. The heterogeneous tumor microvascularity caused by inadequate blood perfusion[22] induces a high degree of uncertainty in the quantification of structural and transport parameters. The uncertainty can be reduced by validation and cross-comparison of results obtained by the two imaging techniques. The dorsal window chamber allows direct examination of in vivo tumor angiogenesis and microcirculation over several days. Tumors were grown in dorsal window chambers in athymic mice, and microvasculature and permeability to 40 kDa dextran and Gadomer were studied by CLSM and DCE-MRI, respectively.

Materials and methods

Animals and tumor model. Dorsal window chambers in MRI-compatible material (POM: poloxy methylene) were produced. The total weight of the camber including the window was 2.0 gram. The chambers were implanted on the back of 7 – 9 weeks old, athymic female BALB/c nu/nu mice with 23 – 25 gram of weight (Taconic, M&M, Denmark) as described previously.[21] 24 h after the implantation of the chamber, the

cover slip was removed and 1.5×10^6 human osteosarcoma cells from the cell line OHS[23] were placed into the center of the chamber. A new glass cover slip was placed above and the chamber was closed. The xenografts were allowed to grow for two weeks before starting the experiments. All surgical procedures were performed under sterile conditions. During this period the animals were given 64 mg/kg/day Baytril (Enrofloxacin) in drinking water containing 2% sucrose. At the time of the experiments, the tumors were approximately 0.5 mm thick and filled the whole window area. The mice were anesthetized by subcutaneous injection of Fentanyl/Midazolam/Haldol/sterile water (3:3:2:4) at 12 ml/kg body weight (Hameln Pharmaceuticals, Germany, Alpharma AS, Norway, and Janssen-Cilag AS, Norway) and the tail vein was cannulated to allow injection of molecular tracers. The animals were kept under pathogen-free conditions at a constant temperature 19 - 22 °C, humidity 50 - 60%, 65 air changes an hour, and were allowed food and water *ad libitum*. All animal experiments have been carried out with ethical committee approval. Mice with dorsal window chambers but without tumors implanted were used to study normal tissue. A total of 16 mice were included in the experiments. One mouse was used for high resolution MR imaging of blood vessels, the others were used for CLSM and DCE-MRI. Some measurements were rejected because of image artifacts.

Tracers. The MRI contrast agent Gadomer (Bayer Schering Pharma AG, Berlin, Germany) was kindly provided by Dr. Hans Bauer. Gadomer contains 24 Gd ions at the surface of a dendritic backbone and has a molecular weight of about 17 kDa. However, due to its globular shape the apparent molecular weight is about 30 - 35 kDa. Gadomer has low toxicity and is mainly eliminated by glomerular filtration.[24] It is large enough to insure slow diffusion through the vascular wall.[25] For the CLSM time series, 40 kDa TMR(tetramethylrhodamine)-dextran (Sigma-Aldrich, St. Louis, MO) was used as a fluorescent macromolecule as this molecule has approximately the same molecular weight as Gadomer. TMR is photostable and suitable for dynamic imaging. 2MDa FITC(fluorescein isothiocyanate)-dextran (Sigma-Aldrich, St. Louis, MO) was used as a blood pool marker.

Confocal laser scanning microscopy

Experimental setup. The animal was anesthetized and an overview image of the tissue was obtained using a stereomicroscope (Motic SMZ-168 Stereo Zoom Microscope, Motic Deutschland GmbH, Germany). The tail vein was cannulated and 100 μl of 20 mg/ml 2 MDa FITC-dextran was injected to visualize the vascular structure. The cannula was flushed with 250 U/ml heparin (Sigma Chemical CO, St. Louis, MO) to avoid blood clotting. The animal was placed on the stage of the microscope (LSM Meta 510, Zeiss, Jena, Germany). The body temperature was kept at 37 °C. Images with a field of view of 460.7 $\times$ 460.7 μm^2 and 512 $\times$ 512 pixel resolution (pixel size 0.9 $\times$ 0.9 μm^2) were acquired with a Plan-Neofluar $20\times/0.5$ objective. Z-stacks of the blood vessels were acquired using a 488 nm laser, a BP500-550 nm filter in front of the detector, and a pinhole diameter of 94 μm. Extravasation of 40 kDa TMR-dextran was measured in three regions of interest (ROI) in each tumor. Background images before injection and time series after injection of 40 kDa dextran were acquired in each ROI using the 543 laser, an LP560 filter in front of the detector, and a pinhole diameter of 86 μm. 100 μl of 30 mg/ml 40 kDa TMR-dextran was then injected and images of the ROIs were successively acquired during a time period up to 60 min.

Image post-processing and data analysis. To minimize contributions to the signal from other sources than the molecular tracer, the background image taken before injection of 40 kDa dextran was subtracted from the time series acquired post injection. Intra- and extravascular image analysis were performed by applying motion-corrected vascular masks to the time series. Contours of the blood vessels were manually traced in Adobe Photoshop CS (Adobe Systems Inc, San Jose, CA). The extravascular area in the ROI was defined as all space more than 4 μm from the blood vessel walls. By visual inspection, the distance of 4 μm was considered sufficient to avoid fluorescence contribution from the intravascular area. Intensity as a function of time was measured for both intra- and extravascular areas using the ImageJ (version 1.38, available from NIH, http://rsb.info.nih.gov/ij/) plug-in *Time Series Analyzer.*

The apparent permeability of the vasculature was calculated using the method described by Patlak *et al*.[26] This method is based on plots of the ratio of extravascular to intravascular concentration of the tracer against a modified time axis (Patlak plot). We assumed that the concentration was proportional to the fluorescence intensity. The values along the ordinate axis are given by

$$y = \frac{C_t(t)}{C_{vess}(t)} \tag{1}$$

where $C_t(t)$ and $C_{vess}(t)$ are the extra- and intravascular concentrations at time *t*. The modified time axis is defined by

$$T = \frac{\int C_{vess}(t)\,dt}{C_{vess}(t)} \tag{2}$$

When there is a net irreversible accumulation of fluorescence in the tissue over the time course of the experiment, the plot becomes linear after equilibrium is reached. The terminal slope of the straight line is equal to the rate constant describing the net irreversible transport of the fluorescent tracer from the capillaries to the extravascular space. An exponential function

$$f(T) = (\alpha + \beta T)\left(1 - e^{-\lambda T}\right) \tag{3}$$

which increases linearly with T when T is large, was fitted to the extravascular/intravascular intensity ratio plotted as a function of *T*. The slope β of the straight line was used as an estimate of the extravasation rate K_i.[27] In order not to violate the requirement of a net irreversible accumulation, only the first 35 minutes of the measurements were plotted.

K_i is related to the apparent vascular permeability P by

$$K_i = P\frac{S}{V} \tag{4}$$

where S is the vascular surface area contained in the imaged tissue volume V.

The extravasation rate was also estimated by the initial rate of accumulated fluorescence in the extravascular space. The fluorescence intensity in the extravascular space normalized to the maximum intensity was plotted versus time. For plots that did not reach a maximum during the measurement time, the maximum intensity was estimated by extrapolation of the experimental data. The initial slope of the fluorescence intensity-time plots was defined as the extravasation rate and obtained by linear regression to the initial linear increase in the intensity.

Analysis of microvascular structure was based on binary images of the vascular masks. Fractal dimension D was determined using *Fractal Box Count* in ImageJ, which counts the number of boxes of an increasing size needed to cover a one pixel binary object boundary. D is calculated from the slope (D = -slope) of a log-log plot of the box size and the number of boxes necessary to cover the boundary. The method was verified by comparing measured fractal dimensions of known fractals to theoretical values, which were found to be in good agreement. Fractal theory and its relevance for vascular networks are previously described.[12,13]

Vascular branching and length, diameter, and volume of each blood vessel in the imaged ROIs were estimated using the software Amira (Visage Imaging GmbH, Germany) after tracing the blood vessels with the filament editor. The number of branching points, also called the fork density[12] (FD), is an estimate of the number of neo-formed vessels and was defined as the number of nodes in the filament traced vessels in the image. The vascular density fraction (VD) was calculated as the area of the image covered by vessels per total area.[12] The surface area (S) was calculated as the sum of the surface areas of all vessels in the ROI. Because the diameter of most vessels was wider than the detected optical section (4.5 μm), the shape of a blood vessel was approximated as a rectangular prism instead of a cylinder.

MRI

Experimental setup. MRI was performed at 7T using a Bruker Biospec Avance 70/20 (Bruker Biospin, Ettlingen, Germany) with a 72-mm volume coil for transmission and an actively decoupled quadrature rat head surface coil for receive only. The animals were anesthetized and cannulated and placed prone in the magnet on a dedicated animal bed with the chamber positioned in the isocenter. The body temperature was kept at 37 - 38 °C with circulating water within the animal bed. Pilot scans were applied to localize the appropriate tissue within the chamber, and to perfectly align the slice plane with the chamber.

For DCE-MRI a T1-map was obtained using a spin echo Rare (RareVTR) sequence with TR = 150, 600, 1200, 3000, 10000 ms, and TE = 12.5 ms. The image resolution was 578 × 578 μm^2, the slice thickness 0.3 mm, and the acquisition time 7 min 58 s. The dynamic series was acquired using a T1-weigthed spin echo Rare sequence with TR = 200 ms, TE = 7 ms, 2 averages. The field of view was 37 × 37 mm^2 with 64 × 64 pixel resolution (pixel size 578 × 578 μm^2) and 350 repetitions were used. The time resolution was 6.4 s, with a total acquisition time of 37 min 20 s. 0.2 mmol/kg Gadomer was injected during the 9th repetition, over a period of 10 s.

For imaging of blood vessels, 0.2 ml 20 mg/ml AlbuminGd-DTPA (~ 92 kDa) was injected. AlbuminGd-DTPA was synthesized in our lab based on a procedure originally described by Ogan.[28] A T1-weighted 3D Flash (fast low flip angle shot) sequence was applied with TR = 15 ms, TE = 2.4 ms, and flip angle = 25.0 deg. The voxel size was 145 × 145 × 144 μm^3 and the acquisition time was 16.38 min.

Data analysis. T1-values and the DCE-MRI data were analyzed using in-house software written in MatlabR2007b (MathWorks Inc, MA). T1 was estimated using least-squares fitting of the multi-TR recording to the standard spin-echo signal equation. A two-compartment kinetic model[19] was fitted to the concentration curves. Tofts model assumes that the tissue consists of a plasma compartment and an extravascular

extracellular space (EES), and that the rate constants k_{pe} (transfer rate from blood to EES) and k_{ep} (transfer rate from EES to blood) are identical.

The concentration $C_p(t)$ at time t of the contrast agent in the plasma compartment is determined by

$$C_p(t) = A_0\left(a_1 e^{-\alpha_1 t} + a_2 e^{-\alpha_2 t}\right) \tag{5}$$

where A_0 is the intravenously administered dose of the contrast agent. The arterial input function constants were previously estimated to a_1 = 6.427 kg/l, a_2 = 2.392 kg/l, α_1 = 0.2270 min^{-1}, and α_2 = 0.0258 min^{-1} from Gadomer plasma decay for nude mice reported by Verhoye *et al*.[30]

The total tissue concentration $C_t(t)$ of the contrast agent as a function of time is given by

$$C_t(t) = v_p \times \left(a_1 e^{-\alpha_1 t} + a_2 e^{-\alpha_2 t}\right) + K^{trans} \times \left[\frac{a_1}{K^{trans}/v_e - \alpha_1} e^{-\alpha_1 t} + \frac{a_2}{K^{trans}/v_e - \alpha_2} e^{-\alpha_2 t} + \left(\frac{a_1}{K^{trans}/v_e - \alpha_1} + \frac{a_2}{K^{trans}/v_e - \alpha_2}\right)\right] e^{\left(-K^{trans}/v_e\right)t} \tag{6}$$

where v_p is the plasma volume fraction, v_e is the EES volume fraction, and $K^{trans} = k_{ep} v_e$ is the volume transfer constant between plasma and EES.

The ROI was defined from post-contrast images as the volume in the chamber window where signal enhancement was detected. Gadomer is not assumed to enter the cells and the extravascular compartment therefore equals EES. The Gadomer relaxivity at 7T was set to 7 mM^{-1} s^{-1} (personal communication, Bayer Schering Pharma AG, Berlin, Germany, March 2009). The volume transfer constant K^{trans} was estimated by least-squares fitting with Eq. (6) to the concentration curves. Under permeability-limited conditions, K^{trans} equals the permeability surface area product per unit volume of tissue.[19] Accumulation in the tissue was estimated by the time-to-peak (*TTP*), i.e. the time from injection of Gadomer until the concentration-time curve reaches its maximum.

Statistics

A two-sample, two-tailed Student's T-test (Minitab, Minitab Inc., State College, PA) assuming non-equal variances was used to perform statistical comparison of normal and tumor data with a significance criterion of $P \leq 0.05$. Correlation was investigated by comparing parameter values obtained for a given animal with other parameters obtained for the same animal. For CLSM, these values were the mean of 1 - 3 measurements at different ROIs in the animal. For DCE-MRI, only one ROI per animal was analyzed. The parameter values were plotted and correlation was estimated by applying linear regression. The goodness of linear fit was estimated by the coefficient of determination R^2 and correlation was established with a significance criterion of $P \leq 0.05$.

Results

Vascular permeability

Extravasation of 40 kDa dextran and Gadomer in OHS tumors and normal tissue was monitored by acquiring time series of CLSM and DCE-MRI images, respectively, of the same animal on two subsequent days. Three localizations in the tissue were successively imaged by CLSM for a time period up to 60 min after injection of dextran. The dextran molecules were quickly distributed in the vasculature (Fig. 1A) and extravasated from the blood vessels to the extravascular space, as detected by enhancement of fluorescence intensity in the extravascular area (Fig. 1B and C) with time. Pre- (Fig. 1D) and post-contrast (Fig 1E and F) DCE-MRI were acquired for the whole chamber window. At time 5 min post-contrast (Fig. 1E), signal enhancement due to accumulation of Gadomer in the tissue was observed. By the end of the experiment the signal intensity was almost back to pre-contrast level (Fig. 1F).

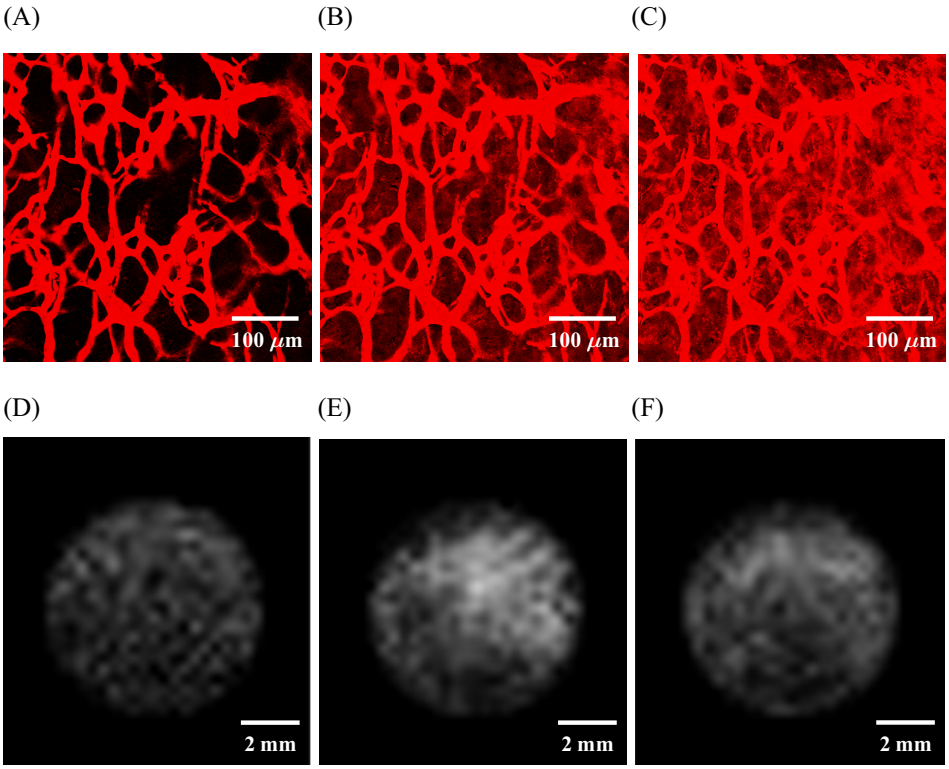

Figure 1. Dynamic time series of OHS tumor in a dorsal window chamber in mice, acquired by CLSM (A-C) and DCE-MRI (D-F). CLSM images acquired at t = 2 min (A), t = 9 min (B), and t = 25 min (C) after injection show fluorescence intensity enhancement due to extravasation of the 40 kDa TMR-dextran from the blood vessels and accumulation in the extravascular space. Images from DCE-MRI time-series at pre-contrast (D), t = 5 min (E) and t = 37 min (F) after injection of Gadomer show accumulation of the contrast agent in the tumor tissue. The pixel size was 0.9×0.9 μm^2 and 578×578 μm^2 for CLSM and DCE-MRI, respectively.

For CLSM images, the total field of view (460.7×460.7 μm^2) was used as ROI. Segmentation of the blood vessels allowed analysis of fluorescence intensity with time for both the intra- and the extravascular space in the ROIs. During the time course of the experiment, the intensity signal in the extravascular space increased with time, generally reached its maximum, and then slowly decreased again (data not shown). The intravascular concentration showed a rapid increase in intensity due to distribution of the tracer in the vasculature, followed by a gradual decrease due to clearance and

extravasation of the tracer out of the blood vessels. The ratio of the intra- and extravascular intensity were plotted against a modified time axis in a Patlak plot (Fig 2A) and the terminal slope of the fit was used as an indicator of permeability.[27] For a time course of 35 min a straight line was generally well fitted to the terminal slope, and the estimated extravasation rate *Ki* was significantly different for tumor and normal tissue. However, the terminal slope for normal tissue was negative (data not shown) and normal tissue was therefore excluded from further analysis. The apparent permeability *P* describes extravasation rate per vessel surface area. The initial slope of the fluorescence intensity-time curves was also used as an estimator of vascular permeability (Fig. 2B). All relevant mean values and standard deviations are listed in Table 1.

Kinetic parameters were estimated from the DCE-MRI data by fitting Tofts model to the Gadomer concentration-time curves in pre-defined volume ROIs. The mean T1 for all tumors was used as input into the Tofts model. The volume transfer constant K^{trans} describes apparent permeability, and tumor uptake was estimated by the time-to-peak (*TTP*) post-contrast. All mean values are listed in Table 1. Differences between normal and tumor tissue could not be detected by DCE-MRI. A typical tissue concentration-time curve is shown in Fig. 2C. Gadomer extravasated from the blood vessels into the tissue, and the concentration-time curves consisted of combined clearance and accumulation of the contrast agent in the tumor tissue. The concentration of Gadomer increased and reached a maximum after 6.2 min (*TTP*) on average, and then subsequent decreased due to clearance from both plasma and the extravascular space.

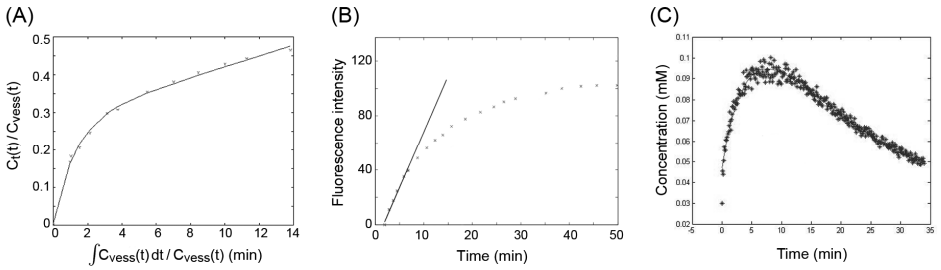

Figure 2. Different models for estimating apparent permeability. (A) Patlak-plot and (B) estimate of initial slope from CLSM time-series of 40 kDa dextran fluorescence intensity. (C) Tofts model fitted to DCE-MRI curve showing concentration versus time after injection of Gadomer.

Microvascular structure

Structural parameters, including vascular density (*VD*), vascular volume fraction (*VVF*), fork density (*FD*), and fractal dimension (*D*), was quantified from CLSM images based on binary images and filament traces of masked blood vessels. There was a striking difference between the tortuous tumor vessels (Fig. 3A) and the well organized normal blood vessels (Fig. 3B). To obtain high spatial resolution of the MR images of the blood vessels, a longer acquisition time was required and a larger intravascular contrast agent (AlbuminGd-DTPA) was therefore used. Larger blood vessels were clearly visualized (Fig. 3C).

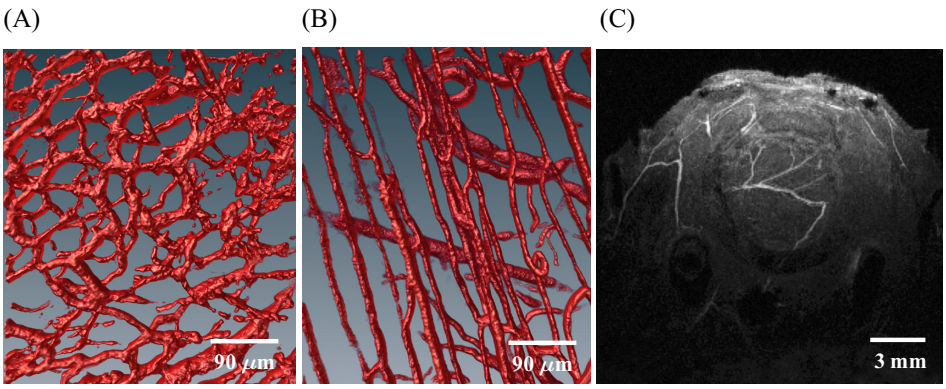

Figure 3. Blood vessels in a dorsal window chamber imaged by CLSM (A,B) and MRI (C). (A) Abnormal, tortuous OHS tumor vessels and (B) well-organized normal vessels visualized in Amira by 3D volume rendering of CLSM z-stacks of tissue after injection of 2 MDa FITC-dextran. (C) Maximum intensity projection of MRI FLASH 3D sequence for imaging of blood vessels. AlbuminGd-DTPA was used as an MRI contrast agent.

Correlation of vascular structural and functional parameters measured by CLSM and DCE-MRI

The structural parameters and permeability estimated by CLSM and DCE-MRI were plotted and compared, and linear regression was applied to the data (Fig. 4). A high degree of positive correlation ($P < 0.001$) was found between all structural vascular parameters, demonstrating a linear relationship between fractal dimension (*D*), vascular density (*VD*), fork density (*FD*), and vascular volume fraction (*VVF*). These structural parameters were significantly higher in tumors than in normal tissue, which can be observed from the two distinct populations in Fig. 4A-C. Extravasation measured by CLSM and represented by the extravasation rate *Ki* correlated ($P \leq 0.02$) with microvascular structure (Fig 4D-F). K^{trans} estimated from DCE-MRI was shown to correlate ($P \leq 0.05$) with K_i and the initial slope of the extravascular fluorescence intensity-time curves, which were both used to estimate vascular extravasation (Fig. 4G and I). However, no correlation was found between K^{trans} and apparent permeability *P* which relates K_i to the vascular surface area. *TTP* represents the tissue uptake of Gadomer and was calculated from the DCE-MRI concentration-time curves. *TTP* was shown to correlate well with the initial slope of the extravascular fluorescence intensity curves (Fig. 4J), demonstrating similar accumulation kinetics for the two tracers.

Mean values and standard deviations of all measurements in tumor and normal tissue are listed in Table 1, whereas the plots in Fig. 4 show mean values calculated from 1 – 3 measurements at different locations in the tissue of each mouse. For the DCE-MRI data, only one ROI per animal was analyzed due to limited signal-to-noise ratio (SNR). The vascular structure demonstrated a high degree of heterogeneity within the same tumors, as indicated by large standard deviations in Fig. 4. Especially the extravasation rate showed large variations at the three measured locations, with the highest coefficient of variation (standard deviation/mean) of 2.43 for an animal, and the heterogeneity was larger within a tumor than between different mice (0.42) as estimated by the coefficients of variation.

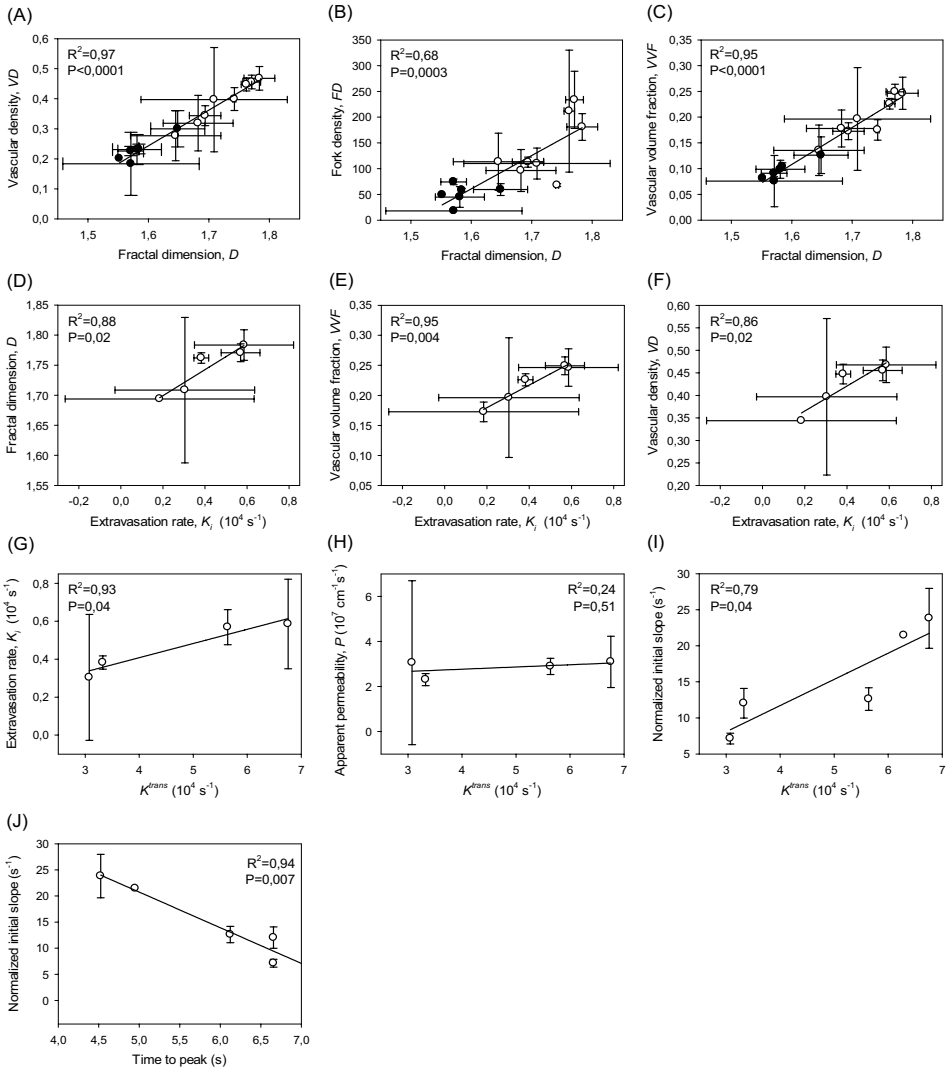

Figure 4. Correlation between vascular structural parameters and permeability obtained with CLSM and DCE-MRI. Microvascular structure: fractal dimension *D*, vascular density *VD*, fork density *FD*, and vascular volume *VVF* was measured by CLSM for normal (●) and tumor tissue (○). Permeability parameters measured by CLSM (extravasation rate K_i, apparent permeability *P*, and initial slope) and DCE-MRI (K^{trans} and time-to-peak *TTP* post-contrast) were plotted for tumor tissue. (A-C): Fractal dimension *D* plotted against structural parameters. (D-F): Permeability represented by the extravasation rate K_i versus structural parameters. (G-I) K^{trans} obtained from DCE-MRI versus permeability parameters measured by CLSM. (J): *TTP* in DCE-MRI concentration-time curves versus the initial slope in CLSM intensity curves. Mean values and standard deviations are based on measurements in 1 – 3 ROIs. The goodness of linear fit R^2 and the P-values are given in each plot.

Table 1. Estimates of permeability and microvasculature parameters in tumor and normal tissue in dorsal skinfold chambers.*

CLSM parameters	**Tumor**	**Normal**
Fractal dimension *D*	1.72 ± 0.06	1.59 ± 0.05
Vascular density *VD*	0.38 ± 0.09	0.24 ± 0.06
Fork density *FD*	144.0 ± 72.8	52.7 ± 20.3
Vascular volume fraction *VVF*	0.20 ± 0.05	0.10 ± 0.03
S/V (cm^{-1})	151.38 ± 40.92	95.70 ± 25.88
Normalized initial slope (s^{-1})	15.4 ± 2.13	15.2 ± 2.58
Extravasation rate K_i ($10^4 s^{-1}$)	0.42 ± 0.27	**
Apparent permeability P ($10^7 cm^{-1}s^{-1}$)	2.58 ± 1.95	**
DCE-MRI parameters	**Tumor**	**Normal**
Volume transfer constant K^{trans} ($10^4 s^{-1}$)	5.02 ± 1.71	8.28 ± 3.32
EES volume fraction v_e	0.20 ± 0.04	0.20 ± 0.06
Time-to-peak *TTP* (s)	6.23 ± 1.28	6.55 ± 1.63

* CLSM parameters are represented by mean values and standard deviations based on 4 – 9 mice and 1 – 3 measurements per mice. The mean DCE-MRI parameters are based on one measurement in each of 5 mice.

** The curves showed clear difference between tumor and normal tissue, but the numbers for normal tissue were excluded because of a negative terminal slope in the Patlak plots.

Discussion

Tumor tissue is often characterized by abnormal microvascular structure and increased vascular permeability. These properties may predict therapeutic response. Robust methods are therefore required for quantifying the structural and functional parameters in tumor tissue. In the present study correlation between microvascular structure and permeability was found in OHS tumor tissue growing in dorsal window chambers imaged by CLSM and DCE-MRI. Few previous studies have directly related permeability of tumor vessels to its microvascular structure by applying these techniques in combination.[31]

MRI provides non-invasive images of vasculature and is a technique of clinical importance in diagnosis and in monitoring therapeutic outcome. However, the spatial resolution in MRI is limited and confocal imaging provides an opportunity to obtain detailed information about microvasculature which is not accessible with MRI. In the present study, larger vessels were clearly observed using MRI whereas small capillaries and their branching pattern were visualized using CLSM. CLSM thus provide more detailed information about local variations than MRI.

Choice of molecular tracers

Gadomer was chosen as an MRI contrast agent because it is biocompatible, has previously been shown to provide information about vascular permeability,[18,30,32,33] and has a suitable size for the present experiments. Gadomer could not be fluorescently labeled because all amines were occupied by Gd. A similar-sized, well-characterized dextran was therefore chosen as a fluorescent counterpart to Gadomer. Multi-modal macromolecular contrast agents, e.g. AlbuminGD-DTPA, were considered but they are generally larger than requested in this study.

Dextrans have previously been used to study permeability in tumors growing in dorsal window chambers. Dreher *et al*. used dextrans of various molecular weights (3.3 kDa – 2 MDa) and showed that accumulation was maximal for dextrans with molecular weights between 40 and 70 kDa,[9] indicating that the enhanced permeability effect is relevant for the chosen molecular tracers in the present study. 40 kDa dextran has also previously been used to characterize permeability of the capillaries in tumors growing in dorsal window chambers.[27]

Permeability estimated by CLSM and DCE-MRI

Permeability of 40 kDa dextran was measured by acquiring CLSM time series. Measurements were performed in three different ROIs for each animal. All extravascular fluorescence-intensity curves showed an initial increase before the

intensity stabilized and occasionally decreased, probably due to reabsorbance into the vascular space or oozing out of the tumor due to the outward connective gradient. There were large variations in the time development and the maximum value of the intensity, both within a given tumor and between different animals, demonstrating a heterogeneous permeability. The spatial heterogeneity of extravasation in tumors is well known and is due to heterogeneous blood supply and anatomic variations of the tumor vessels.[22,34,35] The correlation between functional and anatomic heterogeneity has been demonstrated by Dvorak *et al*., who showed that different types of vessels exhibit different degree of leakiness.[35]

Permeability of Gadomer was estimated from DCE-MRI measurements. The time development of the concentration curves obtained in the present study was consistent with previously found contrast uptake curves of Gadomer.[30] The steep initial slope indicates high vascular permeability. The fast initial decay of the curves indicates that Gadomer is being efficiently cleared from plasma by glomerular filtration, resulting in a low concentration of Gadomer in the tissue, which is consistent with a low maximum value of the concentration curve.

For kinetic analysis of the CLSM images, the method developed by Patlak *et al*.[26] was chosen, whereas the DCE-MR images were analyzed by the well established two-compartment kinetic model developed by Toft *et al*.[19] Previously measured arterial input constants[30] provided acceptable fit to the present DCE-MRI data. The Patlak method used to analyze CLSM data is based on the measured fluorescence intensity values, and does not require various input parameters such as the arterial input function. The method also avoids the use of complex pharmacokinetic modeling. Clear differences between normal and tumor tissue were observed for permeability estimated by the Patlak model. A negative terminal slope was observed in the Patlak plots for normal tissue, which indicates a rapid elimination of the tracer in the interstitium. No significant differences between tumors and normal tissue were detected from the DCE-MRI data using the Tofts model.

The fact that CLSM could discriminate between tumor and normal tissue, whereas DCE-MRI could not, may be explained by differences in the methods, data analysis, and/or molecular tracers. Whereas dextran has a linear molecular structure and is neutral, Gadomer is globular and negatively charged. Permeability has previously been shown to depend on both molecular structure and charge.[10,16] The image resolution used with CLSM (0.9×0.9 μm^2) was superior to that of DCE-MRI (578×578 μm^2). Furthermore, the tissue in the dorsal window chamber was thin (~ 0.5 mm for tumors, $<$ 0.5 mm for normal tissue). The SNR in images acquired with DCE-MRI was therefore low, and to maximize the SNR we chose to use the whole volume with detectable signal enhancement as ROI. The smaller ROIs used in CLSM ($\sim 0.5 \times 0.5$ mm^2) may have been better suited to resolve the differences between tumors and normal tissue. The large ROIs used in DCE-MRI analysis may also have included normal vessels and thereby underestimated tumor permeability. To use smaller ROIs for analyzing DCE-MRI data, e.g. pixel-based DCE-MRI, would be desirable but requires a higher SNR.

Correlation between CLSM and DCE-MRI

The positive correlation obtained between K^{trans} of Gadomer measured by DCE-MRI and the extravasation rate K_i of the 40 kDa dextran measured by CLSM demonstrated that extravasation measured by the two methods reflected each other even though different molecules and different mathematical models were used. K_i indicates the degree of accumulation of the tracer in the extravascular space, and is dependent on the available vasculature in the ROI. Therefore the apparent permeability per vascular surface area P was calculated by estimating the total vascular surface area in the tissue volume (S/V). However, P did not correlate with structural parameters (data not shown) or with K^{trans} (Fig. 4H). This was unexpected and may be because S/V was not well-defined in the optical section, as the optical section was thinner than the diameters of most vessels. In another study of extravasation of 40 kDa dextran in tumors using the dorsal window chamber model, Reyes-Aldasoro *et al*. analyzed 3D multi-photon images with the Patlak Model.[27] 3D images of one ROI may provide a more well-defined vascular surface area. However, in the present work we aimed to study the

heterogeneity within the vasculature by measuring three different ROIs. The time series required a high time resolution due to relatively fast extravasation, and we therefore chose to apply 2D imaging of several ROIs instead of 3D acquisition of one ROI.

Quantitative data for permeability was not the main focus of the present work and would have required thoroughly calibration of e.g. concentration versus intensity. We rather focused on relating information obtained from different techniques and analysis. Permeability was therefore also estimated from CLSM images by extracting the initial slope of the extravascular fluorescence intensity curve. There was a significant correlation between permeability estimated by the initial slope and the DCE-MRI parameters K^{trans} and *TTP*. This indicates that a variety of relevant parameters may be applied in complementary CLSM and MRI analysis.

The relation between microvascular structure and permeability

Enhanced permeability in tumors is related to structural characteristics. The CLSM images revealed several structural parameters which were found to correlate with each other and with the estimated extravasation of dextran. Also, significant differences were found between the microvascular structure of tumors and normal tissue.

Fractal analysis provides an overall mathematical description of the vascular network, and may reflect the degree of vascular tortuousity or self-similarity. The formation of new blood vessels in a tumor by angiogenesis is essential for tumor growth and metastasis, and the fractal dimension has been shown to yield information about vascular architecture, tumor growth and angiogenesis.[13] The fractal dimension in the present study was 1.1 times higher for tumor vessels than for normal vessels. The same ratio between tumor and normal vessels was found by Gazit *et al*., although their fractal dimensions were somewhat higher (1.88 for tumors and 1.70 for normal arteriovenous vascular network).[15] However, they determined the fractal dimension for normal capillaries to 1.99. The fractal dimension for normal tissue (1.59) calculated in the present study indicates that the investigated vasculature contained various vessel types

and not only capillaries. The mean fractal dimensions correlated positively with extravasation rate, vascular density, fork density, and vascular volume fraction, which all may be potential indicators of angiogenetic activity.

Vascular parameters such as microvessel density and permability may be prognostic factors, and has been shown to predict outcome in patients with breast, colon, and lung cancer.[36-40] Anti-angiogenic therapy blocking the vascular endothelial growth factor (VEGF) or its receptor (VEGFR2) is reported to induce apoptosis in the endothelial cells and decrease the vessel diameter, density, and permeability[41,42]. These changes were accompanied by the development of a normal phenotype of the vessel structure, and this normalization of the vascular structure resulted in decreased interstitial fluid pressure and a more normal microenvironment. The normalization of the vasculature and the reduced interstitial fluid pressure may facilitate drug delivery. There is a need to find reliable biomarkers reflecting the vascular structure and thereby the prognostic outcome. Vascular permeability may be such a marker, and K^{trans} is reported to be uniquely suited to evaluate the normalization process in tumor vasculature.[43]. The present work demonstrates that MRI and CLSM may be useful complementary methods in the characterization of permeability.

Conclusion

By combining CLSM and DCE-MRI we measured permeability and microvascular architecture in tumors growing in dorsal window chambers in mice. A correlation was found between permeability parameters estimated by the two techniques. Permeability was further shown to depend on structural parameters, like fractal dimension, vascular volume fraction, and vascular density. We have demonstrated that the dorsal window tumor model gives a unique opportunity to use CLSM and MRI as complementary techniques. CLSM can both validate results obtained with MRI and provide insight into the spatial heterogeneous microenvironment on a microscopic level which is not accessible with MRI.

References

(1) Vaupel, P.; Mayer, A. *Transfus Clin Biol*, **2005**, *12*, 5-10.

(2) Fukumura, D.; Jain, R. K. *J Cell Biochem*, **2007**, *101*, 937-949.

(3) Jain, R. K. *Cancer Res*, **1988**, *48*, 2641-2658.

(4) Less, J. R.; Skalak, T. C.; Sevick, E. M.; Jain, R. K. *Cancer Res*, **1991**, *51*, 265-273.

(5) Leunig, M.; Yuan, F.; Menger, M. D.; Boucher, Y.; Goetz, A. E.; Messmer, K.; Jain, R. K. *Cancer Res*, **1992**, *52*, 6553-6560.

(6) Yuan, F. *Sem Radiat Oncol*, **1998**, *8*, 164-175.

(7) Eikenes, L.; Bruland, Ø. S.; Brekken, C.; Davies, C. de L. *Cancer Res*, **2004**, *64*, 4768-4773.

(8) Eikenes, L.; Tari, M.; Tufto, I.; Bruland, Ø. S.; Davies, C. de L. *Br J Cancer*, **2005**, *93*, 81-88.

(9) Dreher, M. R.; Liu, W. G.; Michelich, C. R.; Dewhirst, M. W.; Yuan, F.; Chilkoti, A. *J Natl Cancer Inst*, **2006**, *98*, 335-344.

(10) Dellian, M.; Yuan, F.; Trubetskoy, V. S.; Torchilin, V. P.; Jain, R. K. *Br J Cancer*, **2000**, *82*, 1513-1518.

(11) Farma, J. M.; Puhlmann, M.; Soriano, P. A.; Cox, D.; Paciotti, G. F.; Tamarkin, L.; Alexander, H. R. *Int J Cancer*, **2007**, *120*, 2474-2480.

(12) Mancardi, D.; Varetto, G.; Bucci, E.; Maniero, F.; Guiot, C. *Theor Biol Med Mod*, **2008**, *5*,

(13) Baish, J. W.; Jain, R. K. *Cancer Res*, **2000**, *60*, 3683-3688.

(14) Sabo, E.; Boltenko, A.; Sova, Y.; Stein, A.; Kleinhaus, S.; Resnick, M. B. *Clin Canc Res*, **2001**, *7*, 533-537.

(15) Gazit, Y.; Berk, D. A.; Leunig, M.; Baxter, L. T.; Jain, R. K. *Phys Rev Lett*, **1995**, *75*, 2428-2431.

(16) Roberts, H. C.; Saeed, M.; Roberts, T. P. L.; Mühler, A.; Shames, D. M.; Mann, J. S.; Stiskal, M.; Demsar, F.; Brasch, R. C. *J Magn Reson Imaging*, **1997**, *7*, 331-338.

(17) Ewing, J. R.; Brown, S. L.; Lu, M.; Panda, S.; Ding, G.; Knight, R. A.; Cao, Y.; Jiang, Q.; Nagaraja, T. N.; Churchman, J. L.; Fenstermacher, J. D. *J Cereb Blood Flow Metab*, **2006**, *26*, 310-320.

(18) Verhoye, M.; van der Sanden, B. P. J.; Rijken, P. F. J. W.; Peters, H. P. W.; Van der Kogel, A. J.; Pee, G.; Vanhoutte, G.; Heerschap, A.; Van der Linden, A. *Magn Reson Med*, **2002**, *47*, 305-313.

(19) Tofts, P. S.; Brix, G.; Buckley, D. L.; Evelhoch, J. L.; Henderson, E.; Knopp, M. V.; Larsson, H. B. W.; Lee, T.-Y.; Mayr, N. A.; Parker, G. J. M.; Port, R. E.; Taylor, J.; Weisskoff, R. M. *J Magn Reson Imaging*, **1999**, *10*, 223-232.

(20) Weissleder, R.; Pittet, M. J. *Nature*, **2008**, *452*, 580-589.

(21) Erikson, A.; Tufto, I.; Bjønnum, A. B.; Bruland, Ø. S.; Davies, C. de L. *Anticancer Res*, **2008**, *28*, 3557-3566.

(22) Lyng, H.; Vorren, A. O.; Sundfør, K.; Taksdal, I.; Lien, H. H.; Kaalhus, O.; Rofstad, E. K. *Int J Cancer*, **2001**, *96*, 182-190.

(23) Fodstad, Ø.; Brøgger, A.; Bruland, Ø.; Solheim, Ø. P.; Nesland, J. M.; Pihl, A. *Int J Cancer*, **1986**, *38*, 33-40.

(24) Misselwitz, B.; Schmitt-Willich, H.; Ebert, W.; Frenzel, T.; Weinmann, H. J. *Magn Reson Mat Phys Biol Med*, **2001**, *12*, 128-134.

(25) Weinmann, H. J.; Ebert, W.; Misselwitz, B.; Schmitt-Willich, H. *Eur J Radiol*, **2003**, *46*, 33-44.

(26) Patlak, C. S.; Blasberg, R. G.; Fenstermacher, J. D. *J Cereb Blood Flow Metab*, **1983**, *3*, 1-7.

(27) Reyes-Aldasoro, C. C.; Wilson, I.; Prise, V. E.; Barber, P. R.; Ameer-Beg, S. M.; Vojnovic, B.; Cunningham, V. J.; Tozer, G. M. *Microcirculation*, **2008**, *15*, 65-79.

(28) Ogan, M. D. *Invest Radiol*, **1988**, *23*, 961-961.

(29) Endrich, B.; Asaishi, K.; Gotz, A.; Messmer, K. *Res Exp Med (Berl)*, **1980**, *177*, 125-134.

(30) Verhoye, M.; Boudewijn, P. J. van der S.; Rijken, P.; Peters, H.; Van der Kogel, A. J.; Pée, G.; Vanhoutte, G.; Heerschap, A.; Van der Linden, A. *SPIE*, **1999**, *3660*,

(31) Gaustad, J. V.; Brurberg, K. G.; Simonsen, T. G.; Mollatt, C. S.; Rofstad, E. K. *Neoplasia*, **2008**, *10*, 354-362.

(32) Duncan, R.; Izzo, L. *Adv Drug Deliv Rev*, **2005**, *57*, 2215-2237.

(33) Su, M. Y.; Mühler, A.; Lao, X.; Nalcioglu, O. *Magn Reson Med*, **1998**, *39*, 259-269.

(34) Jain, R. K. *Cancer Metastasis Rev*, **1990**, *9*, 253-266.

(35) Dvorak, H. F.; Nagy, J. A.; Dvorak, J. T.; Dvorak, A. M. *Am J Pathol*, **1988**, *133*, 95-109.

(36) Kumar, S.; Ghellal, A.; Li, C.; Byrne, G.; Haboubi, N.; Wang, J. M.; Bundred, N. *Cancer Res*, **1999**, *59*, 856-861.

(37) Weidner, N.; Folkman, J.; Pozza, F.; Bevilacqua, P.; Allred, E. N.; Moore, D. H.; Meli, S.; Gasparini, G. *J Natl Cancer Inst*, **1992**, *84*, 1875-1887.

(38) Vermeulen, P. B.; Verhoeven, D.; Hubens, G.; Vanmarck, E.; Goovaerts, G.; Huyghe, M.; Debruijn, E. A.; Vanoosterom, A. T.; Dirix, L. Y. *Ann Oncol*, **1995**, *6*, 59-64.

(39) Ellis, L. M.; Takahashi, Y.; Fenoglio, C. J.; Cleary, K. R.; Bucana, C. D.; Evans, D. B. *Eur J Cancer*, **1998**, *34*, 337-340.

(40) Duarte, I. G.; Bufkin, B. L.; Pennington, M. F.; Gal, A. A.; Cohen, C.; Kosinski, A. S.; Mansour, K. A.; Miller, J. I. *J Thorac Cardiovasc Surg*, **1998**, *115*, 652-658.

(41) Tsuzuki, Y.; Fukumura, D.; Oosthuyse, B.; Koike, C.; Carmeliet, P.; Jain, R. K. *Cancer Res*, **2000**, *60*, 6248-6252.

(42) Yuan, F.; Chen, Y.; Dellian, M.; Safabakhsh, N.; Ferrara, N.; Jain, R. K. *Proc Natl Acad Sci U S A*, **1996**, *93*, 14765-14770.

(43) Pike, M. M.; Stoops, C. N.; Langford, C. P.; Akella, N. S.; Nabors, L. B.; Gillespie, G. Y. *Magn Reson Med*, **2009**, *61*, 615-625.